**POLITECHNIKA WROCŁAWSKA**
Faculty of Chemistry
*Advanced Materials Engineering and Modelling Group*

**UNIVERSITY OF LIMOGES**
Faculty of Science and Technology
*Peirene Laboratory*

**Thesis**

**EMMA L. ROBBINS**

# Design, optimisation, and characterisation of two- and multi-photon absorption photosensitizers for their prospective use in photodynamic therapy

*Supervisor:* Dr. Katarzyna Matczyszyn

*Supervisor:* Dr. Stéphanie Leroy-Lhez

*Co-supervisor:* Dr. Nicolas Villandier

Date:

Rapporteurs:

Examiners:

This work was done as part of <<POLYTHEA: How Light Can Save Lives>> Joint Doctorate programme, financially supported by the European Union’s Horizon 2020 research and innovation programme under the Marie Skłodowska-Curie grant agreement no. 764837

POLYTHEA
HOW LIGHT CAN SAVE LIVES

European Commission

Marie
Skłodowska-Curie
Actions

Mum

Dad

Siân

Grandma

Friends and Chosen Family

드캐

# ACKNOWLEDGEMENTS

Firstly, I would like to thank Dr Stéphanie Leroy-Lhez as the project coordinator of POLYTHEA, the international advisory board, and the supervisors for giving me the opportunity to pursue this project and for forever changing my life. And a special thank you to Dr René Williams, who guided me through my Masters project, and who led me to the POLYTHEA project.

I would like to begin by thanking those in Limoges, the place I called home for the beginning of my PhD. I would like to thank Aurore Berthier, there are no ways to fully repay you for your kindness and patience, my time in Limoges ran a lot smoother and more enjoyable with your help! Thank you, a million times, for allowing me to not have to worry about French administration! Thank you also to Sylvie for giving me a place to stay (more than once!) after having accommodation being closed and broken airplanes! I would like to thank my co-supervisor Dr Nicolas Villandier for walking this novice through lignin nanoparticle synthesis and characterisation, and for your corrections and comments helping me to improve my thesis. Thank you to all of the members of the Peirene Laboratory who helped me during my time in the lab in Limoges, and for introducing me to the joys of TRG. Thank you to my Supervisor in Limoges, Dr Stéphanie Leroy-Lhez. Thank you for giving me this opportunity, for your support, and for my first raclette! Thank you to those I met in Limoges outside of the lab, thank you for allowing me into your lives and homes, and for all the fun times we were able to have in Limoges.

I would like to give a big thanks to those I met and worked with in Wrocław, especially because I arrived in the country two weeks before everything shut down! Thank you to Marta for your kindness and patience in helping me with pretty much everything in the lab! I definitely would not have been able to accomplish most of what I have without your help. Thank you to Krzysztof, Sebastian, and Dominika for your help introducing me to the lab and how everything works, and for all of your help with our publication! Thank you to Radek for your help with the many, many Z-scan measurements.

Thank you to Prof Marek Samoć for all of your knowledge and critiques that helped to improve my work in all technical aspects. Thank you very much to my supervisor in Wrocław, Dr Kasia Matczyszyn, for your patience and guidance, and unwavering belief in me. It was an eventful start to my time in Poland, but thank you for all of your help to get through it! And a special thank you to Grażyna for giving me a place to stay in Poland, thank you.

During my time in Poland, I had the opportunity to work in another lab group at the university of Wrocław. I would like to thank all of those who made my short time there run smoothly and definitely more entertaining! Thank you especially to Rafał, Max, and Alexa for your help (and patience) with submitting all of my many NMR/MS samples! Thank you very much to Dr Bartek Szyszko for allowing me to be a part of your group, and for all of your help, assistance and kindness.

I would like to thank all those I met during my PhD who kept me going, those who made me forget all the stresses, those who kept me entertained, and those who helped me through the rough times. I don't know how I can repay you all for the kindness, generosity, and understanding, but I am eternally grateful to have you in my life! To my twin, my better half, to have been by your side through this journey has been a true highlight and to have a friendship that will last a lifetime I will forever be thankful for (and amazed by!)! Here's to more Hyde Park adventures!

Lastly, I would like to thank my friends who have been with me since high school, and through Keele and Amsterdam, and most importantly my family, for your unwavering support of me. Thank you for keeping me as sane as possible during this time and for helping me keep going when I didn't think I could anymore, whether you realised it or not I could not have done this without any of you. Thank you to my mum, dad, Siân, Grandma, the Hawarden Girlies, White Girl Rapping, my Brum chum, my Seoul-mate, thank you all. All of those nights of InSomnia were worth it, thank you!

– All's well that ends better –

J. R. R. Tolkien

# Contents

# Contents

# Abbreviations

## ABBREVIATIONS

**1PA** – One-Photon Absorption

**2PA** – Two-Photon Absorption

**1PE** – One-Photon Excited

**2PE** – Two-Photon Excited

**2PEF** – Two-Photon Excited Fluorescence

**2PFM** – Two-Photon Fluorescence Microscopy

**A** – decay amplitude

**AFM** – Atomic Force Microscopy

**$^{13}$C-NMR** – Carbon-Nuclear Magnetic Resonance

**Eq.** – Equation

**Equiv.** – Equivalent

**esu** – electrostatic unit(s)

**fs** – femtosecond(s)

**$^{1}$H-NMR** – Proton-Nuclear Magnetic Resonance

**h** – hour(s)

**Im (γ)** – Imaginary part of the cubic hyperpolarisability

**IRF** – Instrument Response Function

**ISC** – Intersystem Crossing

**MALDI** – Matrix-assisted Laser Desorption-Ionisation

**min** – minute(s)

**MS** – Mass Spectroscopy

**mW** – milliwatt

**NIR** – Near-infrared

**NIR-I** – First Near-Infrared region

**NIR-II** – Second Near-Infrared region

**NLO** – Non-linear Optical

**nm** – nanometre(s)

**ns** – nanosecond(s)

**PACT** – Photodynamic Antimicrobial ChemoTherapy

**PAH** – Polyaromatic Hydrocarbon

**PDT** – Photodynamic Therapy

**PS** – Photosensitizer

**rcf** – relative centrifugal force

**Re (γ)** – Real part of the cubic hyperpolarisability

**$R_f$** – Retention factor

**ROS** – Reactive Oxygen Species

**r. t.** – room temperature

**$^1O_2$** – singlet oxygen

**SDGC** – Sucrose Density Gradient Centrifugation

**TLC** – Thin Layer Chromatography

**UV-Vis** – Ultraviolet-Visible spectroscopy

**γ** – cubic hyperpolarisability

**λ** – wavelength

**2λ** – double wavelength

**$\lambda_{ex}$** – excitation wavelength

**$\sigma_2$** – 2PA cross-section

**τ** – fluorescence lifetime

**$\Phi_\Delta$** = singlet oxygen quantum yield

**$\Phi_f$** = fluorescence quantum yield

## Compounds and Solvents:

**Bz** – Benzaldehyde

**DCM** – Dichloromethane

**DDQ** – 2,3-dichloro-5,6-dicyano-1,4-benzoquinone

**DEDA** – N, N-diethylethylenediamine

**DMF** – Dimethylformamide

**DMSO** – Dimethyl sulfoxide

**EDC** - 1-ethyl-3-(3-dimethylaminopropyl)carbodiimide

**HCl** – Hydrochloric acid

**HOAt** – 1-hydroxy-7-azabenzotriazole

**Mes** – Mesitaldehyde

**Pet. ether** – Petroleum ether

**PIFA** – bis(trifluoroacetoxy)iodo benzene

**TEA** – Triethylamine

**TFA** – Trifluoroacetic Acid

**THF** – Tetrahydrofuran

**THPP** – 5,10,15,20-Tetrakis (4-hydroxyphenyl)-21H,23H-porphine

**TMSA** – Trimethylsilylacetylene

**T(OAc)PP** – 5,10,15,20-Tetrakis (4-acetyloxyphenyl)-21H,23H-porphine

**ZnTHPP** – Zinc (II) 5,10,15,20-Tetrakis (4-hydroxyphenyl)-21H,23H-porphine

# Introduction

# INTRODUCTION

This thesis presents work done in collaboration between the Advanced Materials Engineering and Modelling group at Politechnika Wrocławska (PWr) in Poland, and the Peirene Laboratory at the University of Limoges (Unilim) in France. The aim of this work is to characterise and synthesise new and modified photosensitizers with two-photon absorption properties that can be used within photodynamic therapy/photodynamic antimicrobial chemotherapy (PDT/PACT) and theranostic applications.

PDT is a promising alternative for the non-invasive treatment of certain cancers, such as head, neck, and skin cancers,[1-4] the treatment of macular degeneration,[5, 6] as well as cases of oesophageal,[7-9] oral,[10-13] and lung[14-16] cancers. PDT has also shown promise in the treatment of warts and acne.[17, 18] PACT is a promising strategy for the killing of pathogenic bacteria, particularly antibiotic-resistant bacteria.[19-22] PACT has also been frequently used in the disinfection of blood products.[23-25] PDT and PACT both involve the use of a light source, a photosensitizer (PS), and a source of oxygen (Figure 1).

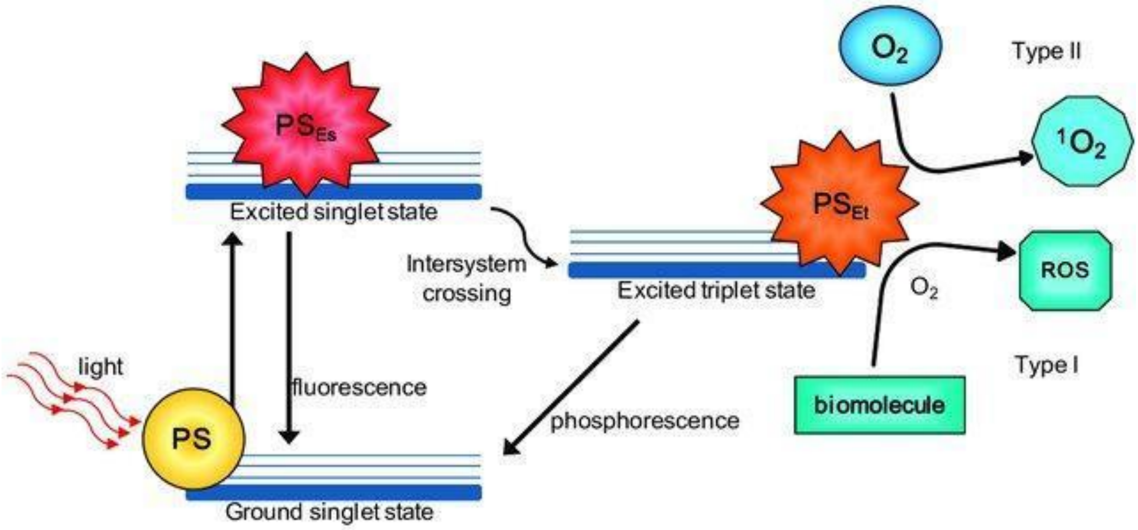

Figure 1. Schematic representation of the mechanism of action of PDT.[26]

The PS is excited from its ground singlet state to its excited singlet state, using a light source (*i.e.,* laser, LED diodes). Once the PS is in its excited singlet state ($PS_{Ess}$), it can return back to its ground singlet state via fluorescence, or non-radiative decay, or preferentially for PDT applications it will transform to its excited triplet state ($PS_{Ets}$) via intersystem crossing (ISC). The $PS_{Ets}$ can either undergo phosphorescence back to its ground singlet state, or it can interact directly with molecular oxygen ($O_2$), or in tandem with surrounding biomolecules, it can take part in the production of reactive oxygen species (ROS). ROS can be produced in one of two ways: Type-I via electron/hydrogen transfer to produce radical species, or Type-II via energy transfer to produce singlet oxygen ($^1O_2$). Type-I photochemistry involves reaction of the $PS_{Ets}$ with a biomolecule (lipids, proteins, or nucleic acids) where hydrogen transfer occurs via the radical mechanism and ROS is generated after reaction with $O_2$. Herein, we are more interested in the Type-II mechanism. Type-II photochemistry involves transfer of energy from the $PS_{Ets}$ to the ground triplet state of molecular oxygen ($^3\Sigma^-_g$, $^3O_2$). Oxygen in its ground triplet state is promoted to its short-lived excited singlet state ($^1\Sigma^+_g$) which rapidly relaxes to its longer-lived excited singlet state ($^1\Delta_g$), known as singlet oxygen ($^1O_2$). The occupancy of the π* orbital of each state of oxygen[27] is displayed in Figure 2.

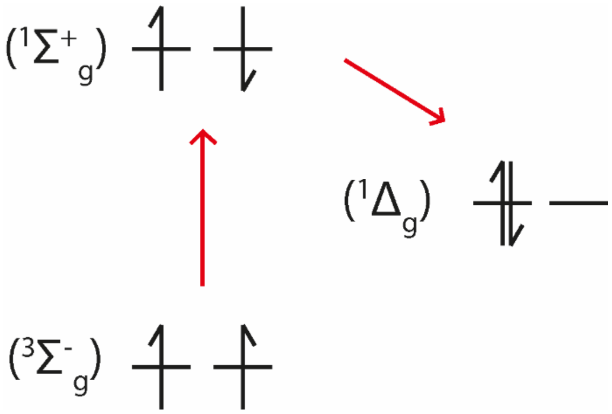

Figure 2. Oxygen π* orbital occupancy of ground triplet state ($^3\Sigma^-_g$), short-lived excited singlet state ($^1\Sigma^+_g$), and longer-lived excited singlet state ($^1\Delta_g$).

$^1O_2$ is a highly reactive and cytotoxic species playing an active role in the oxidative stress of cancer cells during PDT. $^1O_2$ plays various roles in biological systems, most notably it can act as an antibacterial/antimicrobial agent in both plants and animals.[28-30] $^1O_2$ has a relatively short lifetime (3.7 μs in $H_2O$, extended to 67 μs in $D_2O$),[31, 32] therefore, when used in PDT, it is only effective in the area where it is generated, typically within a 20 nm radius.[33] Localisation of the PS should also be taken into consideration during *in vivo* and *in vitro* studies.

Another important factor of PDT is the phototherapeutic window (Figure 3). Due to skin and tissue being able to absorb shorter wavelengths of light, and with the absorption of longer wavelengths by water, there lies a "window" that is optimal for phototherapeutic applications between 600 and 900 nm.[34, 35] There also exists a second near-infrared (NIR) window for *in vivo* imaging between 1000 and 1350 nm, beyond the absorption of water.[36] However, due to the lack of compatible PSs or other molecules capable of working in this wavelength range the use of this spectral range is limited.

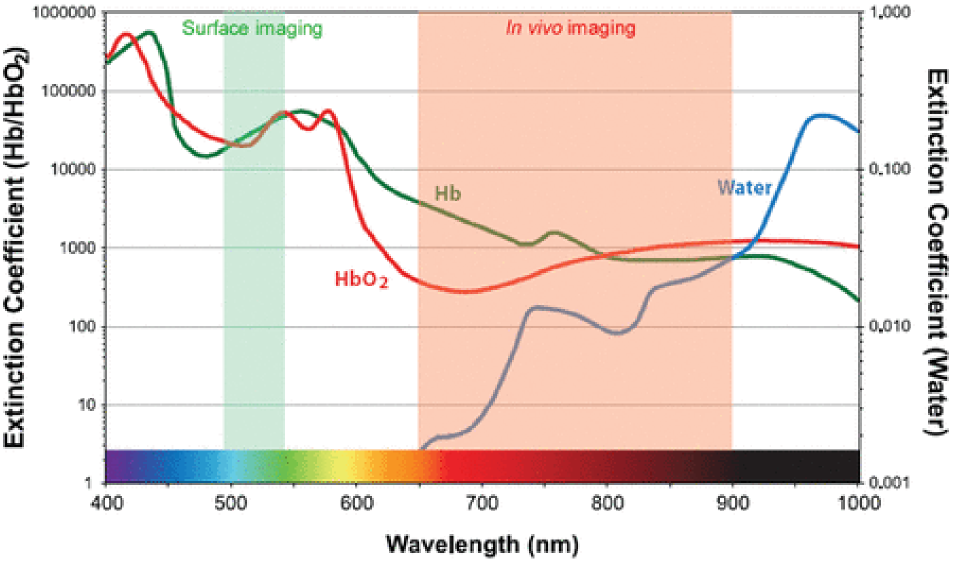

Figure 3. Representation of the ideal phototherapeutic window between 650 and 900 nm.[37]

As with other technologies, PDT and its components can still be further developed for improved application. One such improvement of PDT is the use of two-photon absorption (2PA). 2PA is the process of the simultaneous absorption of two photons of lower energy at twice the excitation wavelength to supply the same energy as that of one photon of higher energy.[38] Meaning, two lower energy photons at 800 nm can cause the same transition as the absorption of one higher energy photon at 400 nm. When combined with PDT, 2PA-PDT works in the same manner as described above, but the transition energy is equal to the sum of that of two simultaneously absorbed photons of lower energy (Figure 4).

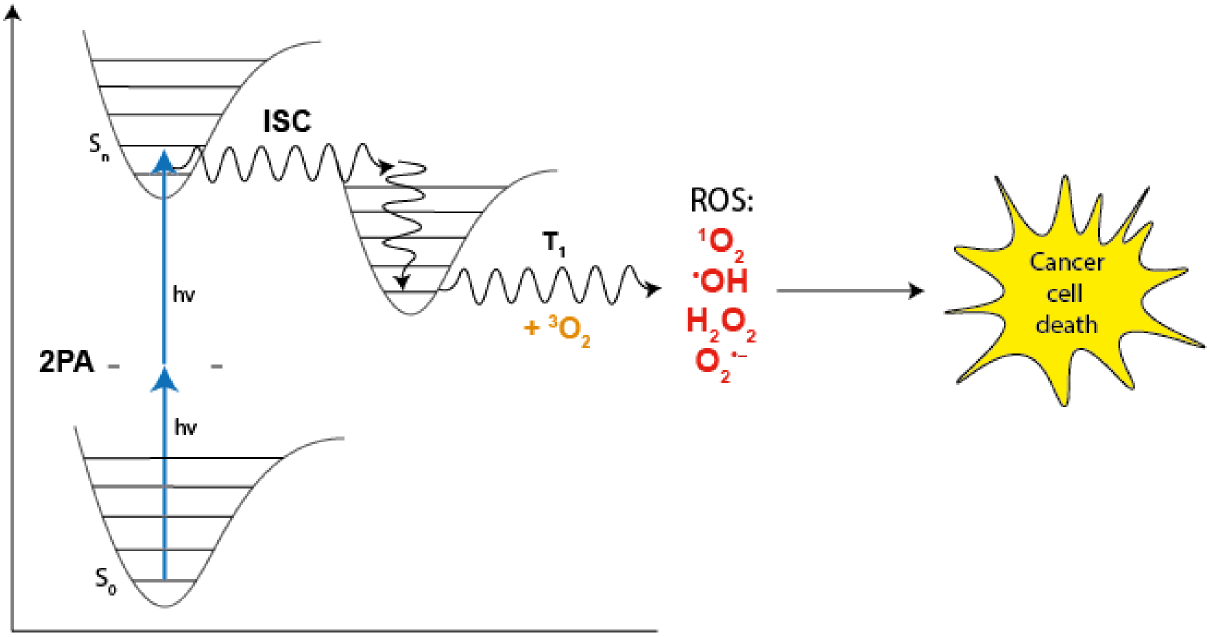

Figure 4. Scheme representing 2PA-driven PDT. The $S_0 \rightarrow S_n$ transition must be two-photon allowed.[39]

2PA was first analysed theoretically in the 1930s by Maria Göppert-Mayer, thus, the unit of two-photon absorption cross-section has been named after her, GM (1 GM = $10^{-50}$ $cm^4$ s).[40] It wasn't until 1961 with the development of the laser that 2PA was observed experimentally (in $CdF_2:Eu^{2+}$ crystal).[41] In the 1990s, 2PA studies became more detailed and extensive due to the advancements and accessibility of picosecond and femtosecond (short pulse) lasers. Thus, more and more information has been able to be collected regarding materials that are suitable for 2PA applications.

2PA has many possible applications, such as optical data storage,[42, 43] microfabrication,[44, 45] 3D polymerisation,[46, 47] and more. 2PA can also be valuable when combined with PDT (2PA-PDT), its application is able to exploit several factors of the 2PA process.[39, 48, 49] Due to the use of lower energy, NIR, light sources, 2PA-PDT should be able to reduce photothermal damage of the irradiated area of skin/tissue. With NIR light lying in the first phototherapeutic window of biological tissue, this promises deeper penetration depth,[50] hopefully, leading to the treatment of deeper lying tumours as an alternative to surgical or chemo/radiotherapy. The excitation beams associated with NIR-lasers produced 2PA absorption essentially only close to a well-defined focal point, unlike the case of 1PA where the absorption takes place everywhere along the path of the beam (Figure 5). There is less light scattering and less reduction of optical power caused by absorption from tissues in the NIR range.

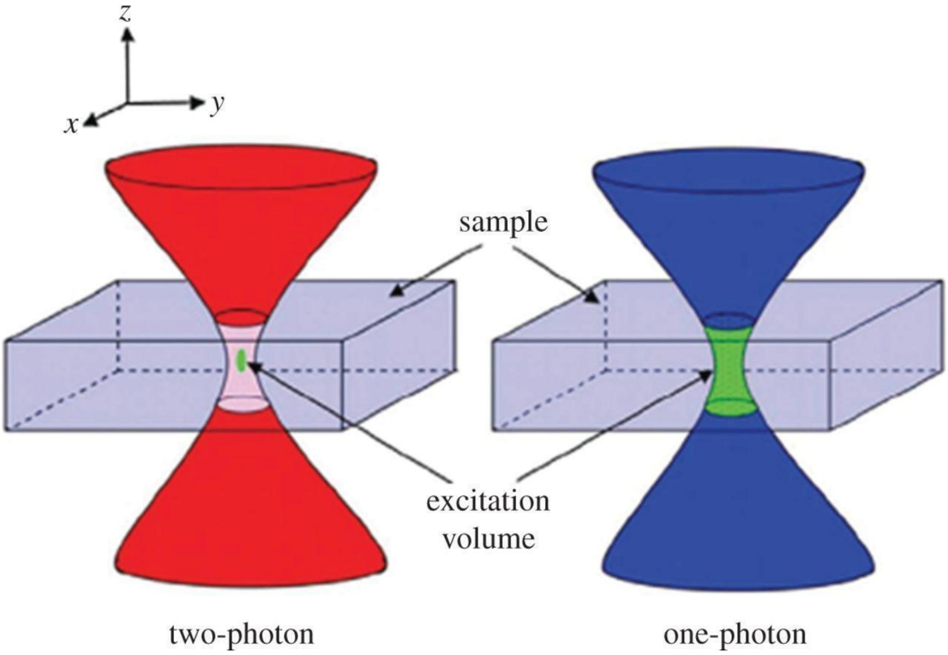

Figure 5. Two-photon absorption (2PA) vs. one-photon absorption (1PA) focal point of excitation beam.[51]

One drawback of 2PA-PDT is the need for expensive laser light sources that are required to provide intensities on GW/cm$^2$ scale.[52] Aside from developments of affordable pico and femtosecond laser technology, one such way to improve the practicability of 2PA-PDT is to develop more highly efficient PSs with improved 2PA capabilities, *i.e.*, by enhancing their two-photon absorption cross-sections ($\sigma_2$). Improvements of the PS component of 2PA-PDT/PACT have been extensively studied,[39] and are still undergoing refinement.

The most popular choice of PS for PDT applications are typically porphyrins. A porphyrin molecule contains 4 pyrrolic rings joined together by a methylene bridge (Figure 6). They can either exist as a free-base, or they can be metallated with a range of metals. Common metals used within PDT applications are zinc and ruthenium.[49, 53-56]

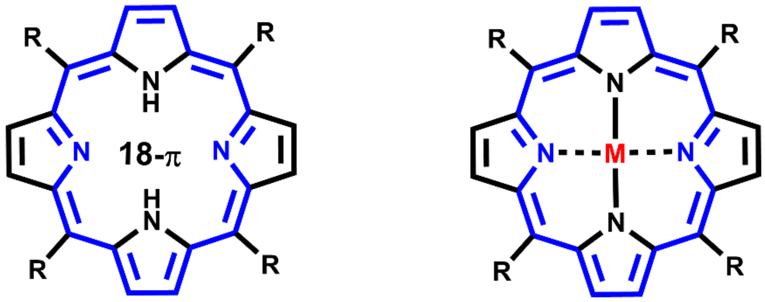

Figure 6. Structure of a porphyrin macrocycle (left = free-base, right = metallated (M = metal)). The π-conjugation system is highlighted in blue.

They consist of a conjugated system of 18-π electrons (the aromatic pathway is highlighted in blue). Porphyrin macrocycles are generally planar, but are flexible and can be easily distorted from their metallation, as well as substitution of bulky groups at the *meso*-positions (represented by the R-groups). Tetrapyrrolic structures are commonly found in nature. Heme in haemoglobin proteins (in red blood cells), has a porphyrin structure that is metallated with $Fe^{2+}$.[57] Myoglobin participates in the storage and transport of oxygen in muscle tissue, and contains a similar structure to heme.[58] Additionally, porphyrin structures are related to that of chlorin and bacteriochlorin (Figure 7), which can also be found in nature, and they have also been extensively studied and used within PDT/PACT applications.[35]

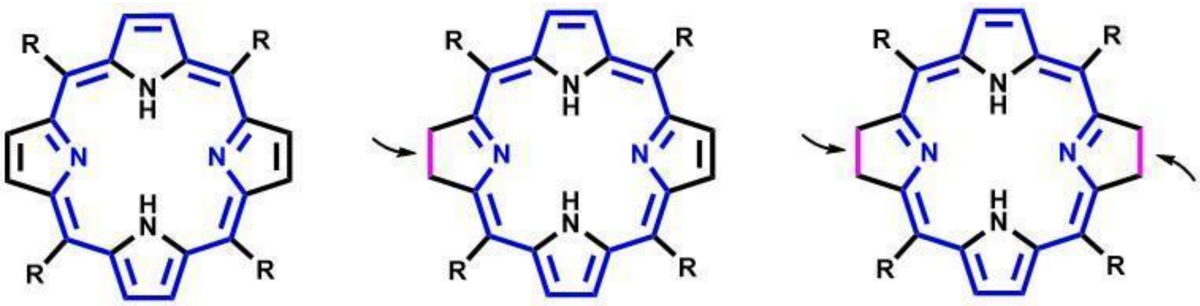

Porphyrin Chlorin Bacteriochlorin

Figure 7. Comparison of related structures of Porphyrin, Chlorin, and Bacteriochlorin. The reduced bonds in chlorin and bacteriochlorin are highlighted in pink, indicated by an arrow.

Porphyrin- and chlorin-core compounds have been readily used for PDT treatment of cancers. The most commonly used being Foscan®, Protoporphyrin IX (PpIX), Photofrin®, and Visudyne®, amongst others.[59-61] However, they have limits for their use, particularly due to their high photosensitivity and small 2PA cross-sections. Foscan® is a second-generation PS and still currently used in the treatment of head and neck cancers.[62, 63] Despite being one of the most regularly used PSs, Foscan® is readily attributed to high photosensitivity, often remaining in the body for up to 4 days, post-PDT treatment. However, this PS only requires a very low light and drug dose, 5 J $cm^{-2}$ and 0.1 mg $kg^{-1}$, respectively.[64] Due to the high photosensitivity (as well as its relatively low 2PA cross-section of 28 ± 8 GM, in dimethyl sulfoxide at 775 nm),[65] the optimisation of this molecule and related compounds are of interest. In order to utilise these porphyrin compounds for 2PA applications, they are required to have at least several properties including, (1) high 2PA cross-section value, (2) high singlet oxygen quantum yield ($\Phi_\Delta$), (3) high absorption in the phototherapeutic window, and (4) good photostability.

Developments of porphyrins and their related chlorin and bacteriochlorin structures have been widely studied. Several modifications of porphyrins that have been explored include, extension of the π-conjugated system.[40, 66, 67] It was found that an effective way to improve the 2PA properties of porphyrins, and related structures, is to extend the π-conjugation system. The large conjugation length provides ease of delocalisation of the π-electrons. Another relatively straightforward modification is the introduction of strong electron acceptor and/or donor groups either at the centre or terminal ends of a molecule.[68-71] In the case of porphyrins, and related structures, this means introducing the electron acceptor/donor groups at their *meso*-position. Sometimes, for these compounds their solubility is often relatively low. One successful way to overcome this is via their encapsulation in nanoparticles,[72, 73] micelles,[74-76] as well as lignin and cellulose,[77-80] and polymers.[81-83] Encapsulation is not only capable of enhancing their solubility, but also potentially their diagnostic capabilities. Where the PS isn’t highly fluorescent (a common side effect from modifying the structure for improved 2PA, and high singlet oxygen yield, properties) the “shell” may be fluorescent, thus this further extends their usefulness in joint therapy and diagnostic (theranostic) applications. Other modifications to improve 2PA properties include dimerisation,[84, 85] metallation,[86, 87] and addition of a 2PA antenna.[88, 89]

An even wider range of PSs can be realised with the modification/expansion of the porphyrin macrocycle core. Core-modifications cause changes to the electronic properties of porphyrin. A variety of heterocycles, and aromatic rings, can be added to expand the porphyrin core by replacing one or more of the pyrrole units. Heterocycles such as furan, thiophene, selenophene, and tellurophene lead to heteroporphyrins **1** (Figure 8).[90] Replacing one pyrrole with benzene leads to benziporphyrinoids **2** and **3**.[91] And the replacement with naphthalene produces aceneporphyrinoid structures, such as naphthiporphyrins **4** and **5**.[92]

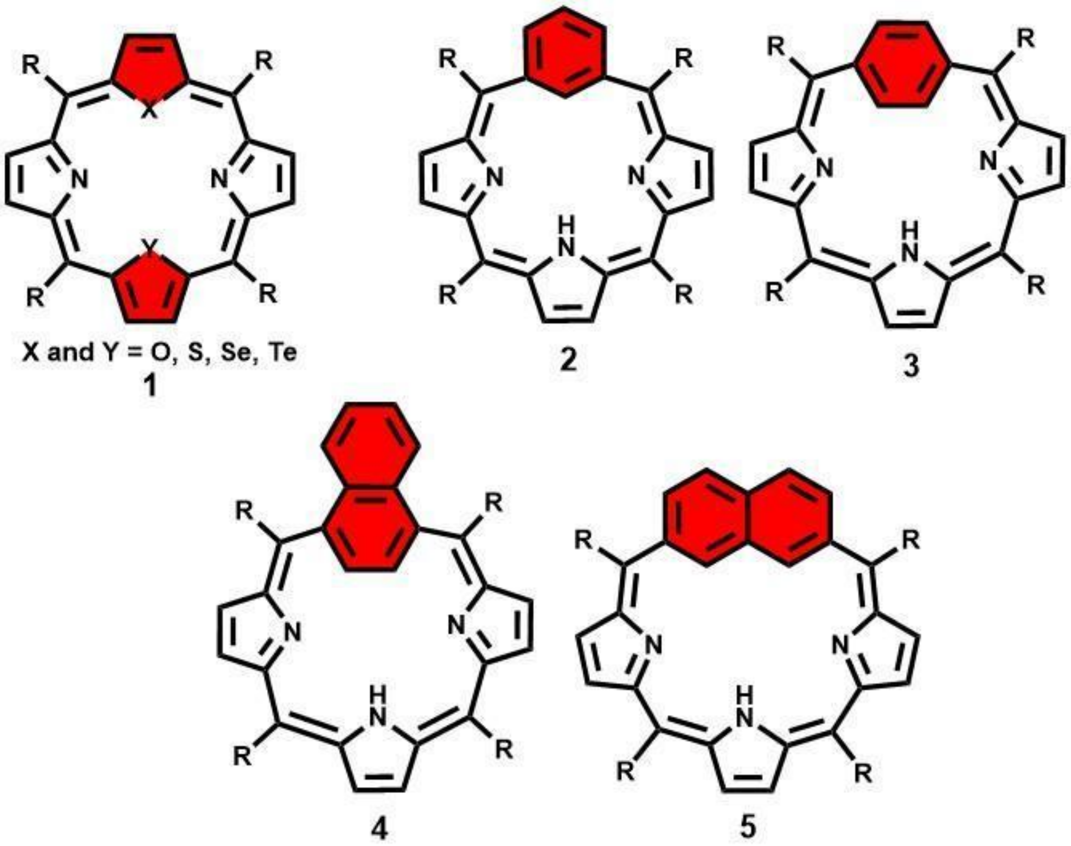

Figure 8. Structures of various core-modified macrocycles: heteroporphyrins **1**, benziporphyrinoids **2** and **3**, aceneporphyrinoids such as naphthiporphyrins **4** and **5**.

These expanded and core-modified porphyrins have been well studied, but their non-linear photophysical properties have yet to be fully explored. Several studies have been completed where expanded macrocycles have shown great promise for 2PA applications, displaying large 2PA cross-section values.[93-95] Other analogues of porphyrins described as porphyrinoids include texaphyrins, hexaphyrins, N-confused porphyrins, and more.[96, 97]

In this framework, the first chapter of this work details two-photon excited emission and two-photon microscopy measurements of porphyrin-encapsulated acetylated lignin nanoparticles. The second chapter presents non-linear optical measurements of modified Foscan® compounds, including their two-photon absorption cross-sections. Chapter three details the synthesis of porphyrin with an elongated π-conjugation system with analysis by $^1$H-NMR and MS (Maldi-TOF), as well as non-linear optical measurements using the Z-scan method. The final chapter, chapter four, will discuss the two-photon absorption properties of a series of core-modified macrocycles.

# Chapter I:

## Porphyrin-loaded acetylated lignin nanoparticles

## INTRODUCTION

There have been many ways to improve the solubility as well as the properties of porphyrins for their use in two-photon applications. One such way is their encapsulation within nanoparticles. Indeed, encapsulation of molecules with limited solubility can help overcome any related solubility issues, particularly in aqueous media.[98-101] Also, encapsulation may aid in non-specific targeting molecules being more target specific, as nanoparticles can be easily functionalised with targeting moieties, etc. Another usefulness of nanoparticles can be that they also have certain optical properties, depending on the material being used, making them attractive for use in combination with more potent porphyrins/photosensitizers (PSs).[100, 102-104]

One such material that has shown its usefulness for encapsulation, of porphyrins and other PSs, is Lignin.[105-108] Lignin is an aromatic polymer and a renewable resource, second in abundance to cellulose.[109] Lignin can be collected in large quantities as a by-product of the paper-making and pulping industries. Currently, only 1-2% of this lignin is further utilised in the production of modified and enhanced products.[110] Lignin has been shown to display several beneficial properties for biological applications. Several studies have displayed their antioxidant, antimicrobial, and anti-inflammatory properties, as well as low cytotoxicity, and UV-blocking properties.[111-114] In order to transform the unordered and complex lignin into more manageable, ordered, nanoparticles, modifications of lignin have been the subject of various research.[115-117] One such modification being acetylation, which has shown to further improve the photophysical properties of lignin. Acetylated lignin (Figure 9) is capable of generating reactive oxygen species (ROS) making it particularly advantageous for phototherapeutic applications.[118] Acetylated lignin has also been shown to produce spherical nanoparticles under certain conditions, and their usefulness has been demonstrated in the transportation of active molecules.[77, 119] This biologically compatible material is attractive for use in combination with certain drugs and/or photosensitizers within photodynamic therapy (PDT) and photodynamic antimicrobial chemotherapy (PACT) applications.[78, 120-122]

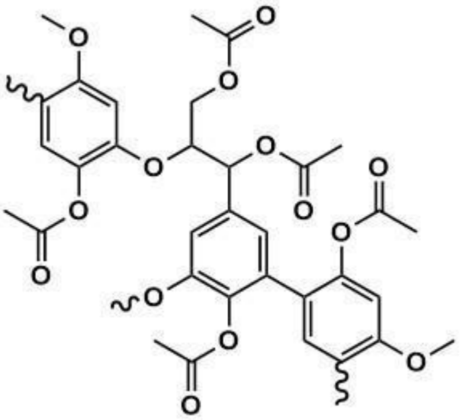

Figure 9. Structure of acetylated lignin.

As proposed in the introduction of this work, a way to improve the impact of PDT is to combine it with two-photon absorption (2PA).[123, 124] The main advancement of 2PA mediated PDT lies in the improvement of photosensitizers with high two-photon absorption cross-sections, featuring a large π-conjugated system, strong end donor and/or acceptor groups, as well as narrow one-photon absorption (1PA) and 2PA bands.[39] Photosensitizers that have been widely studied and are capable of absorbing at longer wavelengths are porphyrins, typically within the first biological optical window (NIR-I: 650 – 950 nm). There also lies a second biological optical window (NIR-II) between 1000 and 1350 nm.[34, 125-127] Many photosensitizers may not be as biologically compatible as desired being poorly soluble in aqueous media or having poor stability due to aggregation. A widely utilised method to overcome these issues are to embed or encapsulate the photosensitizers within nanoparticles.[128-131] With the low cytotoxicity of lignin, its abundance and renewability, as well as it being easily modified, lignin and thus, acetylated lignin nanoparticles are an attractive choice for this purpose.

This chapter will cover the investigation of the linear and non-linear optical properties of several porphyrins that have been embedded in acetylated lignin nanoparticles in the NIR regime via two-photon excited fluorescence and microscopy techniques.

Three different porphyrins were encapsulated into acetylated lignin nanoparticles (sample 1, **S1**: 5,10,15,20-Tetrakis (4-hydroxyphenyl)-21H,23H-porphine (THPP), sample 2, **S2**: Zinc (II) 5,10,15,20-Tetrakis (4-hydroxyphenyl)-21H,23H-porphine (ZnTHPP), and sample 3, **S3**: 5,10,15,20-Tetrakis (4-acetyloxyphenyl)-21H,23H-porphine (T(OAc)PP), Figure 10). A control sample of empty acetylated lignin nanoparticles, containing no porphyrin, was also examined (sample 4, **S4**). The different experimental techniques used were two-photon excited fluorescence (2PEF),[132-135] atomic force microscopy (AFM),[136, 137] and two-photon fluorescence microscopy (2PFM).[138, 139] The particles (**S1**-**S4**) were studied as dispersions in buffer solution, as well as size separated. Separation of the nanoparticles was done according to the size of the particles, select fractions were examined to determine if the size of the particles had any effect on their photophysical properties.

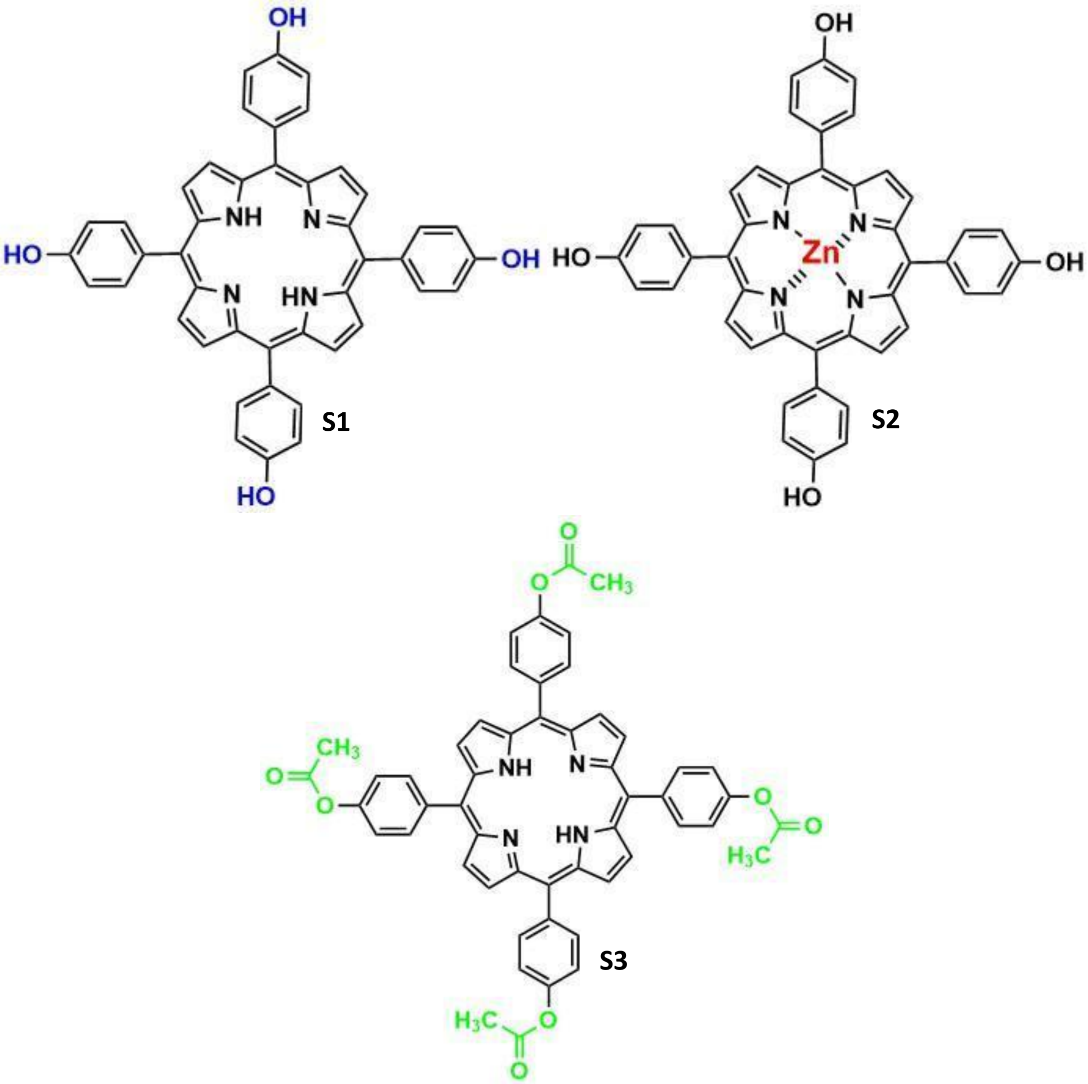

Figure 10. Structures of the three different porphyrins that were encapsulated (**S1**, **S2**, and **S3**).

## 1.1 MORPHOLOGY AND SIZE SEPARATION

### *1.1.1 Atomic Force Microscopy (AFM)*

The stock solutions of the encapsulated porphyrins contained particles of various sizes, ranging from several hundred nanometres to several micrometres. In order to visualise the particles using AFM, a droplet of the bulk dispersion (**S1**) was deposited on a coverslip and left to dry before being viewed. An AFM image was captured of the centre of the dry droplet of **S1**, Figure 11, after analysis of ca. 100 spherical particles, the average diameter of the fraction of the smallest structures was determined to be 94 ± 15 nm. It should be mentioned that a large number of particles with different sizes accumulated on the edge of the droplet during the drying process as a result of the coffee ring effect.[140] The large difference in sizes of the particles is due to the method of synthesis used. Because of the size difference of the particles, additional experiments were performed on the hybrid bulk solutions before and after separation by sucrose density gradient centrifugation (SDGC).[141, 142]

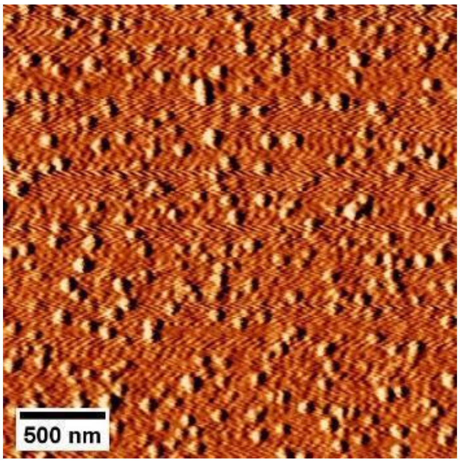

Figure 11. AFM images of lignin nanoparticles loaded with porphyrin (**S1**) in the center of the dry droplet of 15 times diluted stock solution deposited on a cover slip.

### *1.1.2 Size separation*

To separate the nanoparticles by their size, sucrose density gradient centrifugation (SDGC) was performed. Eight fractions of sucrose (0, 5, 7.5, 10, 12.5, 15, 17.5, and 20% w/v) dissolved in Milli-Q water were used for the SDGC procedure. 1500 µL aliquots of each sucrose fraction were layered slowly one on top of the other (in a 20 mL centrifuge tube), starting from the densest 20% w/v fraction working up to the least dense 0% w/v fraction. The final 1000 µL layer containing the nanoparticle dispersion suspended in Milli-Q water was layered on top of the 0% w/v sucrose fraction. The tube is centrifuged for 30 minutes at 3000 rpm. After centrifugation, each layer was removed and separated into individual Eppendorf's. This procedure was repeated for each bulk dispersion, **S1-S3**. Before the samples underwent microscopy analysis, the sucrose was removed from each fraction. 700 µL was taken from each individual Eppendorf and centrifuged for 30 minutes at 2000 rcf (relative centrifugal force). The resulting supernatant was removed and the nanoparticles were resuspended in Milli-Q water. Henceforth, samples extracted from the 0% w/v sucrose fraction are referred to as *i.e.*, **S1-0**, those from the 10% w/v sucrose fraction as **S1-10**, and those from the 20% w/v sucrose fraction as **S1-20**, etc.

## 1.2 LINEAR PHOTOPHYSICAL CHARACTERISATION

### *1.2.1 Extinction spectra*

The extinction spectra of the bulk aqueous dispersions show the characteristic Soret band ($\lambda_{soret}$) of the free porphyrins. Weak Q-band signals can also be easily discerned in **S1**-**S3**. In contrast, the spectrum of porphyrin-free nanoparticles (**S4**) indicates mostly strong light scattering, with the absence of any well-defined absorption peaks (Figure 12).

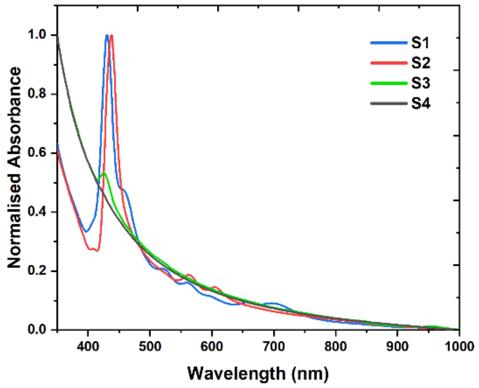

Figure 12. Normalised extinction spectra of bulk aqueous dispersions of porphyrins inside the nanoparticles, **S1**-**S4**. (**S1:** $\lambda_{max}$ = 430 nm, **S2:** $\lambda_{max}$ = 437 nm, **S3:** $\lambda_{max}$ = 426 nm).

The $\lambda_{soret}$ bands of the bulk aqueous dispersions are positioned at 430 nm (**S1**), 437 nm (**S2**), and 426 nm (**S3**). Compared to the unencapsulated porphyrin, there is an observed red-shift of the $\lambda_{soret}$ bands seen in each of the dispersions; $\lambda_{soret}$ of unencapsulated porphyrin = 424 nm (THPP), 419 nm (ZnTHPP), and 422 nm (T(OAc)PP).[78] There also indicates the splitting of the absorption bands resulting in new absorption components. The observed red-shift is typically observed for J-aggregates of porphyrins, with self-assembling playing the predominant role.

The UV-Vis spectra of select fractions from the separated **S1** bulk-dispersion (**S1-0**, **S1-10**, and **S1-20**), as well as from the separated **S4** bulk-dispersion (**S4-0** and **S4-10**) are shown in Figure 13. As with the previous spectra (Figure 12), the $\lambda_{soret}$ band is still observable, along with a small bathochromic shift moving from the smallest particle size fraction (**S1-0**) to the largest particle size fraction (**S1-20**); $\lambda_{soret}$ = 429 nm (**S1-0**), 431 nm (**S1-10**), and 433 nm (**S1-20**). Also observed is the splitting of the major absorption bands into two overlapping components, as above. The bathochromic shift of the Soret bands, along with the new emerging absorption components, can arise from the self-assembly of rigid, polar-rich porphyrin molecules into J-aggregates, as is likely with the bulk dispersions of **S1-S3**. J-aggregates can form through various intermolecular interactions, such as hydrogen bonding, electrostatic forces, and π-π stacking, which is a common phenomenon between porphyrin derivatives.[143, 144] These trends observed in the UV-Vis spectra have also been previously attributed to π-π interactions between the porphyrin core and the aromatic lignin residues, and hydrogen bonding, in literature studies such as reported by G. Marchand *et al*.[77, 121]

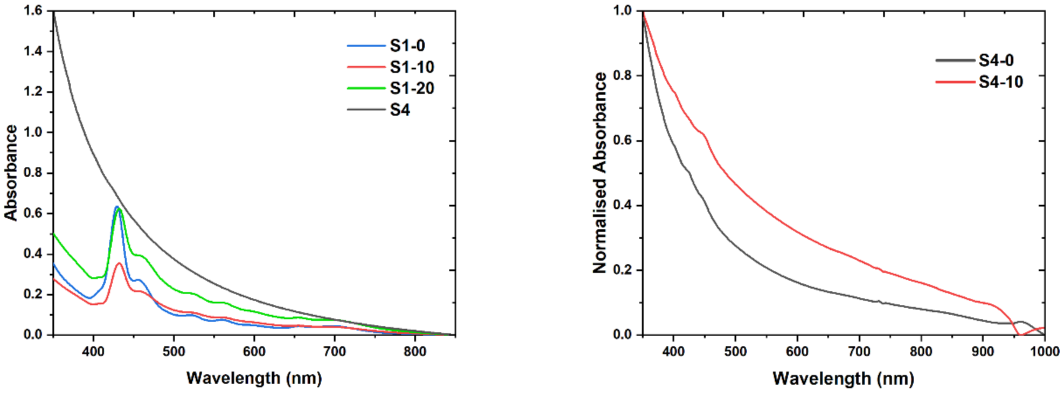

Figure 13. Left: Absorbance spectra of **S1-0**, **S1-10**, **S1-20**, and **S4** (**S1-0:** $\lambda_{max}$ = 429 nm, **S1-10:** $\lambda_{max}$ = 431 nm, **S1-20:** $\lambda_{max}$ = 433 nm). Right: Normalised absorbance spectra of **S4-0** and **S4-10**.

### *1.2.2 One-photon excited (1PE) fluorescence*

The fluorescence maxima of each bulk dispersion were determined from their one-photon excited (1PE) fluorescence spectra (Figure 14) to be 658 nm (**S1**), 612 nm (**S2**), and 649 nm (**S3**). The 1PE fluorescence decays were then recorded at the fluorescence maxima of the corresponding sample.

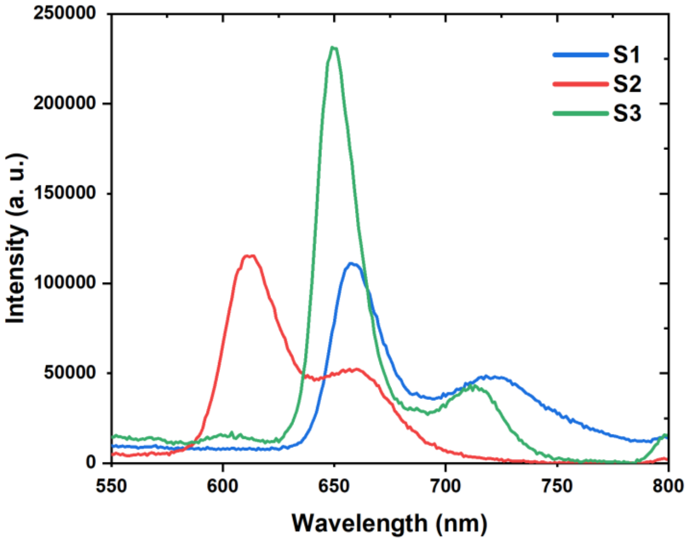

Figure 14. The 1PE fluorescence spectra of **S1**, **S2**, and **S3** ($\lambda_{ex}$ = 420 nm, phosphate buffer (50 mM), **S1** = 0.0547 mmol/dm$^3$, **S2** = 0.0627 mmol/dm$^3$, **S3** = 0.00597 mmol/dm$^3$).

*1.2.3 Time-resolved 1PE fluorescence*

The as-recorded fluorescence decay curves were fitted using mono- (**S2**), bi- (**S1**) as well as triple-exponential (**S3**) equations (see below, Eq. 1 - 3). The porphyrin-loaded acetylated lignin nanoparticles reveal fluorescence decays that depend strongly on the type of porphyrin that is encapsulated (Figure 15). The hydroxyl-containing (–OH) porphyrins display the shortest fluorescence lifetime values, 0.335 ns for **S2**, and 0.723 ns for **S1** (weighted average, Eq. 4). **S3** displays the longest fluorescence lifetime of 4.62 ns (weighted average, Eq. 4), all the fluorescence lifetime details are shown in Table 1. To compare, the singlet excited-state lifetimes of unencapsulated porphyrins are 9.9 ns (THPP) and 2.0 ns (ZnTHPP).[145] Due to the tendencies of J-aggregates to form through self-assembly of the porphyrins within the confinements of the particles,[143, 146, 147] and alternatively, π-π interactions between the porphyrin and the acetylated lignin, it is of no surprise that the measured fluorescence decay lifetimes are shorter for the porphyrin-loaded nanoparticles compared to the "free" porphyrins.

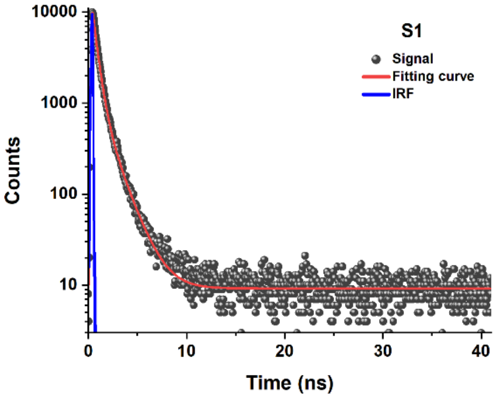

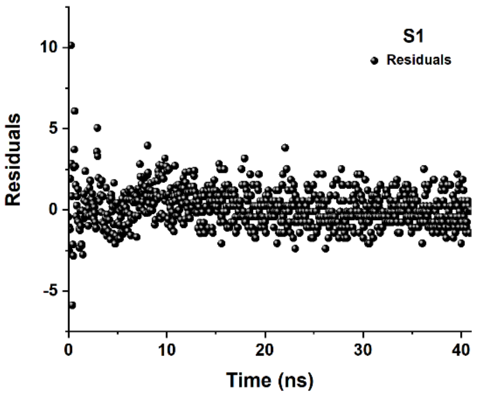

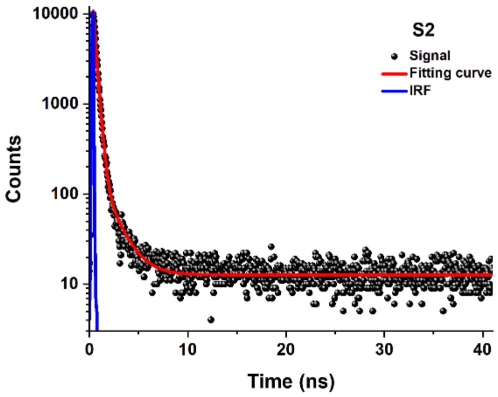

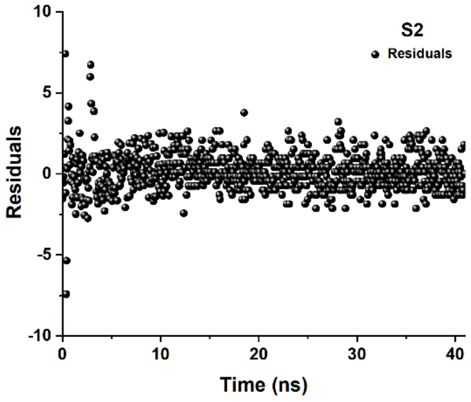

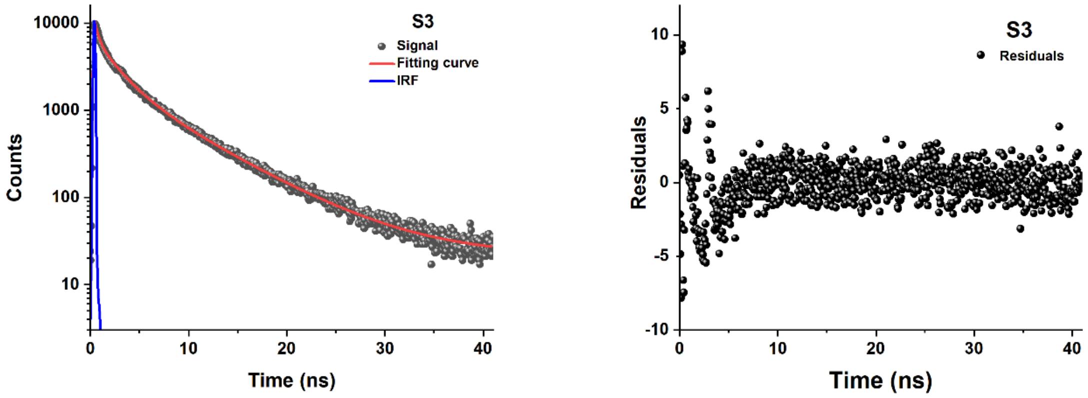

Figure 15. Fluorescence decay and residuals plot of the bulk porphyrin-loaded acetylated lignin nanoparticles **S1**, **S2**, and **S3** (IRF = Instrument Response Function).

Table 1. Average fluorescence lifetime values (τ). A corresponds to relative decay amplitudes.

| **Sample** | **$\tau_1$ (ns)** | **$A_1$ (%)** | **$\tau_2$ (ns)** | **$A_2$ (%)** | **$\tau_3$ (ns)** | **$A_3$ (%)** |
|---|---|---|---|---|---|---|
| **S1** | 0.499 | 89.6 | 1.45 | 10.4 | - | - |
| **S2** | 0.335 | 100.0 | - | - | - | - |
| **S3** | 0.371 | 44.2 | 2.12 | 37.2 | 6.75 | 18.6 |

Fluorescence decays of each sample were averaged after six accumulations, and then fitted with commercially-available SPCImage software, using proper mono- (Eq. 1), bi- (Eq. 2), or triple-exponential (Eq. 3) equations:

$$I(t) = A_1 \cdot exp\left(-\frac{t}{\tau_1}\right) \qquad \textbf{Eq. 1}$$

$$I(t) = A_1 \cdot exp\left(-\frac{t}{\tau_1}\right) + A_2 \cdot exp\left(-\frac{t}{\tau_2}\right) \qquad \textbf{Eq. 2}$$

$$I(t) = A_1 \cdot exp\left(-\frac{t}{\tau_1}\right) + A_2 \cdot exp\left(-\frac{t}{\tau_2}\right) + A_3 \cdot exp\left(-\frac{t}{\tau_3}\right) \qquad \textbf{Eq. 3}$$

where **$I(t)$** represents the photoluminescence intensity (a.u.), **$t$** denotes time (ns), **$\tau_1$**, **$\tau_2$**, **$\tau_3$** are lifetime components (ns), and **$A_1$**, **$A_2$**, and **$A_3$** are the relative decay amplitudes for the corresponding terms in the decay function.

Afterward, the intensity-weighted average fluorescence lifetime values were calculated, as follows:

$$\langle \tau \rangle = \frac{\Sigma A_i.\tau_i^2}{\Sigma A_i.\tau_i} \qquad \textbf{Eq. 4}$$

where **$\tau_i$** represents lifetime *i*-component (ns), **$A_i$** corresponds to a proper normalised amplitude, and **<τ>** denotes the calculated average lifetime (ns).

## 1.3 NON-LINEAR OPTICAL CHARACTERISATION

### *1.3.1 Femtosecond laser-induced fluorescence*

First, non-linear optical (NLO) performances of aqueous dispersions of the porphyrin-loaded and empty nanoparticles were studied in their crude product forms. More precisely, the femtosecond (fs) laser-induced fluorescence spectra of all three porphyrin-loaded hybrids and the empty acetylated lignin nanoparticles were measured at several excitation wavelengths (from 840 nm to 1080 nm). As depicted in Figure 16, each of the porphyrin-loaded acetylated lignin nanoparticles show ultrabroad complex emission bands with no excitation-dependent tendencies that lay in the red colour and NIR-I regions. The spectra of the fs laser-induced excitation, at wavelengths 740 nm and 770 nm, in the NIR-I region are displayed in Figure 17.

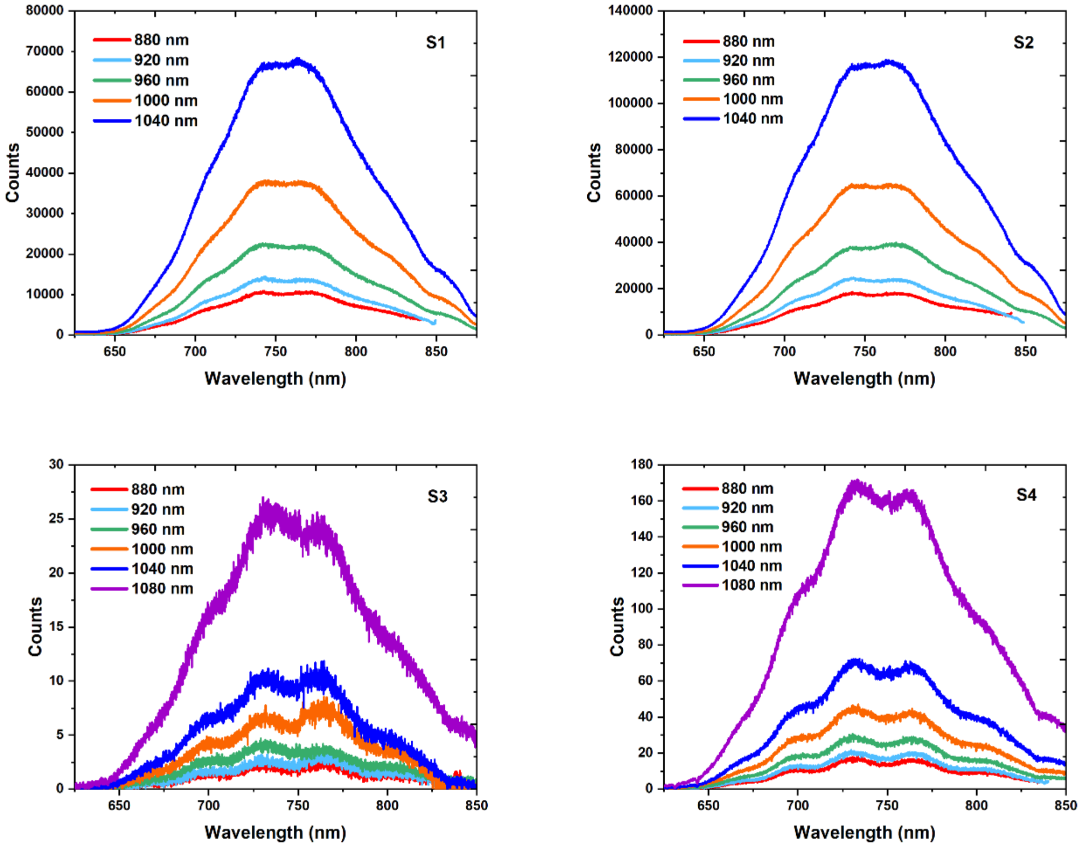

Figure 16. Femtosecond-laser induced fluorescence spectra of all four bulk aqueous dispersions (**S1**-**S4**). The excitation wavelengths are from 880 nm to 1040 nm in increments of 40 nm (**S1** and **S2**), and from 880 nm to 1080 nm in increments of 40 nm (**S3** and **S4**).

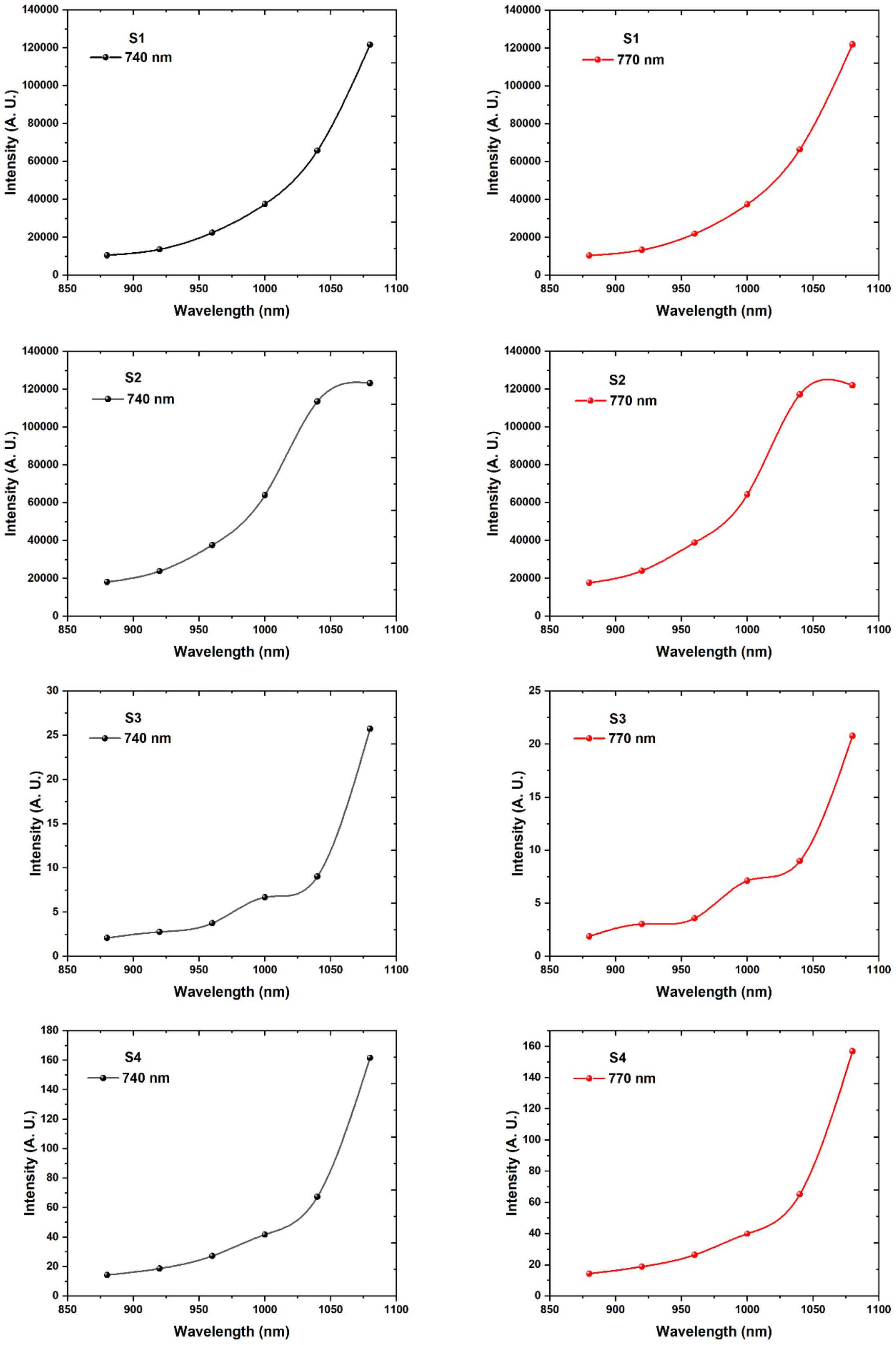

Figure 17. fs laser-induced excitation spectra in the NIR-I region (740 nm and 770 nm) of bulk dispersions **S1** – **S4**.

Interestingly, their spectral behaviour, including major fluorescence maxima peaks at *ca.* 740 nm and 770 nm, are similar to the emission signals arising from the porphyrin-free nanoparticles (**S4**), and thereby, they differ significantly compared to the one-photon excited fluorescence spectra (Figure 18).

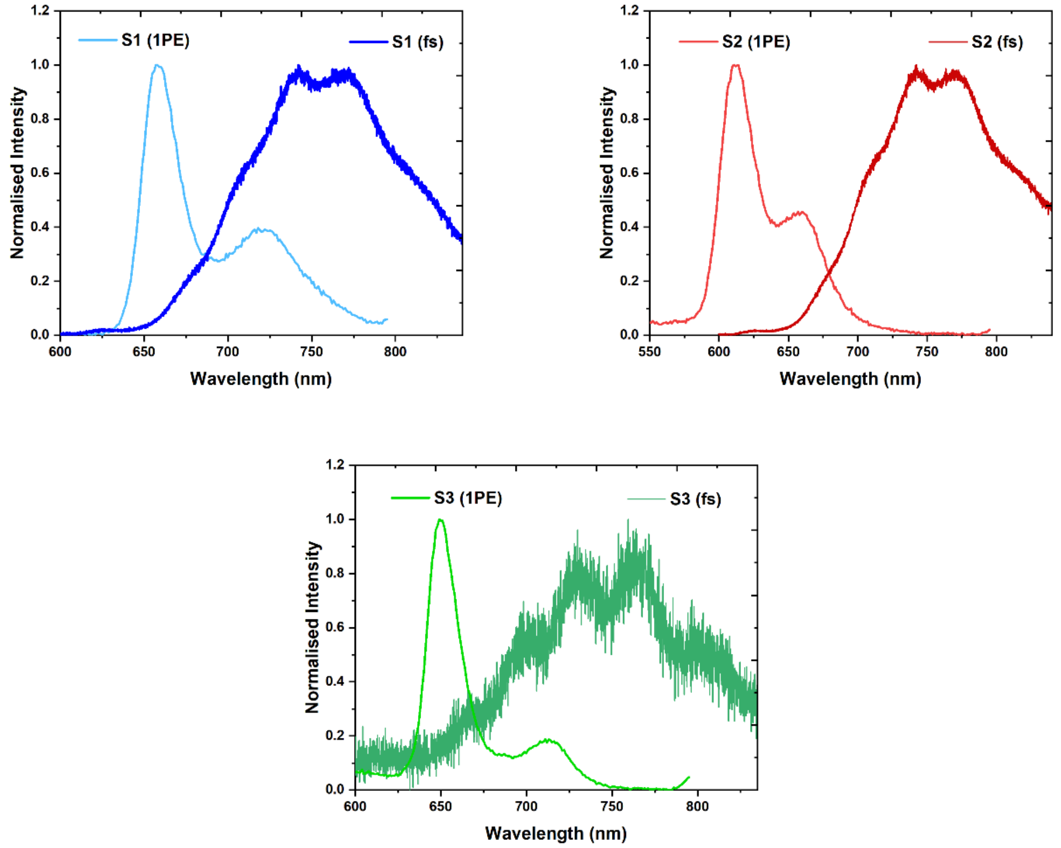

Figure 18. Combined one-photon excited (1PE) emission (left, $\lambda_{ex}$ = 420 nm) and femtosecond (fs) laser-induced emission (right, $\lambda_{ex}$ = 880 nm) spectra of bulk dispersions **S1** – **S3**.

To gain more details about the mechanism of the fluorescence process, femtosecond laser-induced emission intensity *vs* laser power at 880 nm were studied (Figure 19). As a result, the slope values were estimated to be around 1.0, ranging from 0.872 (**S2**) to 1.26 (**S4**) revealing that the emission of the hybrids may originate from complex deactivation pathways. We assume that the porphyrin loading is homogeneous, but these findings may be attributed to the existence of different morphologies, size distribution, and aggregates of the acetylated lignin nanoparticles in the bulk dispersions. These results indicated the need for the spectroscopic measurements to be performed on the separated fractions of the bulk hybrids.

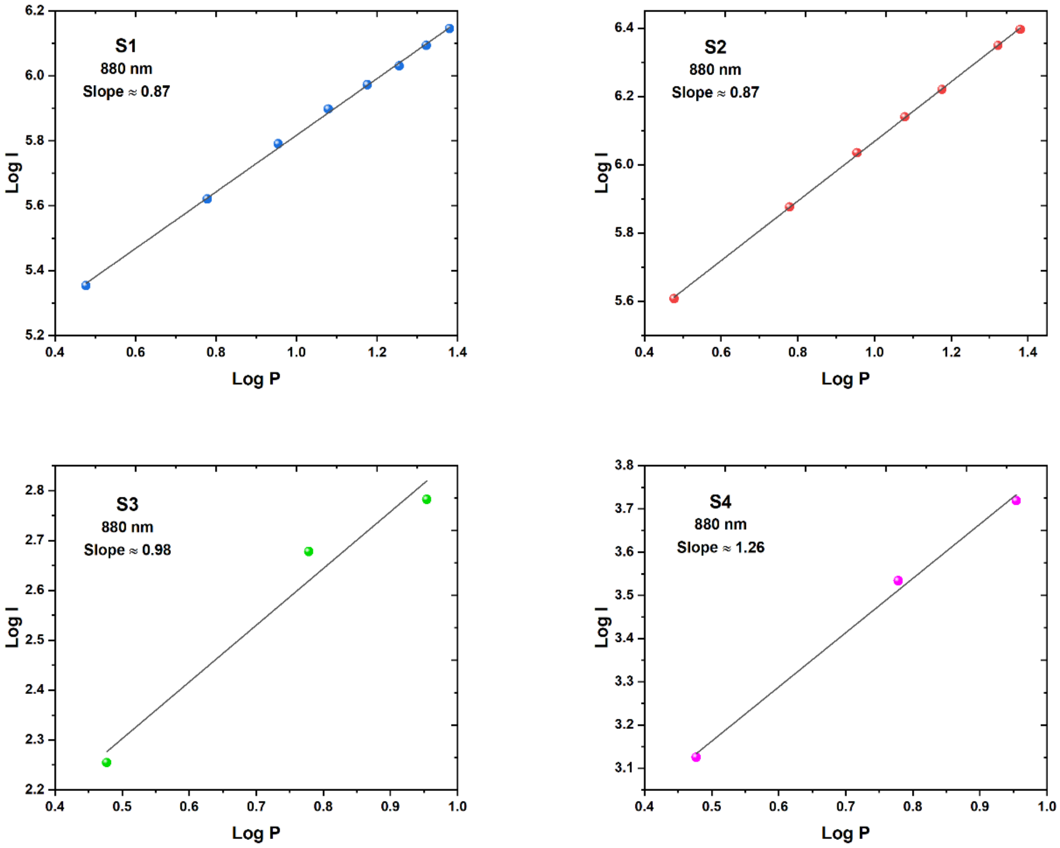

Figure 19. Power-dependence graphs of **S1**-**S4** in log-log scale, excitation wavelength = 880 nm. The slope indicates the nature of the process (number of photons absorbed simultaneously, one- or multi-photon).

Similar measurements, as previously described, were performed on the nanoparticles following the SDGC procedure. **S1-0**, **S1-10**, **S1-20**, **S4-0**, and **S4-10**, were irradiated by a femtosecond laser beam of wavelengths ranging from 840 nm to 1080 nm (Figure 20). All of the graphs, exhibit peaks in similar spectral localizations. Undeniably, the most effective emission is observed upon excitation at 1080 nm. Since the recorded spectra contain multiple components, these findings may be ascribed to the size distribution of the nanoparticles in the suspension as well as to their chemical complexity (*incl.* diverse J-aggregates of porphyrins in the nanoconjugates), allowing thereby their various hybrid forms to interact with each other and reveal distinct self-assemblies which result in complex emission pathways along with the plausible energy transfers and quenching processes. Further experiments would be required to confirm this with more certainty.

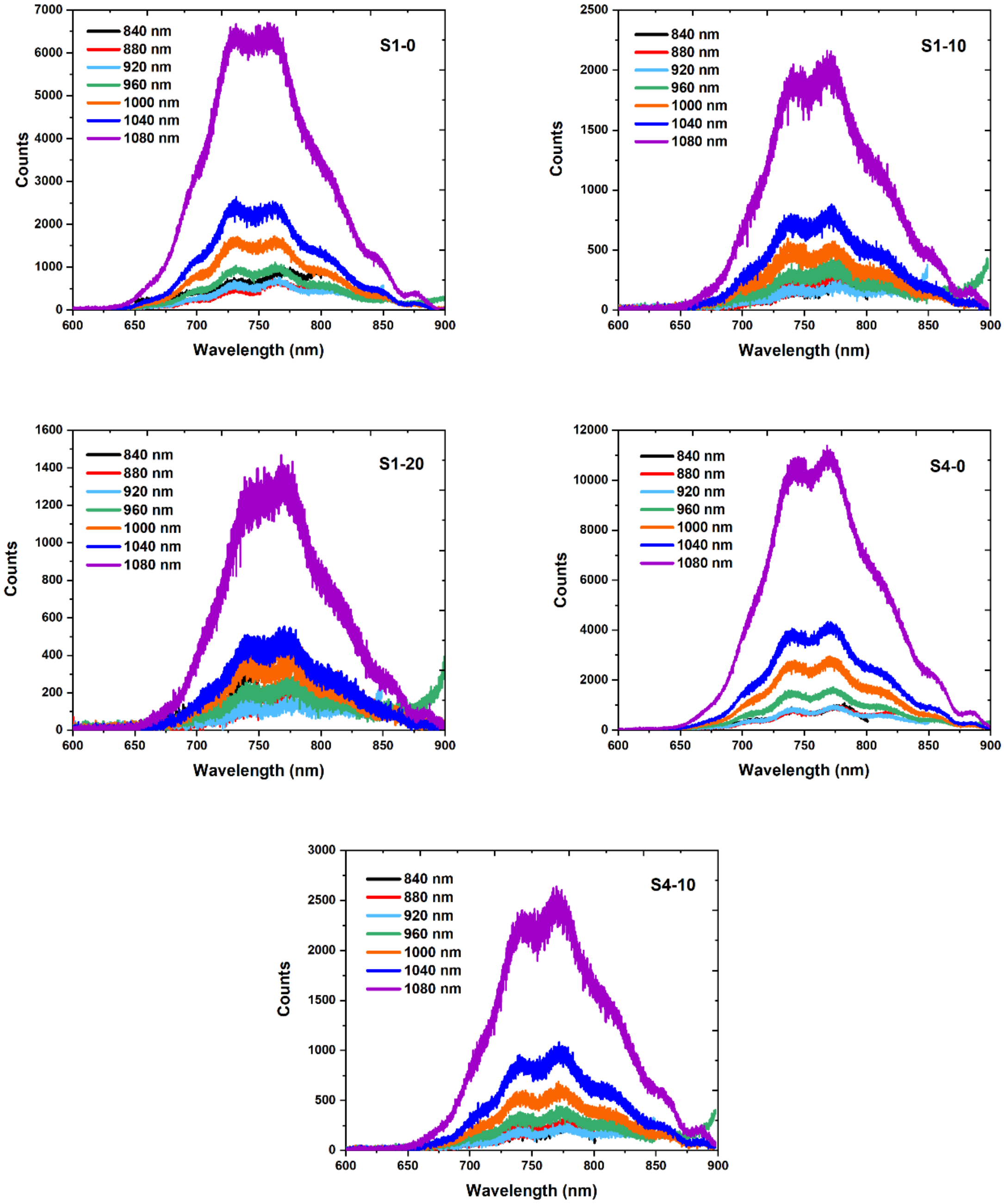

Figure 20. Femtosecond-laser induced fluorescence spectra of selected fractions after the SDCG procedure. The excitation wavelengths are from 840 nm to 1080 nm in increments of 40 nm.

To unravel the nature of the emission process, power-dependent measurements of the emission spectra for two excitation wavelengths (880 and 1080 nm, and power of 3 mW to 21 mW in increments of 3 mW) were performed (Figure 21). It appears that all of the recorded emission spectra are of a one-photon nature. Interestingly, the slope for the 880 nm excitation wavelength oscillates around 1.2, which indicates a non-negligible contribution of multi-photon processes.

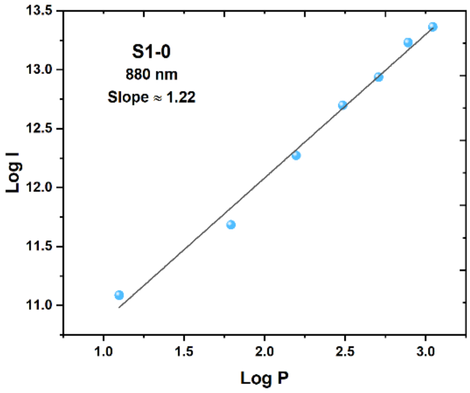
S1-0
880 nm
Slope ≈ 1.22
Log I
Log P
13.5
13.0
12.5
12.0
11.5
11.0
1.0
1.5
2.0
2.5
3.0

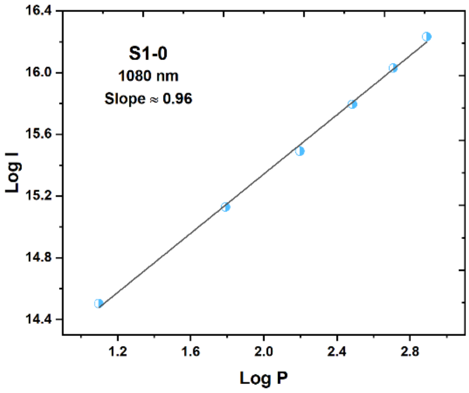
S1-0
1080 nm
Slope ≈ 0.96
Log I
Log P
16.4
16.0
15.6
15.2
14.8
14.4
1.2
1.6
2.0
2.4
2.8

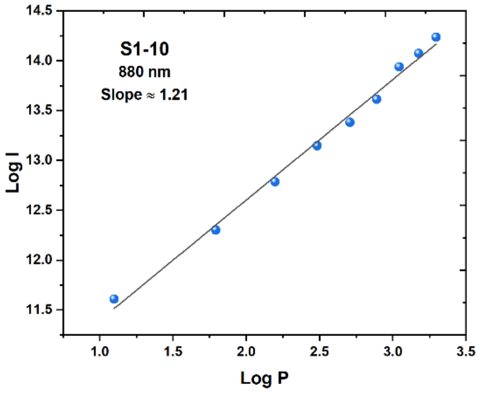
S1-10
880 nm
Slope ≈ 1.21
Log I
Log P
14.5
14.0
13.5
13.0
12.5
12.0
11.5
1.0
1.5
2.0
2.5
3.0
3.5

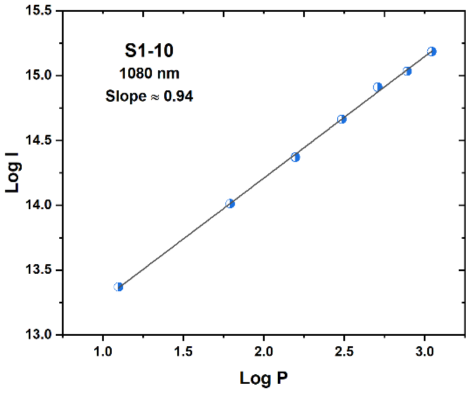
S1-10
1080 nm
Slope ≈ 0.94
Log I
Log P
15.5
15.0
14.5
14.0
13.5
13.0
1.0
1.5
2.0
2.5
3.0

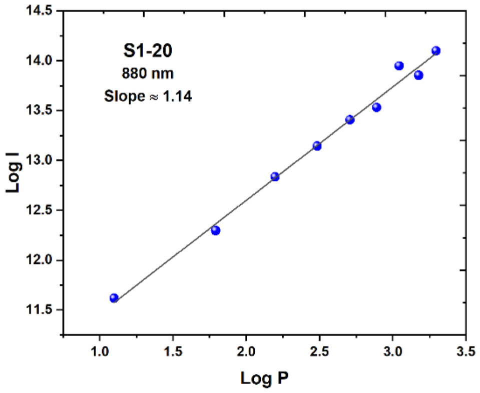
S1-20
880 nm
Slope ≈ 1.14
Log I
Log P
14.5
14.0
13.5
13.0
12.5
12.0
11.5
1.0
1.5
2.0
2.5
3.0
3.5

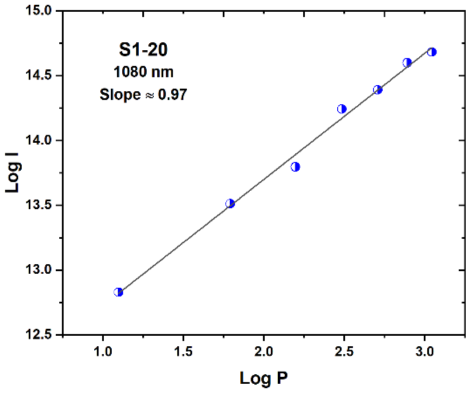
S1-20
1080 nm
Slope ≈ 0.97
Log I
Log P
15.0
14.5
14.0
13.5
13.0
12.5
1.0
1.5
2.0
2.5
3.0

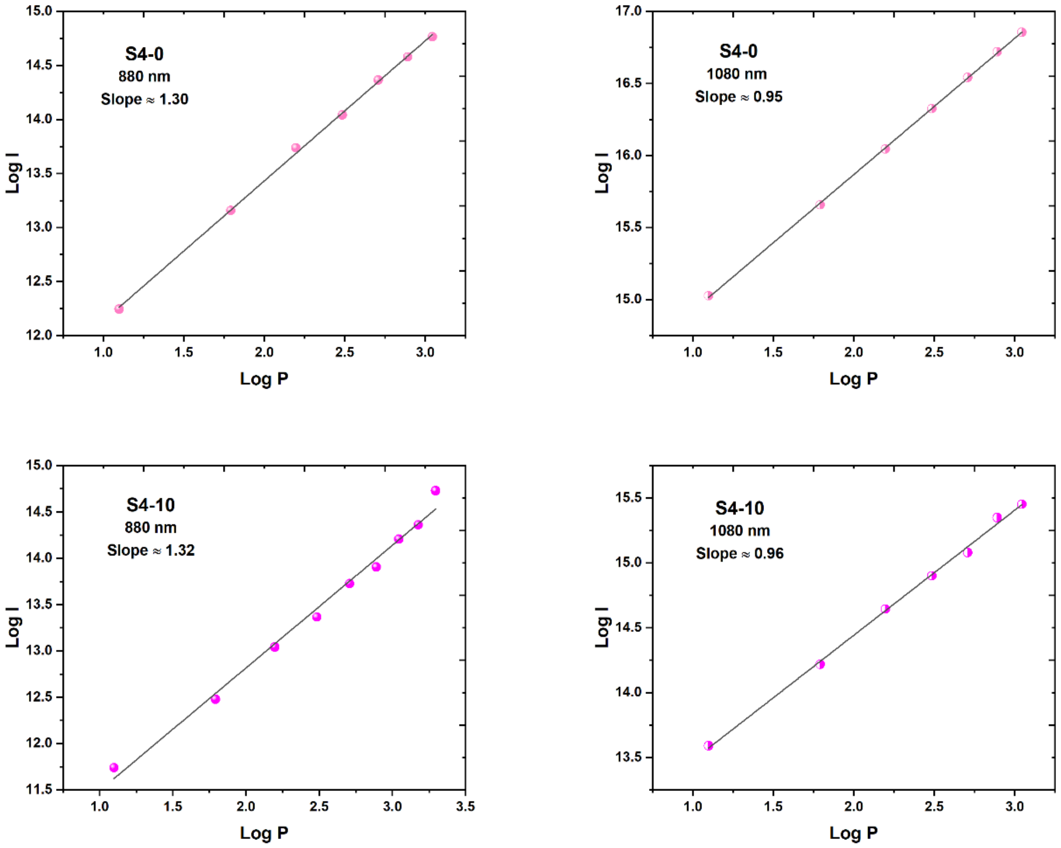

Figure 21. Power-dependence measurements for selected fractions after the SDCG procedure in log-log scale, excitation wavelength = 880 and 1080 nm. The slope indicates the nature of the process (number of photons absorbed simultaneously, one- or multi-photon).

### *1.3.2 Two-photon fluorescence microscopy (2PFM)*

The nonlinear optical responses of the select separated nanoparticle fractions that were deposited on coverslips, were epi-collected by a x100 oil immersion objective, under 910 nm excitation. Maps of the intensity of luminescence of **S1-0** and **S1-20** are shown in Figure 22. The samples are prepared similarly to those for AFM, a droplet containing the nanoparticles is deposited onto a coverslip and left to dry at a 45° angle. This preparation method allowed for well-dispersed particles on the glass substrate enabling the collection of emission from a single nanoparticle. The investigated structures are shown as bright spots on the luminescence intensity maps. From the maps, it is clear that the particles in sample **S1-20** are distinctly larger than those observed in **S1-0**, however, there was no significant difference in the intensity of the luminescence.

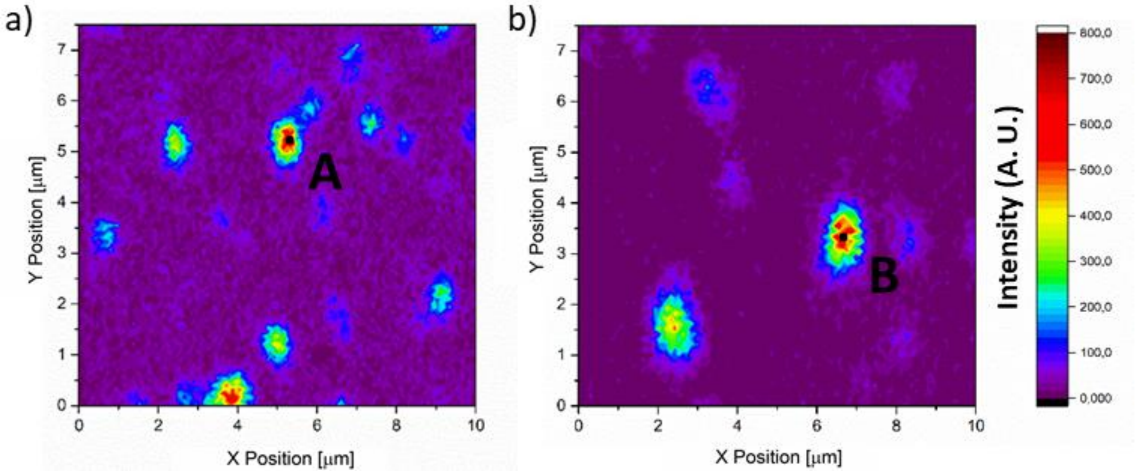

Figure 22. Maps of two-photon excited luminescence signal taken within the **S1-0** (a) and **S1-20** (b) deposited on the glass substrate. Excitation wavelength = 910 nm and the power of the incident laser on the sample was adjusted to 80 µW.

Two-photon excited (2PE) emission was measured at two different points, as marked in Figure 22 points A and B. The 2PE emission spectrum can be seen in Figure 23 (a), it should be noted that the characteristic peaks for the particles on the glass substrate (**S1-0** and **S1-20**) are spectrally, minimally, shifted compared to the locations of those for the porphyrin-loaded nanoparticle bulk dispersion (**S1**). The particles in the separated fractions (on the glass substrate) still display the two characteristic emission peaks as observed for the corresponding hybrids suspension (**S1**). For example, in the 1PE fluorescence spectrum of **S1**, the peaks are located at 658 nm and 722 nm, with the components of the 2PE fluorescence spectrum of *i.e.*, **S1-20**, positioned at 655 nm and 738 nm (Figure 23 (a)). Seeing that these spectral results are taken from a single nanoparticle, it is confirmed that the 2PE fluorescence observed on the intensity map corresponds to the porphyrin-loaded acetylated lignin nanoparticle.

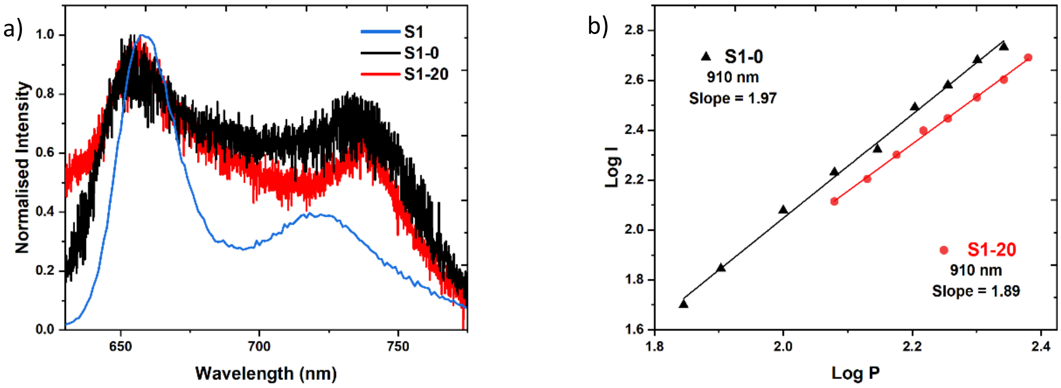

Figure 23. (a) Normalised one-photon excited emission spectrum of the bulk dispersion **S1** (blue, $\lambda_{ex}$ = 420 nm) and normalised two-photon excited emission spectra of a single porphyrin-loaded acetylated lignin particle from **S1-0** and **S1-20** (black and red, $\lambda_{ex}$ = 910 nm). The laser power during the measurements was adjusted to 1 mW. (b) The log-log plots of luminescence signal vs. incident laser power performed on a single nanoparticle from the different fractions: **S1-0** (black line and triangles, slope = 1.97±0.07) and **S1-20** (red line and circles, slope = 1.89±0.04).

Additionally, the development of the fluorescence intensity as a function of excitation power was measured to determine the mechanism of excitation for the same samples (**S1-0** and **S1-20**), as was measured for the bulk dispersions and separated suspensions. The excitation beam ($\lambda_{ex}$ = 910 nm) focused on a single nanoparticle and the signal was collected for 10 seconds at a constant power of 1 mW. The median values of the emission signal collected for different average powers were plotted as a function of intensity vs power (Figure 23 (b)). For each sample, the slope values of the log-log plots are close to 2.0 (**S1-0** = 1.97 and **S1-20** = 1.89) confirming that excitation of a single particle involves a two-photon process.

Furthermore, the differences between the spectra displayed in Figure 23 (a) suggests that there may be various forms of the porphyrin-loaded acetylated lignin nanoparticles present. Such as the aforementioned self-assemblies, or agglomerations of nanohybrids that occur in the bulk dispersions, and complex interactions may also appear between the nanoparticles themselves. [148, 149]

## 1.4 CONCLUSION AND OUTLOOK

The femtosecond laser-induced emission of bulk dispersed and single porphyrin-loaded acetylated lignin nanoparticles were measured. The results from these initial experiments show promise for the use of these nanoparticles as remarkable biomarkers that are capable of emitting in the NIR range, most significantly within the first biological optical window, as demonstrated particularly well with the single nanoparticle measurements. The observable femtosecond laser-induced emission can be utilised in the distribution and monitoring of these formulations. Future work needs to be done regarding the singlet oxygen generation capabilities of the bulk dispersions, as well as the separated fractions, to determine their usefulness within 2PA-PDT, theranostic applications, and more.

In order to ascertain and further develop our understanding of the results we observe here, additional experiments will need to be performed. Especially, microscopic measurements of the bulk aqueous dispersions in order to fully compare the established results presented in this work, as well as the remaining separated samples, to provide a fuller picture.

# Chapter II:

## Non-linear optical properties of Foscan® (*m*-THPC) and derivatives

## INTRODUCTION

As indicated in the introduction, the excitation of a chromophore/photosensitizers (PS) may occur not only by the common one-photon absorption (1PA), but can also occur by a two-photon absorption (2PA) process. As previously mentioned, this is the process of the simultaneous absorption of two lower energy photons to provide the transition energy. The dependence of the rate of generation of the excited states is quadratic for the two-photon process, and linear for the absorption process of a single, higher energy photon. The two-photon process also differs in the requirements of short-pulse lasers, and longer wavelengths, for excitation.[38] The combination of 2PA and photodynamic therapy (PDT) allows for improved treatment efficacy, tumour targeting, and the use of longer wavelength excitation for deeper tissue penetration (refer back to the introduction for details).[150]

The determining factor for the appropriateness of a photosensitizer for its use within two-photon absorption combined PDT (2PA-PDT) is its 2PA cross-section value. The absorption cross-section value is a measure of the probability of an absorption process, in this case the two-photon absorption process.[38, 40] The 2PA cross-section is usually experimentally determined in one of the two alternative ways: by the Z-scan method, or by two-photon excited fluorescence (2PEF) measurements. Z-scan is a measurement based on the light transmittance as a function of the position of the sample along the z-axis as it travels along a focused laser beam.[151, 152] The 2PEF technique is based on the intensity of the two-photon induced fluorescence as a function of the excitation intensity.[132, 133] Both techniques have their drawbacks, but have both shown to be reliable in their respective uses. 2PA cross-sections that are measured using the Z-scan technique often tend to present higher values than the other technique, this may be due to the presence of non-linear scattering or other optical loss processes in the sample during a measurement. A drawback of 2PEF is that this technique can only be applied to molecules that are significantly fluorescent and the measurement wavelength range cannot overlap with the 1PA regions. 2PEF is usually preferred to be performed on species that have a relatively high luminescence quantum yield. 2PEF experiments are typically carried out by comparing the signal of an investigated sample to a well-studied reference fluorescent dye. This avoids the need for exact knowledge of variables that are dependent on the laser beam (geometry, pulse duration, *etc.*).[40]

The desired properties of PSs for two-photon induced PDT have been extensively reviewed and determined in various literature studies.[39, 67, 153] Of the variety of modifications, one such example obtains large enhancements of 2PA properties by increasing the size of the π-electron system, as well as the distance between a donor (HOMO) and an acceptor (LUMO) moiety.[154, 155]

The photosensitizer (PS) is a key component of PDT. 5, 10, 15, 20-tetra(*m*-hydroxyphenyl) chlorin (***m*-THPC**, Figure 24), was registered as the drug formulation Foscan®, is a second-generation PS that is used in PDT applications. [156, 157] It was approved for use in the EU in 2001, for the palliative treatment of head and neck cancers.[158] Foscan® is part of a family of reduced porphyrins that was first synthesised by Bonnett *et al.*, more than 30 years ago.[159] Although Foscan® is one of the most commonly used PSs for PDT treatment, it isn't without its drawbacks. There are several limitations including its limited solubility in aqueous media causing aggregation, non-specific accumulation meaning it accumulates in more than one area of the body, and it also causes prolonged light sensitivity. With modifications made to the ***m*-THPC** core of Foscan® there is the possibility to enhance its use for two-photon applications, thus, reducing the drawbacks associated with Foscan® and improving treatment efficacy.

Herein, we demonstrate the application of simple modifications and their resulting enhanced 2PA properties.[160] It was decided that simple modifications would be made to the terminal groups of ***m*-THPC** to enhance its 2PA properties, as a starting point. Prior to the linear and non-linear measurements, substitution, esterification, and Sonogashira cross-coupling reactions were utilised to produce aldehyde and carboxylic acid derivatives of ***m*-THPC** (**PS1**, **PS3**, and **PS5** and their synthetic pathway are described in Figure 24). These moieties were chosen not only for possible 2PA enhancements, but also for their suitability in the design of drug delivery systems, including inorganic nanoparticles and hydrogels.[161-163]

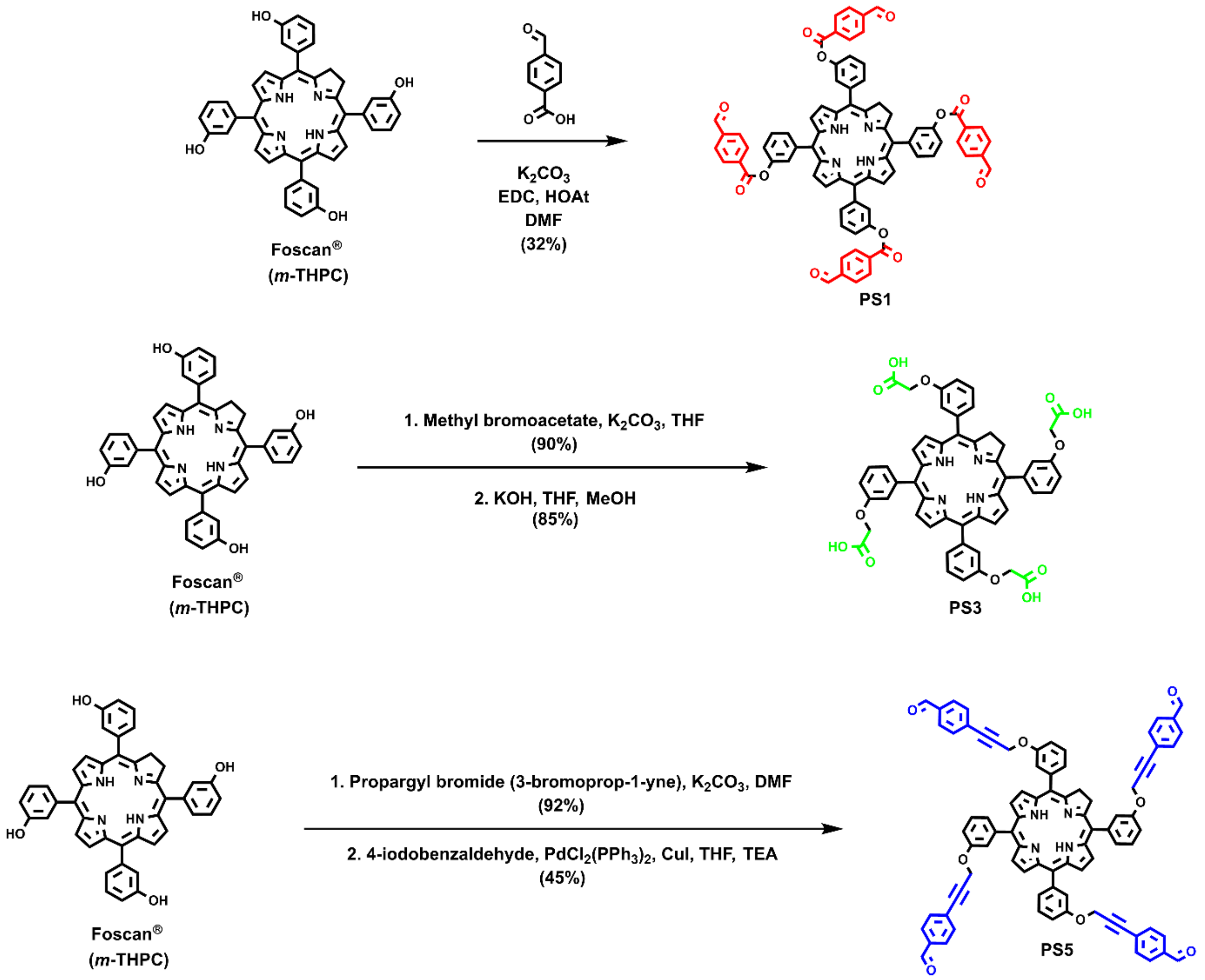

Figure 24. Reaction scheme utilised by our collaborators in the synthesis of **PS1**, **PS3**, and **PS5** (for demonstrative purposes). EDC refers to 1-ethyl-3-(3-dimethylaminopropyl)carbodiimide and HOAt refers to 1-hydroxy-7-azabenzotriazole.

Linear photophysical measurements (UV-Vis absorption) were done on the four PSs prior to their non-linear measurements. Non-linear photophysical measurements were performed to determine the 2PA cross-section value of each PS, in this instance the two-photon excited fluorescence technique was utilised. The results here confirm the potential application of **PS1**, **PS3**, and **PS5** within 2PA-PDT. This work was done in collaboration with Senge and Gomes-da-Silva.[160] Foscan®, **PS1**, **PS3**, and **PS5** were provided for the measurements discussed hereafter.

## 2.1 TWO-PHOTON EXCITED FLUORESCENCE (2PEF)

### *2.1.1 Two-photon absorption cross-section values*

To gain further information regarding the 2PA properties of our molecules, the 2PA cross-section values ($\sigma_2$) were estimated by 2PE emission measurements. 2PE emission spectra were recorded on a custom-built experimental setup, consisting of a spectrometer (Shamrock 303i, Andor) equipped with an ultrasensitive camera (iDus camera, Andor). All samples were excited with a Ti:Sapphire Chameleon laser (Coherent Inc.), over the wavelength range of 820 nm to 1080 nm (the repetition rate 80 MHz and the pulse duration ≈120 fs). The corresponding absorbance values in the emission region were kept below 0.1 by adjusting the relative molar concentrations. This allows us to minimise any undesired effects, such as reabsorption and aggregation. The photostability of each compound was monitored, via UV-Vis absorption and 1PE fluorescence measurements, periodically throughout the 2PE emission measurements. All spectroscopic measurements were performed in dimethylformamide (DMF) at room temperature. The 2PA cross-section values ($\sigma_2$) were determined using the commercially available dye LDS-698, in chloroform, as the reference.[164] The calculated $\sigma_2$ values for each PS are displayed in Figure 25, with the most representative parameters at the 2PA maxima being displayed in Table 2.

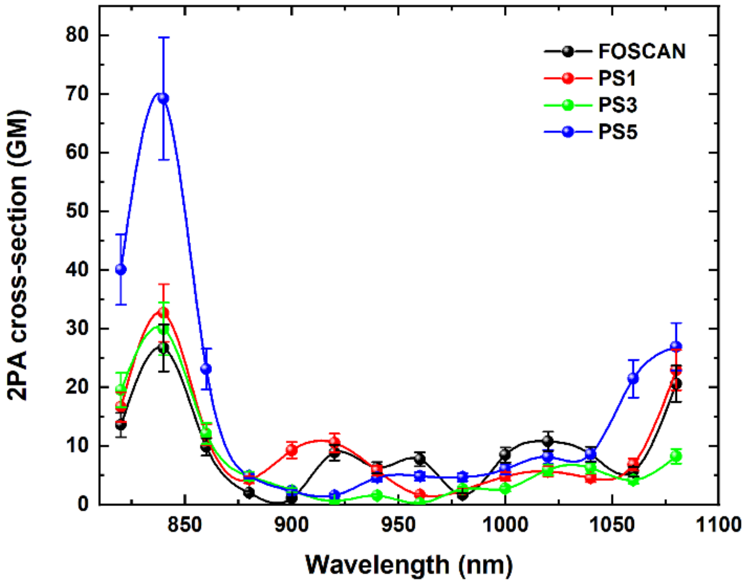

Figure 25. Spectra of the calculated 2PA cross-section values of Foscan®, **PS1**, **PS3**, and **PS5** over the wide wavelength range from 820 to 1080 nm (20 nm intervals) in DMF.

Table 2. 2PA cross-section values ($\sigma_2$) and normalised 2PA cross-section values ($\sigma_{2\ \mathrm{norm.}}$) of Foscan® and derivatives in DMF ($\lambda_{exc}$ = 840 nm).

| PS | $\sigma_2$ [GM] | $\sigma_{2\ \mathrm{norm.}}$ [GM/Da] |
|---|---|---|
| **Foscan®** | 26.7 ± 4.0 | 0.039 |
| **PS1** | 32.7 ± 4.9 | 0.048 |
| **PS3** | 30.0 ± 4.5 | 0.033 |
| **PS5** | 69.3 ± 10.0 | 0.056 |

2PA cross-section values were calculated from the 2PE emission measurements using LDS 698 in chloroform as a reference, following Equation 1:

$$\sigma_{2,sam}\ [\mathrm{GM}] = \sigma_{2,\ ref}\ \frac{I_{sam} C_{ref} n_{ref}^2 \Phi_{ref}}{I_{ref} C_{sam} n_{sam}^2 \Phi_{sam}} \quad \text{(Eq. 1)}$$

where *I* is the integrated emission intensity, *C* is the molar concentration, ϕ is the 1PE fluorescence quantum yield, and *n* is the refractive index of solvent. '*sam*' refers to sample and '*ref*' refers to reference.[165-167] The normalised $\sigma_2$ values ($\sigma_{2\ \mathrm{norm.}}$) were estimated, following Equation 2, where *M* denotes the molecular weight of the compounds.

$$\sigma_{2\ norm.,sam}\ [\mathrm{GM/M}] = \sigma_{2,sam} / M \quad \text{(Eq. 2)}$$

The 1PA and 2PA spectra of ***m*-THPC** and the derivatives are compared in Figure 26. There is good overlap between the Soret band and the major 2PA peak around double its wavelength, 420 and 840 nm, respectively. Due to their very similar spectral behaviour, as well as the non-centrosymmetric design of the molecules, it can be concluded that the 1PA and the 2PA process may reach the same excited state. The possibility of partial re-absorption of the emission taking place during the 1PA process corresponds to the observed small red-shift in the 2PA spectra. This phenomenon is related to the light beam and its different penetration depths.[168] Furthermore, the photosensitizers display weaker 2PA cross-section values (~ 10 – 20 GM) in the longer wavelength region, above 1000 nm. These lower cross-section values are related to the Q-bands from the one-photon transitions.

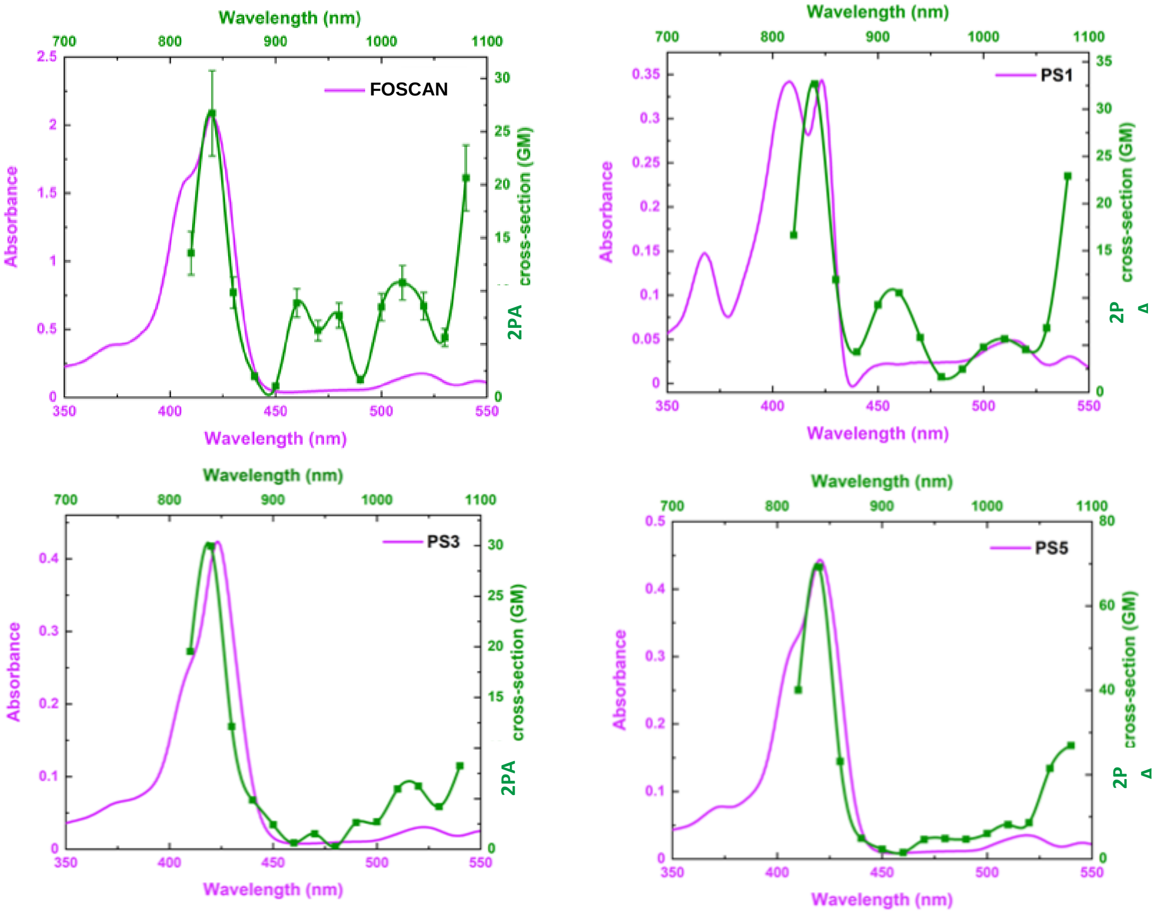

Figure 26. Overlayed 1PA and 2PA spectra of each compound (Foscan®, **PS1**, **PS3**, and **PS5**) at the concentration of $10^{-6}$ M, all in DMF.

The 2PA cross-section values follow the trend **PS5** > **PS1** > **PS 3** > ***m*-THPC**. As previously mentioned, it is well-known that extension of the π-conjugation length typically leads to enhancements in the 2PA properties of molecules.[66, 169, 170] This effect is observed here between **PS1** and **PS5**, we change from carbonyl to alkyne linkers, resulting in a significant enhancement in the 2PA cross-section value from 32.7 to 69.3 GM. Direct *meso*-substitution of the functional groups to the porphyrin core, has also been shown to have a positive enhancement on 2PA properties, despite being of some hinderance to conjugation, as reported in the literature.[88]

The observed differences in 2PA cross-section values are most likely due to the differing terminal electron accepting groups. The aldehyde function in **PS1** and **PS5** is more strongly electron accepting than the carboxyl group in **PS3**. Each of the derivatives are designed in a donor-acceptor (D-A) motif, the differing acceptor strengths may also have an effect on the extent of charge transfer from the centre of the molecule. There have been previous studies that also report significant 2PA cross-section enhancement due to the D-A configuration,[68, 171] as seen in **PS1**, **PS3**, and **PS5**. Such simple modifications of ***m*-THPC** have led to the 2.6-fold enhancement of the 2PA cross-section value (λ = 840 nm) of **PS5** (69.3 ± 10.0 GM) compared to the unmodified ***m*-THPC** (26.7 ± 4.0 GM). The variation in molecular structures of ***m*-THPC**, **PS1**, **PS3**, and **PS5** also induces different 2PA properties in the Q-band regions, at double the excitation wavelength, as shown in Figure 26 (green line).

Even though ***m*-THPC** and derivatives are known strong emitters and innovative PSs, there is limited attention and little to no exploration of their two-photon and multi-photon absorption properties. Other than the measurements reported here, the 2PA spectrum of ***m*-THPC** in the Q-band region (1050 – 1450 nm), as well as around the Soret band, using the Z-scan open aperture technique was reported by Hamed, et al., in 2014.[65] The 2PA cross-section values were reported as 28 GM (775 nm) and 20 GM (1320 nm) in DMSO. There has been one previous report where the 2PA cross-section of ***m*-THPC** is measured via 2PE fluorescence at the single excitation wavelength of 800 nm,[172] with the measured 2PA cross-section of ***m*-THPC** being 18 GM in a solvent mixture of ethanol (20%), polyethylene glycol (30%), and distilled water (50%).

### *2.1.2 Power dependence measurements*

As has been done in previous reports,[173-175] power dependence measurements of emission intensities at 840 nm were performed. In this series of measurements, the 2PE fluorescence spectra of ***m*-THPC**, **PS1**, **PS3**, and **PS5** were recorded with varying laser excitation power ranging from 2.5 mW to 40 mW. The corresponding logarithmic plots of input power (log P) vs. emission intensity (log I) are shown in Figure 27, below. The slope values were measured to be 1.87, 1.79, 1.80, and 1.78, for ***m*-**

**THPC**, **PS1**, **PS3**, and **PS5**, respectively. These values indicate a quadratic power relation, thus, confirming a two-photon process is occurring.

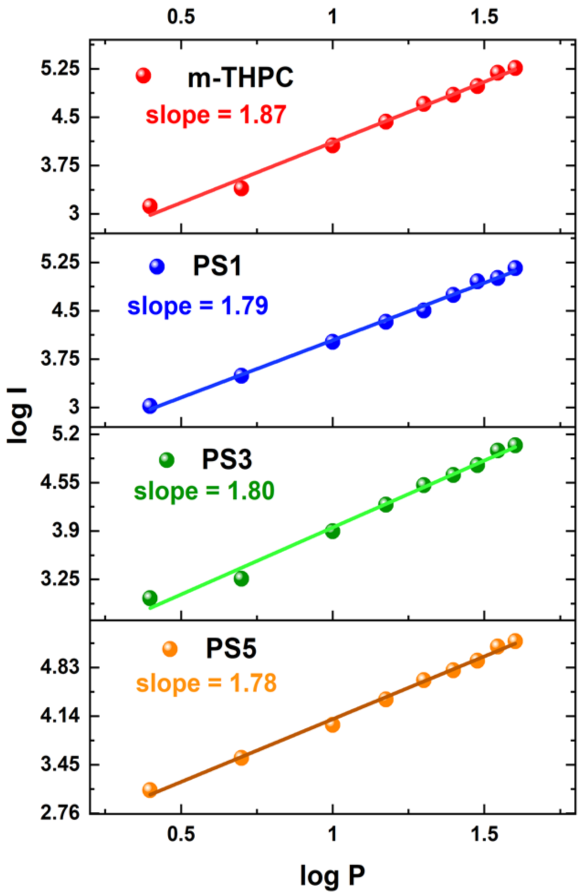

Figure 27. Power dependence graphs for *m*-THPC, **PS1**, **PS3**, and **PS5** (λ = 840 nm). Slope of each graph are 1.87, 1.79, 1.80, and 1.78, respectively.

## 2.2 TRANSFER EFFECT FROM DMF TO AQUEOUS SOLUTION

The intense red fluorescence that each PS produces upon two-photon excitation shows great potential for these compounds to be used as 2PE fluorescence imaging agents. We can further test this by changing the media that the compounds are measured in. Due to the addition of carboxyl groups to the *meso*-phenyl rings aids in the solubilisation of **PS3** in aqueous media without any further pre-treatments, its 2PE fluorescence was measured again in pH 7.2, buffer solution. There are spectral differences observed between the organic solvent (DMF) and aqueous (buffer solution) media (Figure

28). The emission that dominates in buffer solution is more red-shifted (~ 670 nm) compared to the one that dominates in DMF (~ 655 nm). This may be indicative of the considerable contribution that H-like agglomerates may have to the 2PE fluorescence. Having said that, the fact that there is significantly strong red 2PE fluorescence occurring in physiological conditions demonstrates the potential of **PS3** in biomedical applications.

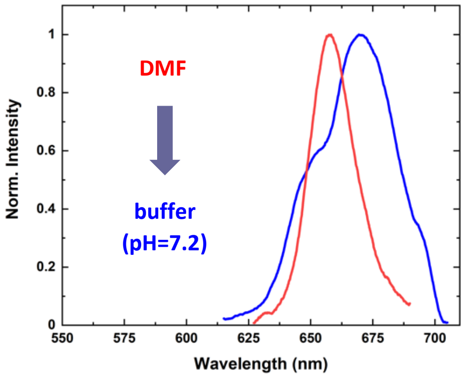

Figure 28. Transfer effect on the 2PE fluorescence spectra from DMF to buffer solution (pH = 7.2) of **PS3**.

## 2.3 CONCLUSION & OUTLOOK

Following the modification of the ***m*-THPC** skeleton via introduction of aldehyde and carboxylic acid groups, their linear and non-linear photophysical properties were measured. Two-photon excited fluorescence measurements (in DMF) were performed on ***m*-THPC**, **PS1**, **PS3**, and **PS5**, the results showed that even simple modifications could lead to an improvement on the 2PA properties. This was confirmed by the determination of the 2PA cross-sections. In particular, **PS5** with its alkyne linkers between the core and the newly introduced carbonyl groups, indicated a 2.6-fold increase at the 2PA maxima compared to the unmodified ***m*-THPC** core. Additionally, the results of **PS3** demonstrating fluorescence in aqueous media upon two-photon excitation furthers the capabilities for this PS to be used not only in 2PA-PDT, but also potential as fluorescence imaging probes.

Future work will include *in vitro* and *in vivo* studies to determine if the photosensitivity of the modified derivatives (**PS1**, **PS3**, and **PS5**) has been altered compared to the parent compound, ***m*-**

**THPC**. It is hoped that the derivatives described here will allow for the excitation of PSs at longer laser wavelengths, allowing for deeper tissue penetration, and thus, allowing for higher therapeutic response and lower light sensitivity that comes with Foscan® treatment. The PSs that have limited solubility in aqueous media (**PS1** and **PS5**) may also be included in the development of systems combining PSs and nanoformulations/nanoparticles. It is clear from the 2PA cross-section results here that these PSs show good promise for the development of two-photon induced PDT.

# Chapter III:

## Synthesis and characterisation of functionalised porphyrin for prospective use in PDT/PACT

## INTRODUCTION

Our initial goal was to make chemical modifications to a porphyrin, in order to increase the π-conjugated system. As seen in several reviews,[39, 67, 176, 177] extension of the π-conjugation system has shown positive effects on the 2PA properties of porphyrins and other photosensitizer molecules. A synthetic route was designed to synthesise a para-substituted pyrimidine functional group (**ER-7** and **ER-7-I**). Pyrimidine is an electron-rich aromatic ring and commonly undergoes meta-substitution. However, meta-substitution is not as beneficial as para-substitution in improving π-conjugation. Therefore, it was decided to synthesise the novel 2-(4-bromophenyl)-5-iodopyrimidine and coupled it with porphyrin core through conjugated spacer for this particular project. The target compounds structures are shown in Figure 29.

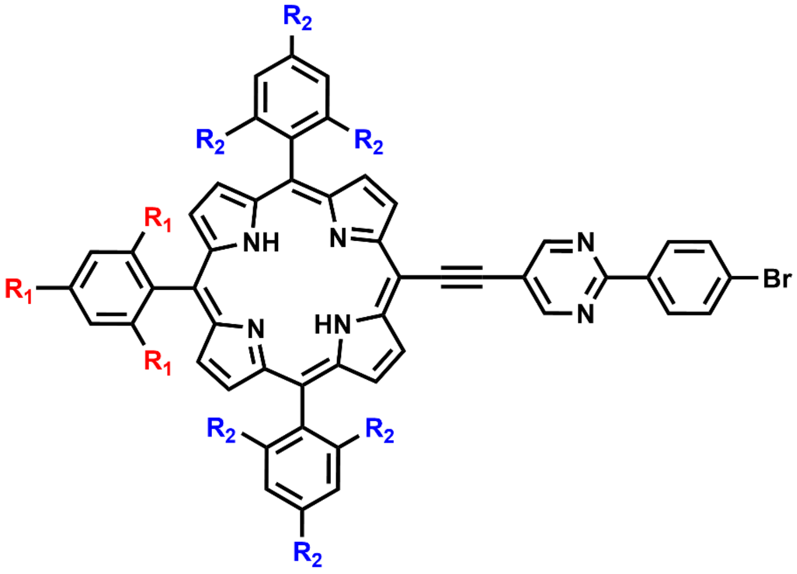

**ER-7**
$R_1$ = $CH_3$
$R_2$ = H

**ER-7b**
$R_1$ = $R_2$ = $CH_3$

Figure 29. Structures of the targeted compounds (**ER-7** and **ER-7b**).

For coupling purposes, the porphyrin cores need to bear either iodine or acetylene. The synthesis of the porphyrin core, as well as of the pyrimidine, have been optimised for efficiency and yield. The compounds synthesised in this chapter are shown in Figure 30.

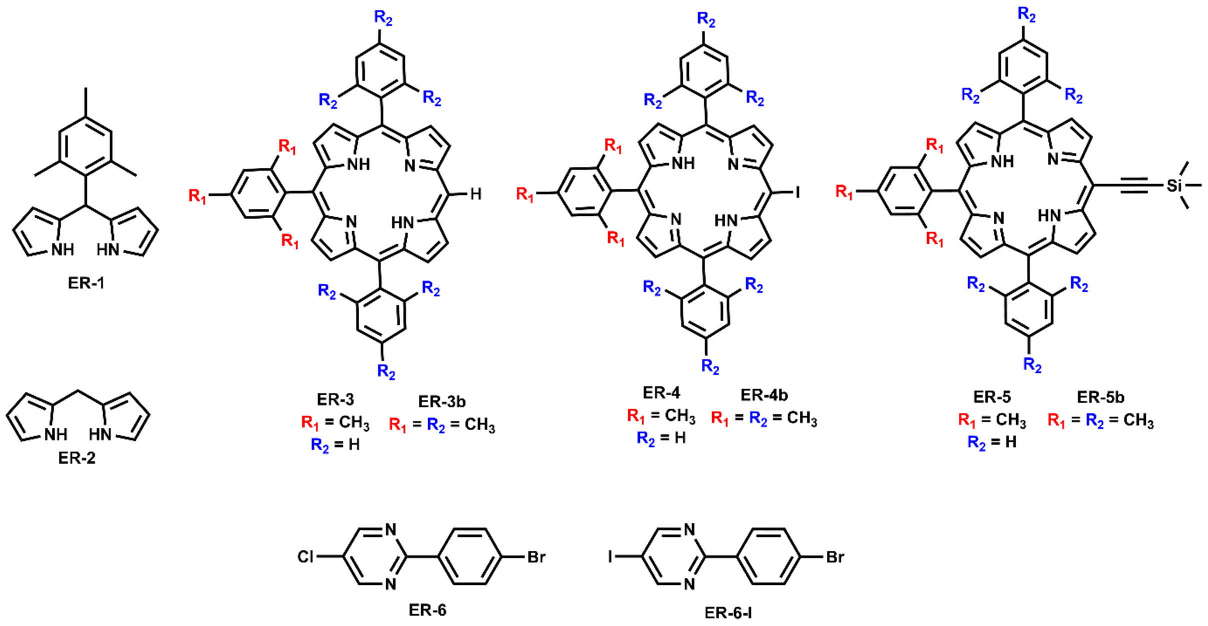

Figure 30. Structures of the target precursors.

The retrosynthetic pathways of the compounds are shown in Figure 31. The key synthons are the porphyrin core (**ER-3** or **ER-3b**, **ER-4**, and **ER-5**) and the iodinated para-substituted pyrimidine (**ER-6-I**). Different condensation reaction conditions were explored to determine the most effective route. Also, different iodination reaction conditions were tested to determine the best conditions for successful iodination of **ER-6**.

Firstly, the synthesis of porphyrinic synthons will be described, followed by the synthesis of ER-6 and ER-6-I. Characterisation (NMR, UV-Vis, Mass Spectrometry, and 2PA properties) will also be detailed in the following discussion. Finally, we will discuss the outcomes of the performed synthesis and the characterisation of the materials, as well as the outlook and future prospects of the compounds.

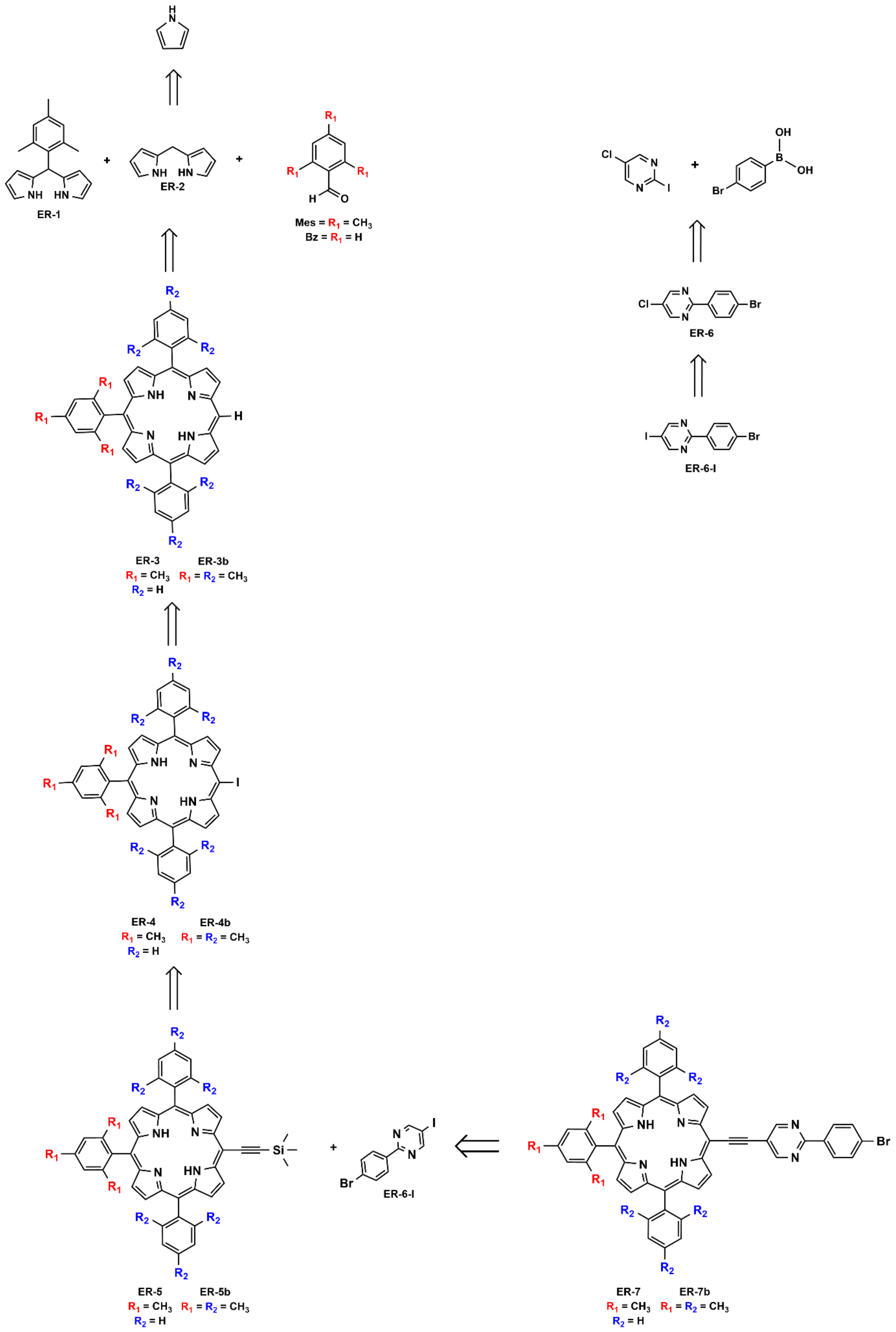

Figure 31. Retrosynthetic pathway of the synthetic strategy for **ER-7** and **ER-7b** (Mes = mesitaldehyde, Bz = benzaldehyde).

## 3.1 SYNTHESIS OF THE PORPHYRIN BASE (ER-3 and ER-3b)

Both synthesis methods of the porphyrin base are based on the Lindsey method, previously described in various literature.[178] The prior synthesis of the two dipyrromethane compounds (**ER-1** and **ER-2**) have also been previously described in the literature.[179, 180] The two dipyrromethanes are reacted together to form the porphyrin core (di-mesityl-phenyl-porphyrin). With the partial preservation of mesityls, the phenomenon of scrambling can be mostly avoided. This phenomenon can lead to modification of the photophysical properties of photosensitizers, such as reducing the quantum yields of singlet oxygen production/fluorescence.[181]

### *3.1.1 Dipyrromethane synthesis*

The synthesis of each dipyrromethane (**ER-1** and **ER-2**) consists of reacting the aldehyde (mesitaldehyde and formaldehyde) in the presence of an excess of pyrrole in an acidic medium (Figure 32).

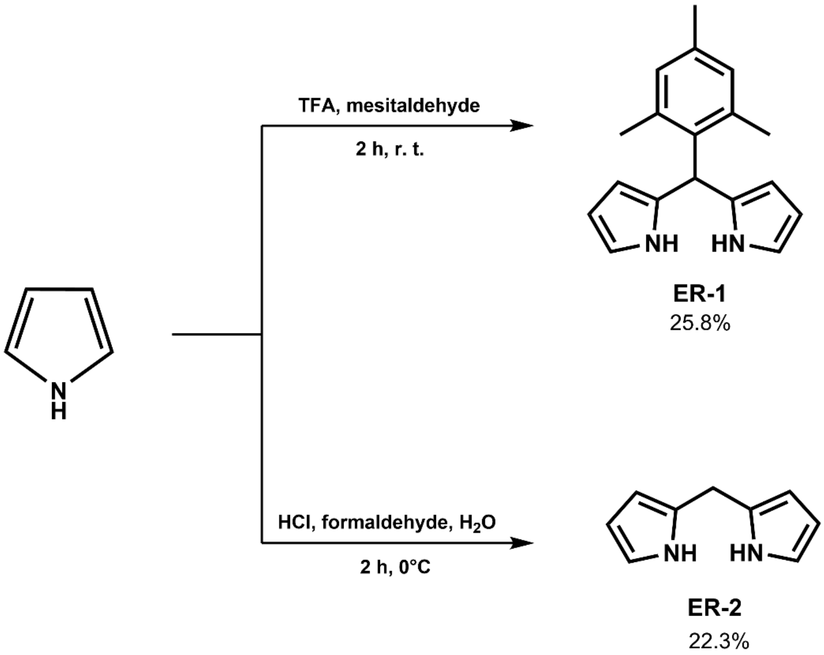

Figure 32. Synthesis of dipyrromethanes **ER-1** and **ER-2**.

The synthesis of dipyrromethane **ER-1** is performed in the presence of trifluoroacetic acid (TFA) and in the absence of solvent in order to limit any further oligomerisation of pyrrole beyond dipyrromethane.[182] Regarding the synthesis of the second dipyrromethane **ER-2** is synthesised using water. Formaldehyde is readily soluble in water, reducing the need for additional toxic solvents. **ER-1** and **ER-2** are obtained with yields of 25.8% and 22.3%, respectively. Although these yields are low, due to the polymerisation of pyrrole, they are consistent with those observed in the literature.[179, 183]

### *3.1.2 Synthesis of the porphyrin core*

We first set out to synthesise the porphyrin base, with the fourth meso-position being free for subsequent substitution/functionalisation. The remaining three meso-positions were initially aimed to bear a mesitylene group (**ER-3b**, Figure 33). Due to synthesis issues, the yield of the reaction was very poor even after optimisation and an abundance of unreacted aldehyde remained in the resulting crude product. Therefore, an alternative aldehyde, benzaldehyde, was used resulting in replacement of two of the meso-mesitylene groups with benzene of the porphyrin base (**ER-3**, Figure 34).

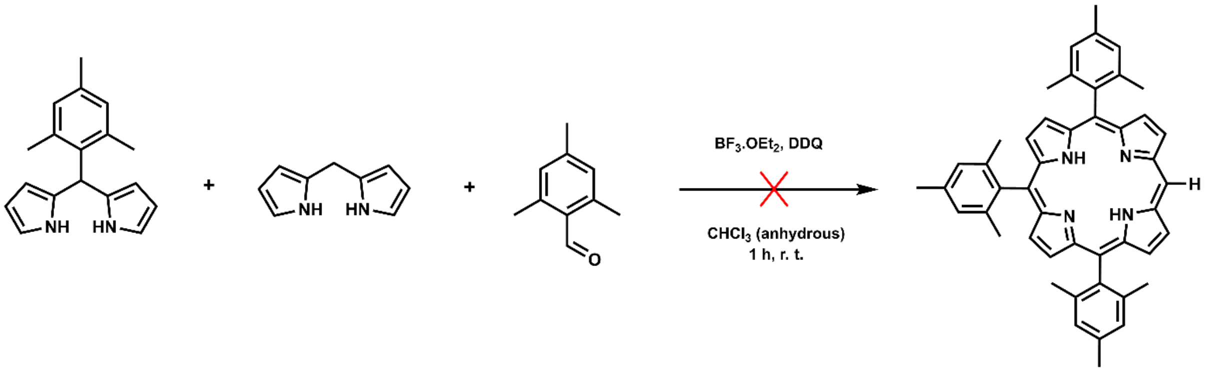

Figure 33. Unsuccessful porphyrin core (**ER-3b**) synthetic step.

The synthesis of porphyrin **ER-3** follows, as for **ER-3b**, the condensation method of Lindsey with the pyrrole being used directly. This method makes it possible to perform a condensation reaction between two dipyrromethanes (**ER-1** and **ER-2**) and an aldehyde (benzaldehyde in our case), in reasonable yields. The general synthetic scheme is shown in Figure 34.

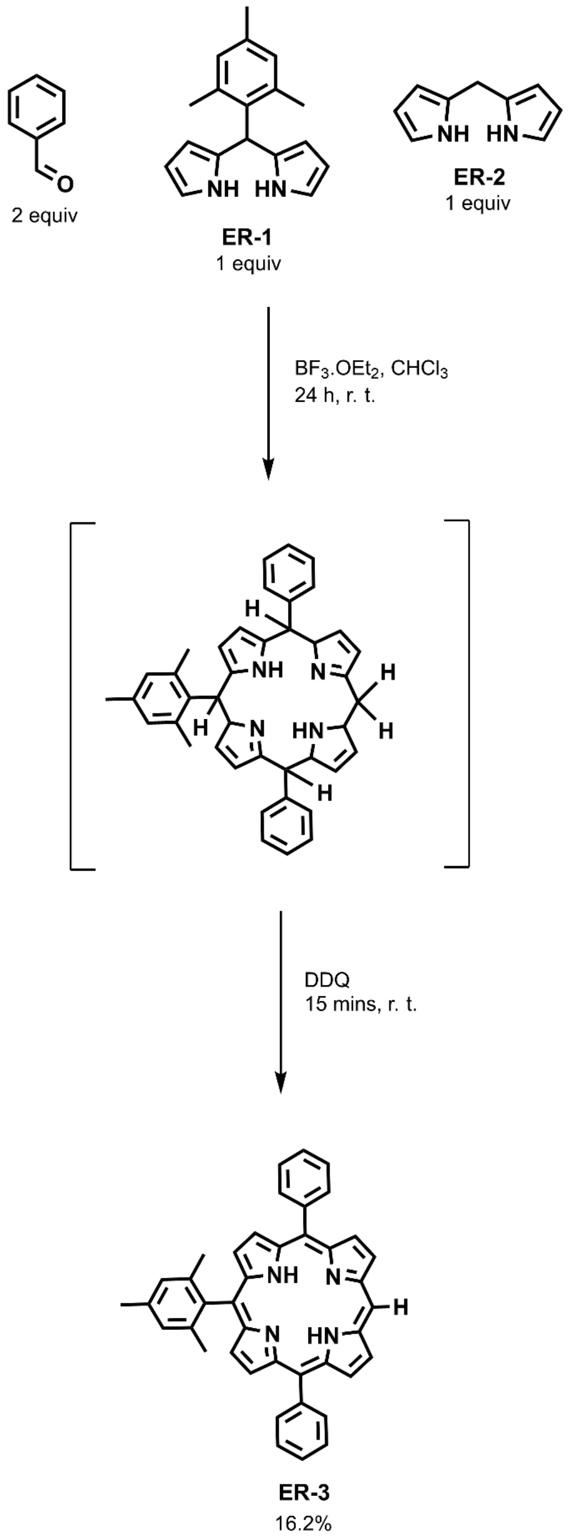

Figure 34. Principle of synthesis of 10-mesityl-5,15-diphenylporphyrin (**ER-3**).

The reaction between benzaldehyde, mesityl-dipyrromethane (**ER-1**), and dipyrromethane (**ER-2**) is performed in a dilute reaction medium according to the ratio 2/1/1. Catalysation with a Lewis acid (boron trifluoride diethyl etherate, $BF_3.OEt_2$) makes it possible to obtain the intermediate porphyrinogen, which is subsequently oxidised using 2,3-dichloro-5,6-dicyano-1,4-benzoquinone (DDQ). 10-mesityl-5,15-diphenylporphyrin (**ER-3**) is obtained after purification, with a yield of 16.2%. As previously, the yield is relatively low due to polymerisation of the dipyrromethanes (**ER-1** and **ER-2**) and formation of any side products. However, the yield remains consistent with those obtained in the literature.[184]

## 3.2 SYNTHESIS OF PORPHYRIN PRECURSORS: HALOGENATED AND ACETYLENIC

### *3.2.1 Iodination*

The iodination of the free meso-position of porphyrin **ER-3** was performed as previously described in the literature.[179, 185, 186] The reaction step consists of iodinating the free-base porphyrin in the presence of bis(trifluoroacetoxy)iodo benzene (PIFA) and iodide (Figure 35). The exact mechanism of iodination via PIFA/$I_2$ has not yet been fully realised. However, PIFA is known in literature for its use in radical reactions and nucleophilic substitutions as a catalytic reagent.[187] Iodo-mesityl-diphenylporphyrin (**ER-4**) is obtained after purification, with 55.6% yield.

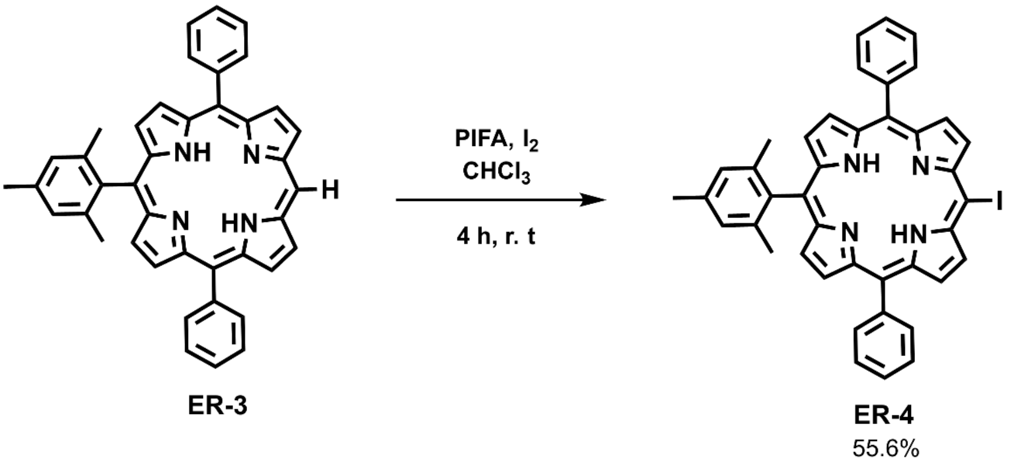

Figure 35. Iodination of the porphyrin core (**ER-3**) with PIFA.

*3.2.2 Acetylation via Sonogashira coupling*

During this reaction, the acetylene precursor, the trimethylsilylacetylene (TMSA), was attached to the meso-position of the iodinated porphyrin **ER-4** via Sonogashira coupling using bis(triphenylphosphine)palladium(II) dichloride ($PdCl_2(PPh_3)_2$ and copper(I) iodide (CuI) as catalyst system (Figure 36).[184] The reaction is carried out in an inert medium, in a Schlenk tube and using anhydrous toluene and triethylamine (TEA). The reaction is heated to 50 °C, and after stirring for 4 h the reaction is stopped. Purification of the crude compound leads to a yield of 23.3% of pure **ER-5**, the yield is relatively low, but this may be due to the reaction being performed on a small, mg scale. Another reason for the lower yield may be because complexation of copper by the free-base porphyrin has occurred. However, the $^1$H-NMR spectrum and mass spectrometry analysis confirms that **ER-5** was successfully synthesised, we still have free-base porphyrin as the NH-pyrrolic protons integration are normal.

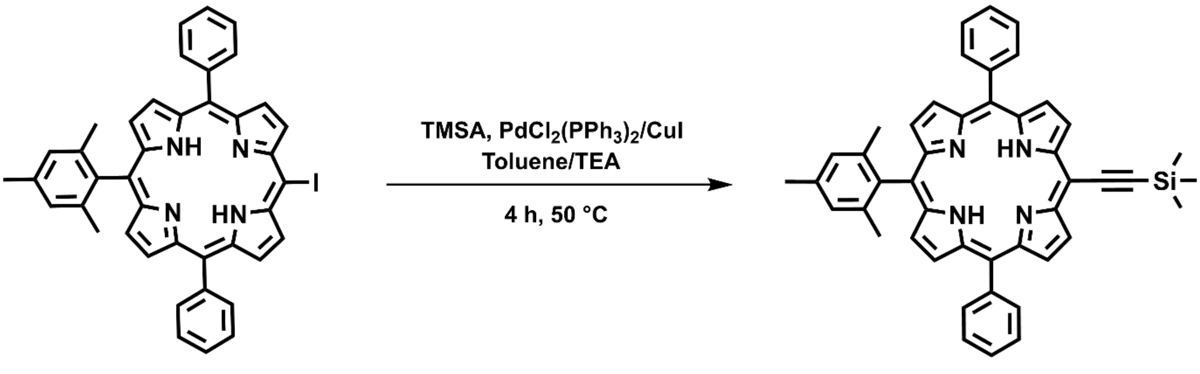

**ER-4**

**ER-5**
22.3%

Figure 36. Attachment of trimethylsilylacetylene (TMSA) to the halogen position of porphyrin **ER-4**.

## 3.3 NOVEL HETEROCYCLE (2-(4-BROMOPHENYL)-5-IODOPYRIMIDINE) SYNTHESIS

In order to further extend the π-conjugation system of our photosensitizer, we developed a route to synthesise a para-substituted pyrimidine heterocycle system (Figure 37). The additional terminal heteroatom (bromine, Br) may also provide added benefit of the heavy atom effect.

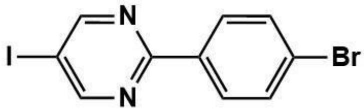

Figure 37. Structure of 2-(4-bromophenyl)-5-iodopyrimidine (**ER-6**)

*3.3.1 Synthesis of 2-(4-bromophenyl)-5-chloropyrimidine*

The initial chloropyrimidine was synthesised by the reaction of 5-chloro-2-iodopyrimidine and 4-bromophenylboronic acid in the presence of tetrakis(triphenylphosphine)palladium (0) ($Pd(PPh_3)_4$) catalyst, and heated to 55 °C (Figure 38) following the procedure by Hudson, *et al.*, as a guideline.[188] The reaction is performed in inert conditions, with anhydrous solvents, to avoid decomposition of the palladium catalyst. After 16 h the reaction is stopped and the crude is purified by silica gel column chromatography. **ER-6** was obtained in a 27.7% yield. This lower yield may be attributed to the high reactivity and reduced stability of the free boronic acid formed in the cross-coupling reaction. $^1$H-NMR and mass spectrometry confirm the structure of compound **ER-6**.

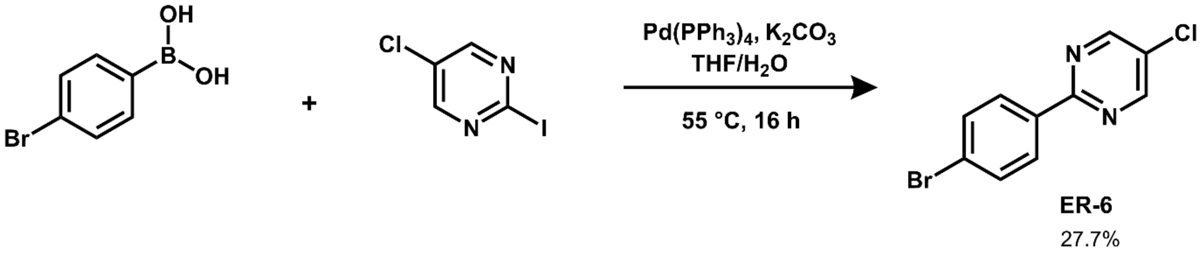

Figure 38. Cross-coupling reaction to form the para-substituted pyrimidine **ER-6**.

*3.3.2 Iodination of 2-(4-bromophenyl)-5-chloropyrimidine*

The next step is to perform an iodination reaction on **ER-6** in order to allow more straightforward coupling of the heterocycle with the porphyrin macrocycle. After optimisation of this step, the best procedure utilised the amine N, N-diethylethylenediamine (DEDA), and both CuI and NaI as catalyst and a source of iodide (Figure 39). After stirring for 48 h, at 100 °C, the reaction was stopped and the solvent evaporated to afford **ER-6-I** in 80% yield. Full conversion from **ER-6** to **ER-6-I** was achieved, with impurities removed during the washing stages.

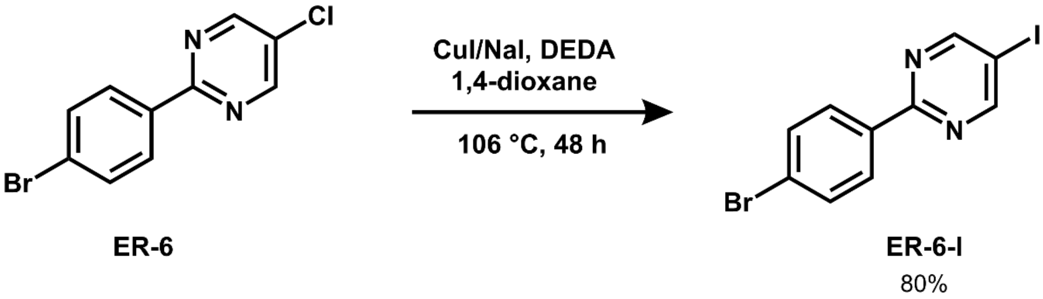

Figure 39. Iodination of pyrimidine **ER-6**.

## 3.4 COUPLING OF THE PORPHYRIN AND PYRIMIDINE HETEROCYCLE

### *3.4.1 Strategy*

The initial coupling route that we looked into implementing utilised triphenylarsine ($Ph_3As$), but we wanted to avoid the unnecessary use of the poisonous arsenic-containing compound. We set out to find an alternative route that would work for the coupling of our compounds. A couple of strategies based on Sonogashira coupling were found. The first one implemented didn't work (Figure 40), it was confirmed to not have worked by $^1$H-NMR and MS.

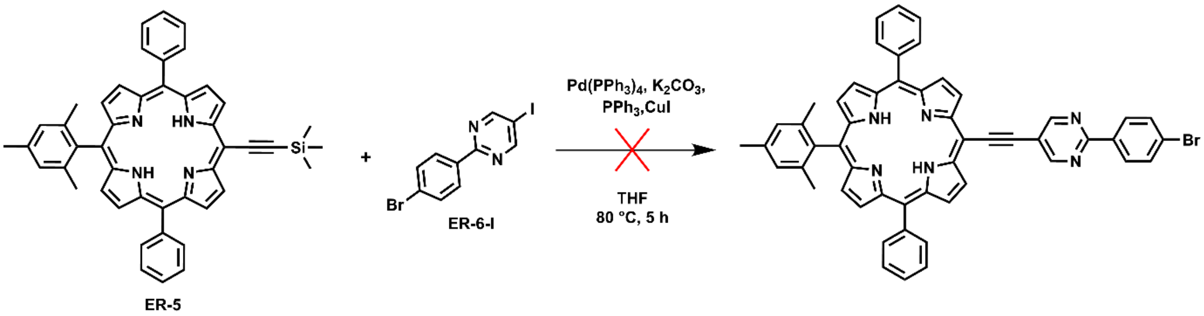

Figure 40. Unsuccessful strategy of the coupling of the acetylated porphyrin (**ER-5**) and the iodinated para-substituted pyrimidine (**ER-6-I**).

A mixture of **ER-6-I**, **ER-5**, $K_2CO_3$, $Pd(PPh_3)_4$, $PPh_3$, and CuI in a small amount of tetrahydrofuran (THF) was stirred at 80 °C. After stopping the reaction, and subsequent washing of the crude product, NMR and MS analysis confirmed that the coupling did not work. We increased the catalysts and ligands by 3-fold ($Pd(PPh_3)_4$, CuI, and $PPh_3$), but this still did not work. The next steps were to increase the reaction run-time and/or find an alternative ligand. The fact that the porphyrin is a free-base, non-metallated, may also be a factor in the reaction not working. The copper may be co-ordinated to the porphyrin rather than acting as a catalyst for the reaction. A different route to take this reaction in would be to use a metallated version of the porphyrin, either with zinc or palladium, to ensure the copper species partakes in the catalytic reaction to couple **ER-6-I** to the porphyrin **ER-5**.

Due to time constraints this step was unable to be optimised. However, there are still some routes that can be tested and hopefully, in the near future this can be completed with the resulting compound being characterised, and its usefulness within 2PA and possible PDT/PACT applications determined.

## 3.5 CHARACTERISATION

All compounds were characterised by $^1$H-NMR. The porphyrin macrocycles and pyrimidine heterocycles were further characterised by mass spectrometry, with the porphyrin macrocycles also being characterised by UV-Visible absorption spectroscopy. Z-scan technique, to measure the two-photon absorption properties, was also employed for the measurement of the porphyrin macrocycles.

### *3.5.1 $^1$H-NMR*

The proton-nuclear magnetic resonance spectra of all synthesised compounds were recorded at 500 MHz, with the exception of **ER-2** being recorded at 600 MHz (this was due to the 500 MHz being under repair at the time of measurement). All measurements were performed in deuterated chloroform, with the exception of **ER-5** being measured in deuterated dichloromethane, due to chloroform-d masking a proton signal.

The dipyrromethanes consist of several types of $^1$H-NMR signals:

- The NH-pyrrolic protons are very deshielded compared to those in the porphyrin derivatives, here they resonate between 7.84 and 7.93 ppm.
- The central protons in **ER-2** resonate at a higher ppm of 3.98 compared to similar aliphatic compounds due to being located next to 2 pyrrolic rings.
- The addition of the third aromatic ring in **ER-1** leads to the central proton signal being further deshielded and resonating at 5.93 ppm.

The spectrum of **ER-1** also differs from **ER-2** with the appearance of the -$CH_3$ signals (2.07 and 2.28 ppm).

As with the dipyrromethanes, the $^1$H-NMR spectrum of free meso-mesityl-diphenylporphyrin, and its derivatives ($A_3B$ type porphyrins) also consist of several types of signals:

- The NH-pyrrolic protons are very shielded and resonate between -2.40 and -2.89 ppm in the form of a singlet.
- The $CH_3$-mesityl protons are located between 1.82 and 2.63 ppm, and appear in the form of two singlets.
- Phenyl protons resonate between 6.01 and 8.24 ppm (And between 7.62 and 8.73 ppm for the para-substituted pyrimidines).
- The β-pyrrolic protons are located between 8.63 and 9.71 ppm, and appear in four different groups.
- The H-*meso*-proton is very deshielded and resonates around 10.00 ppm in the form of a singlet.
- Tetra-substituted porphyrins **ER-4** and **ER-5** are confirmed with the disappearance of the *meso*-proton signal, as seen in the **ER-3** spectrum (10.21 ppm).

- Attachment of TMSA in compound **ER-5** is confirmed with the appearance of three equivalent methyl groups in its spectrum (0.62 ppm).

The numbering of the carbons used in the interpretation of the $^1$H-NMR spectra is shown as an insert in the spectrum of each compound (Figure 41-47).

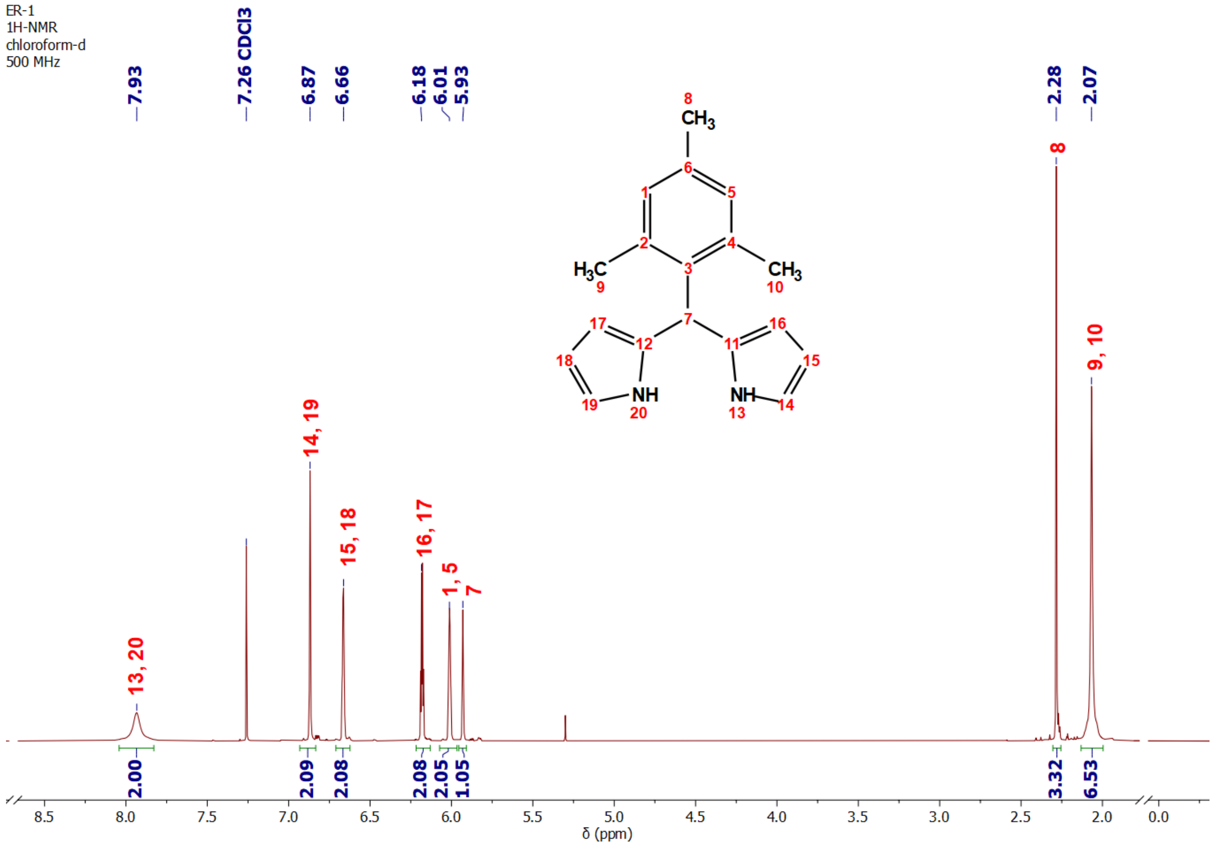

Figure 41. $^1$H-NMR spectrum of dipyrromethane **ER-1**.

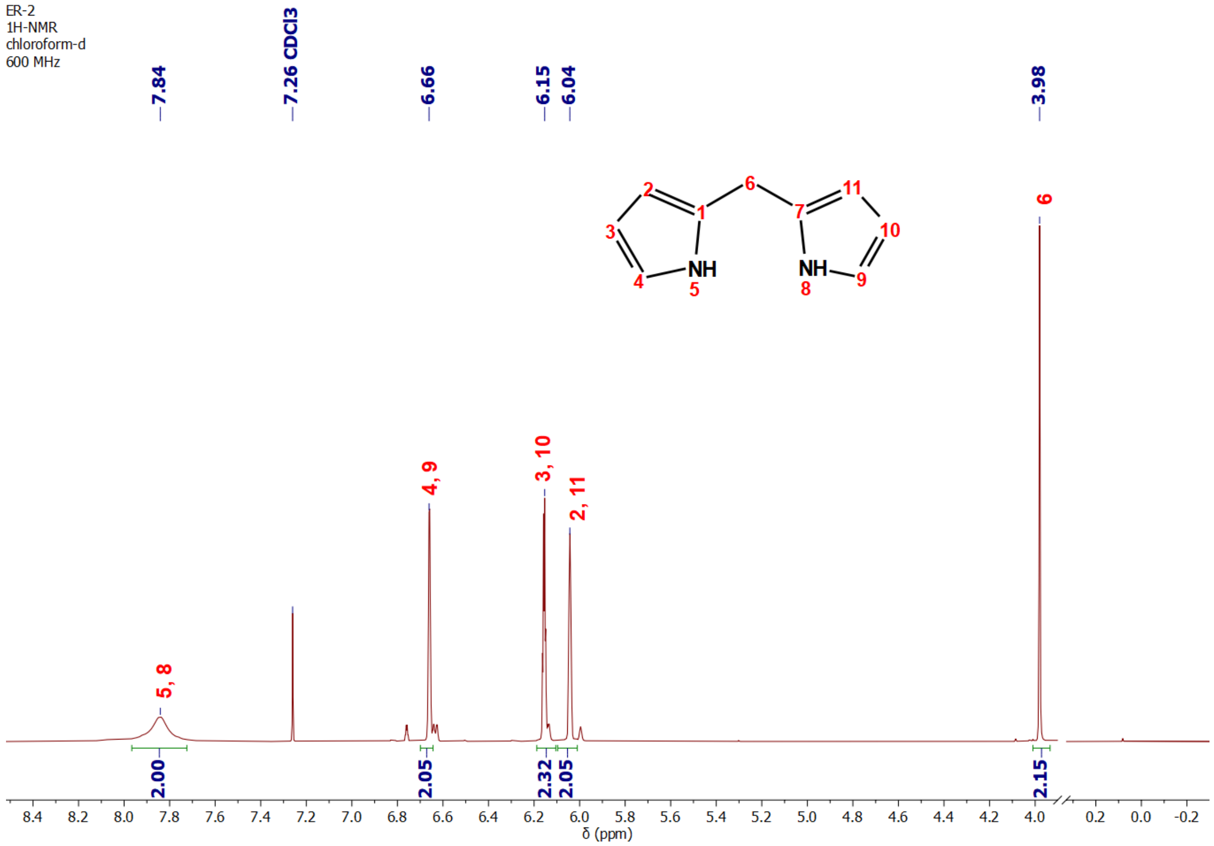

Figure 42. $^1$H-NMR spectrum of dipyrromethane **ER-2**.

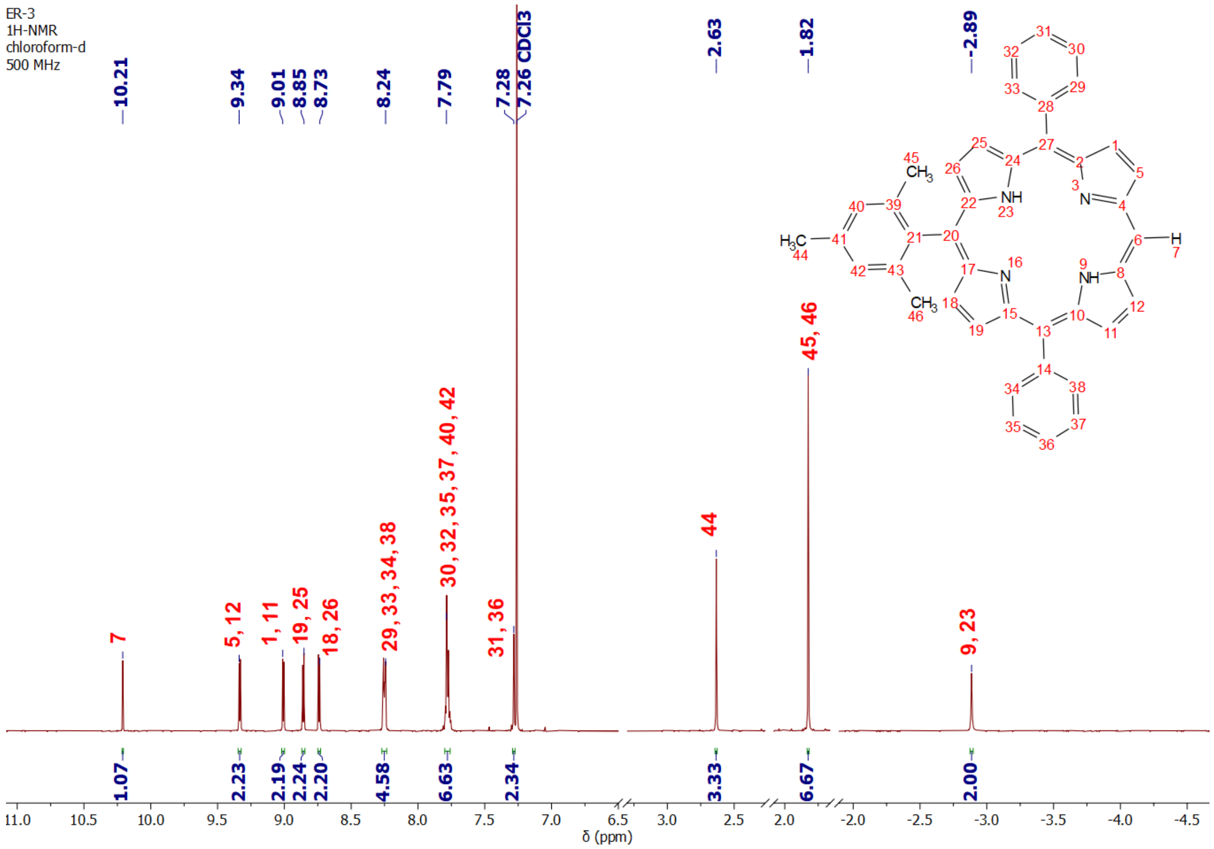

Figure 43. ¹H-NMR spectrum of free-base porphyrin **ER-3**.

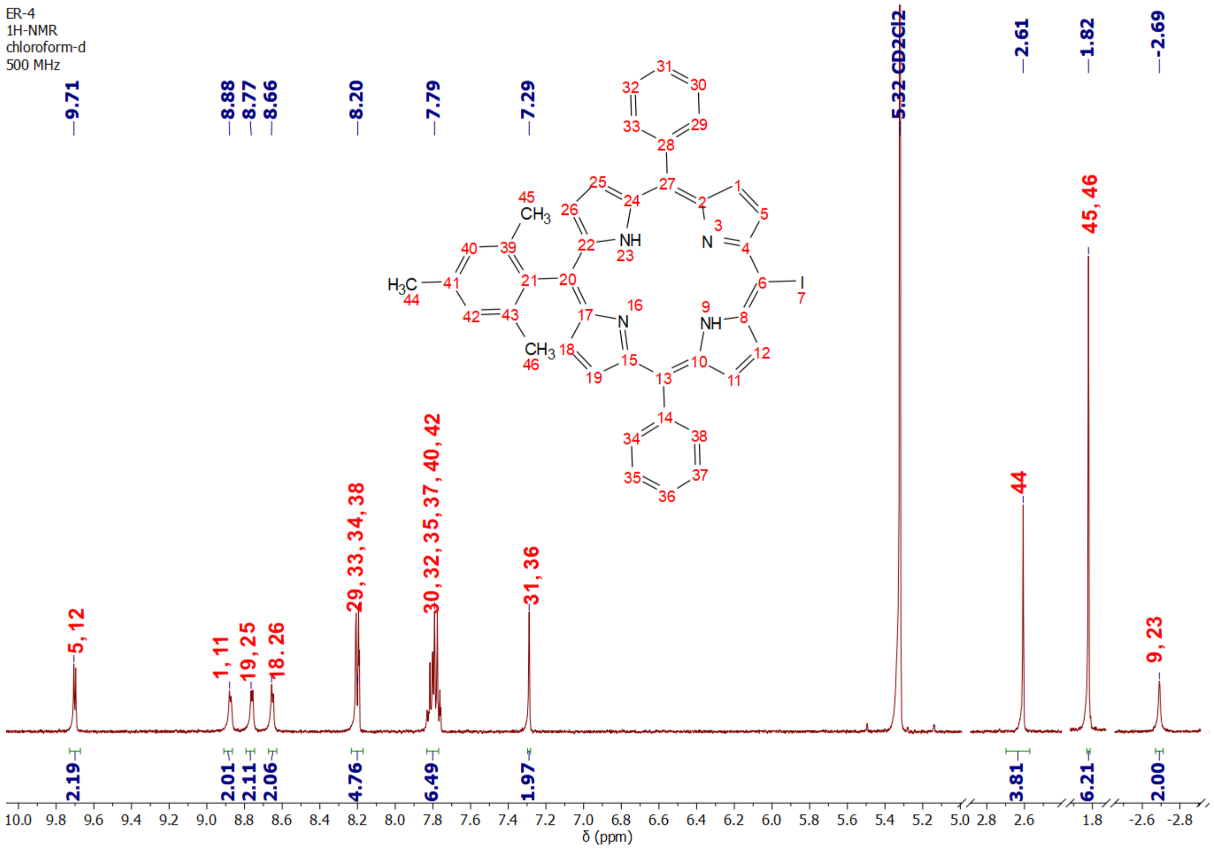

Figure 44. ¹H-NMR spectrum of halogenated free-base porphyrin **ER-4**.

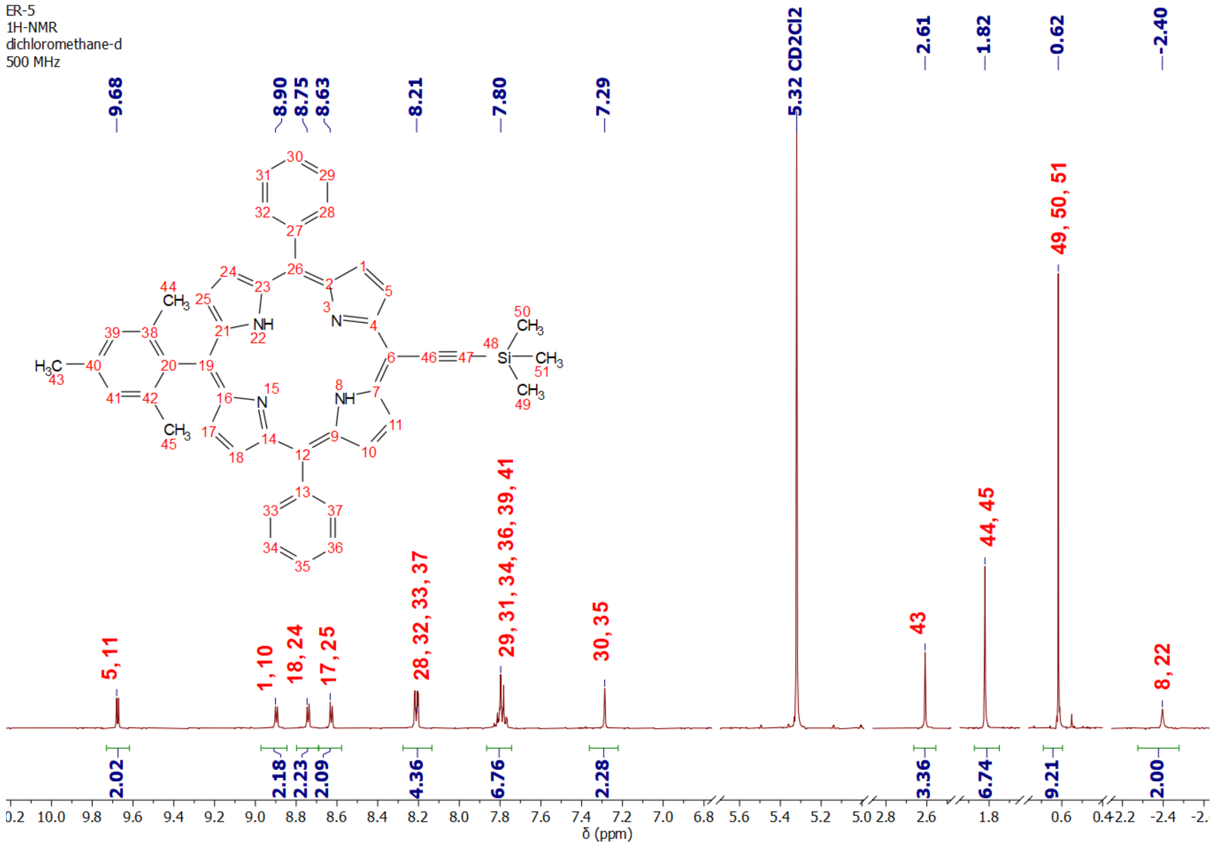

Figure 45. $^1$H-NMR spectrum of acetylated free-base porphyrin **ER-5**.

The para-substituted pyrimidines also display typical signals:

- Both spectra of **ER-6** and **ER-6-I** have three different signals as they both contain 6 protons.
- They only differ in the observed chemical shifts due to the difference in chlorine and iodine.
- The effect of the pyrimidine ring on the phenyl ring is different and the shifts are changed, 8.29 and 7.62 ppm for **ER-6**, and 8.13 and 7.84 ppm for **ER-6-I**.

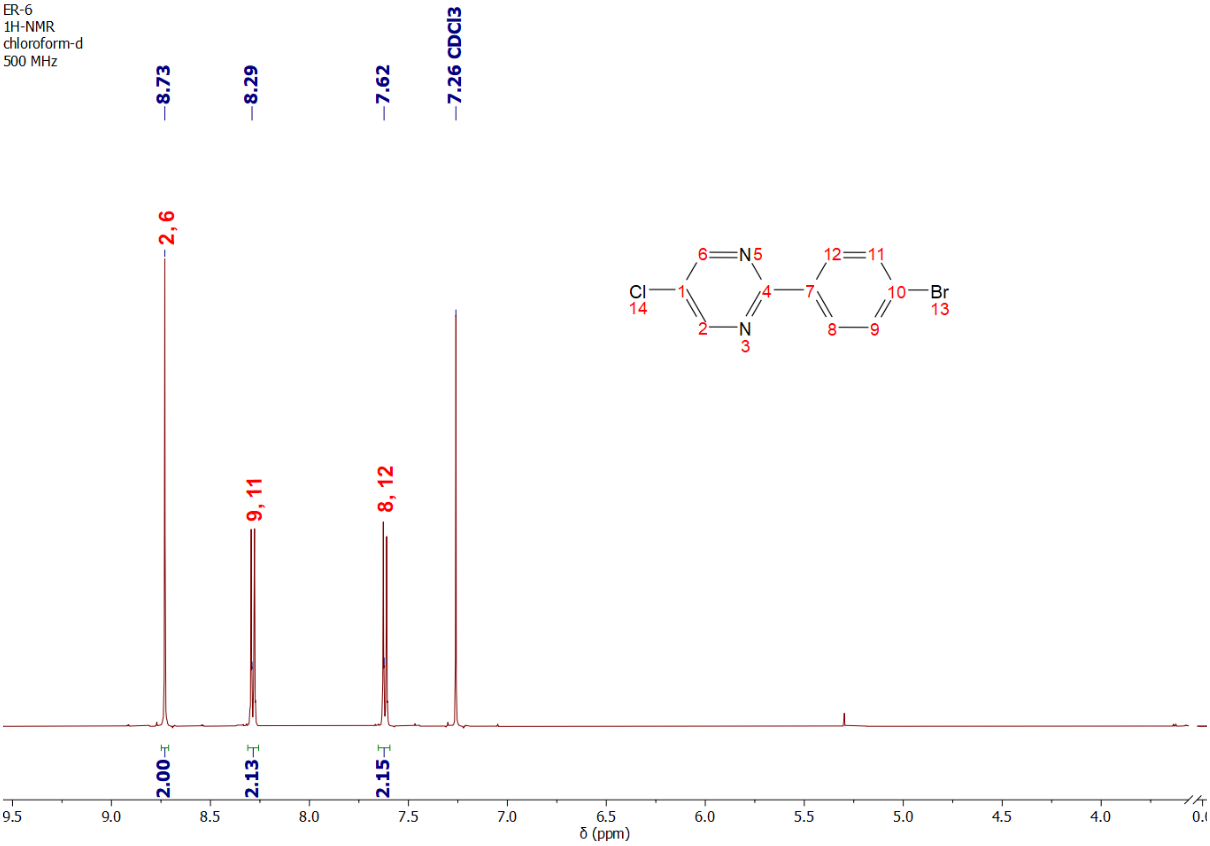

Figure 46. $^1$H-NMR spectrum of para-substituted pyrimidine **ER-6**.

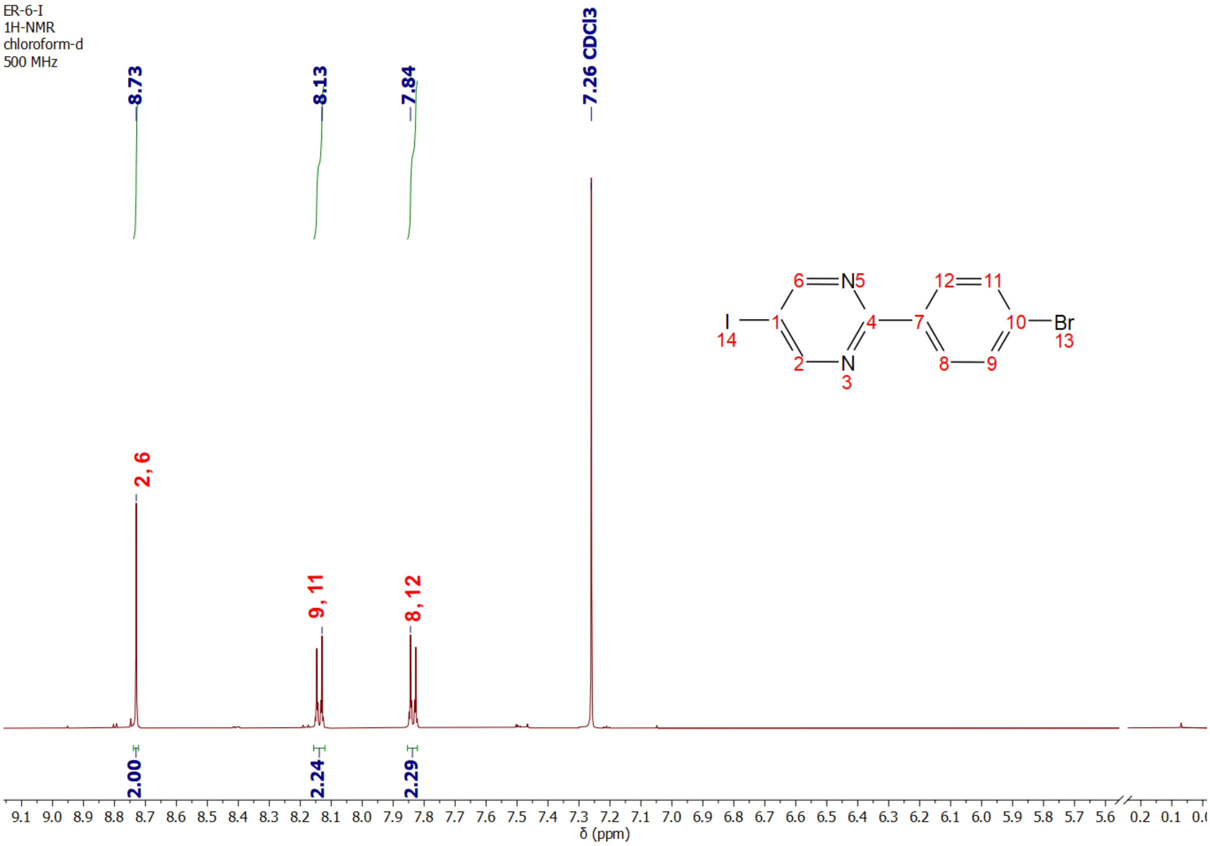

Figure 47. $^1$H-NMR spectrum of halogenated para-substituted pyrimidine **ER-6-I**.

### *3.5.2 Mass Spectrometry (MS)*

The structural analysis of compounds **ER-3**, **ER-4**, **ER-5**, **ER-7**, and **ER-7-I** was continued by studying their mass spectra. The matrix-assisted laser desorption-ionisation (MALDI) technique was utilised, it allows for the quasi-molecular ion to be observed, generally without fragmentation. The results obtained for the previously listed compounds are shown in Table 3. All the spectra show the quasi-molecular ion peak $[M + H]^+$. As an example, the spectra of compound **ER-3** and **ER-7** are shown in Figure 48 and 49.

Table 3. m/z value for the compounds **ER-3**, **ER-4**, **ER-5**, **ER-7**, and **ER-7-I** obtained by the MALDI-TOF method.

| **Compound** | **Chemical formula** | **Exact mass** | **Mass found $[M + H]^+$** |
|---|---|---|---|
| **ER-3** | $C_{41}H_{32}N_4$ | 580.263 | 581.308 |
| **ER-4** | $C_{41}H_{31}IN_4$ | 706.159 | 708.170 |
| **ER-5** | $C_{46}H_{40}N_4Si$ | 676.302 | 677.322 |
| **ER-7** | $C_{10}H_6BrClN_2$ | 267.940 | 270.764 |
| **ER-7-I** | $C_{10}H_6BrIN_2$ | 359.876 | 361.153 |

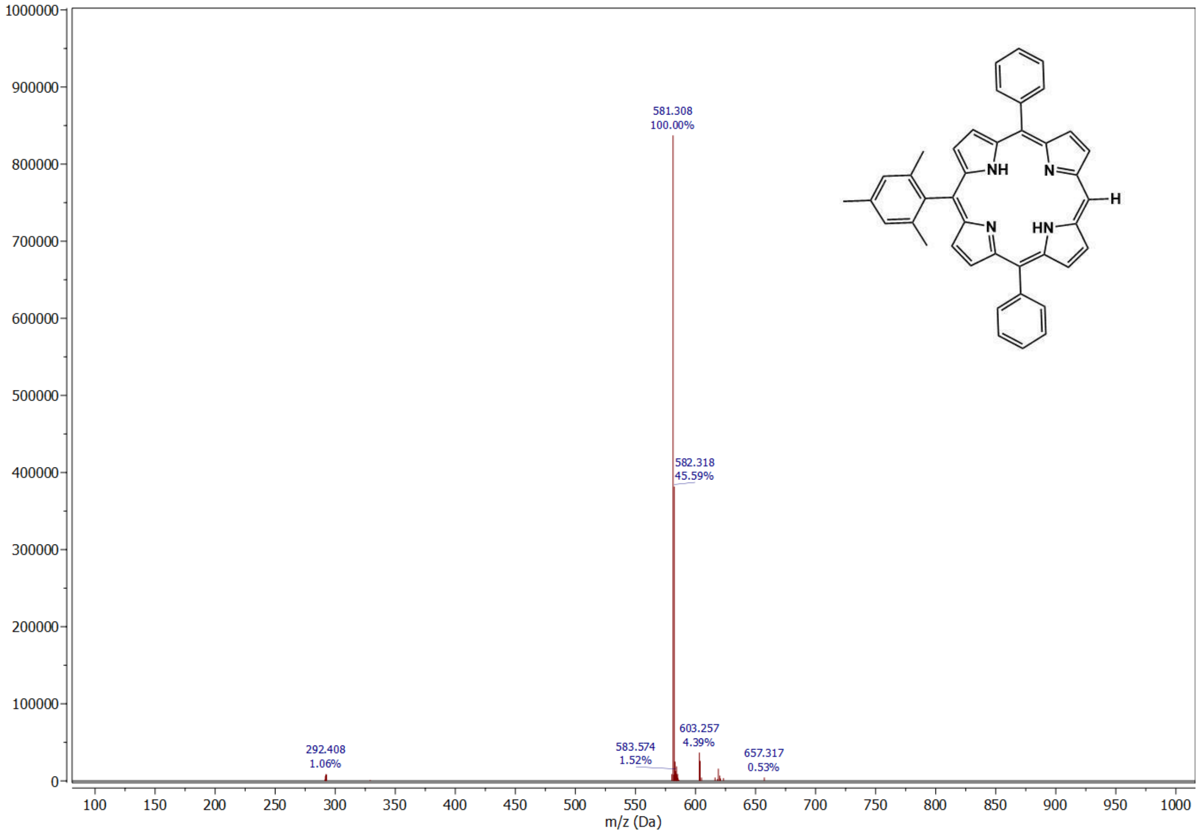

Figure 48. MALDI-TOF mass spectrum of compound **ER-3**.

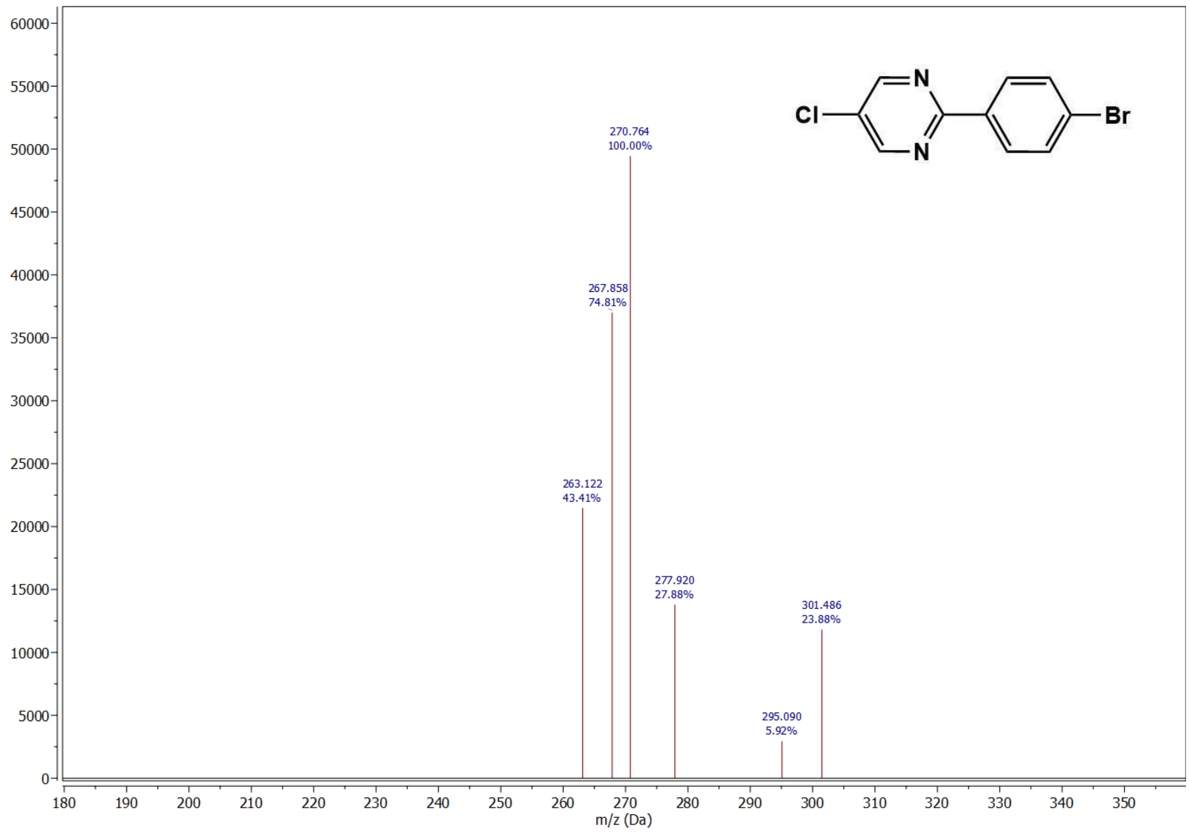

Figure 49. MALDI-TOF mass spectrum of compound **ER-6**.

### *3.5.3 UV-Visible absorption (UV-Vis)*

The spectra of **ER-3**, **ER-4**, and **ER-5** were measured in chloroform at room temperature (Figure 50-52). The concentrations used were in the order of $10^{-6}$ mol $dm^{-3}$. The spectra are combined and normalised in order to clearly visualise the displacement of the absorption bands (Figure 53).

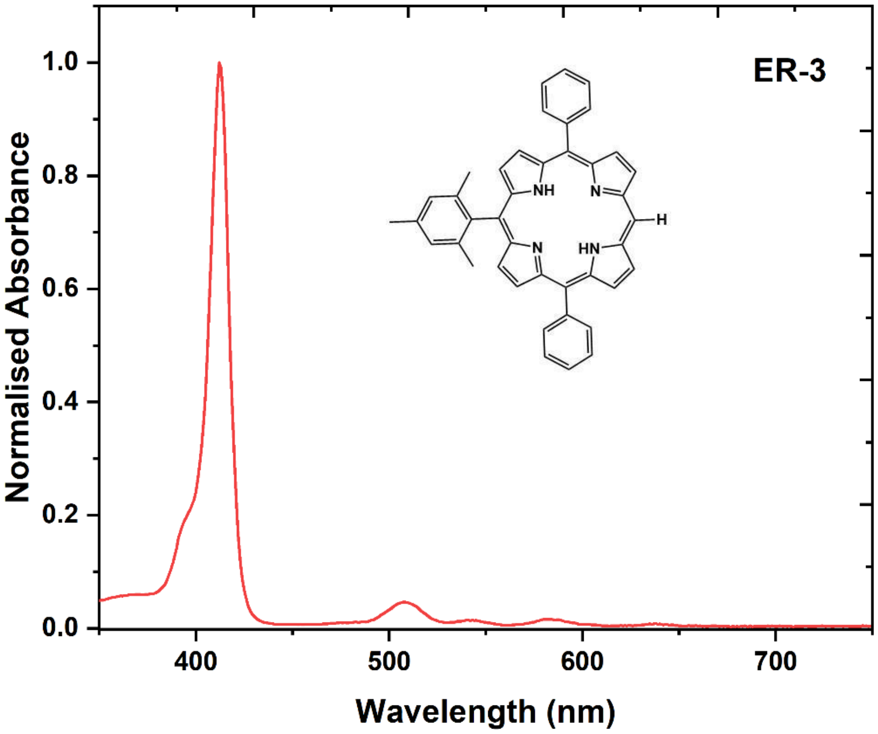

Figure 50. UV-Vis absorption spectrum of porphyrin **ER-3** in chloroform.

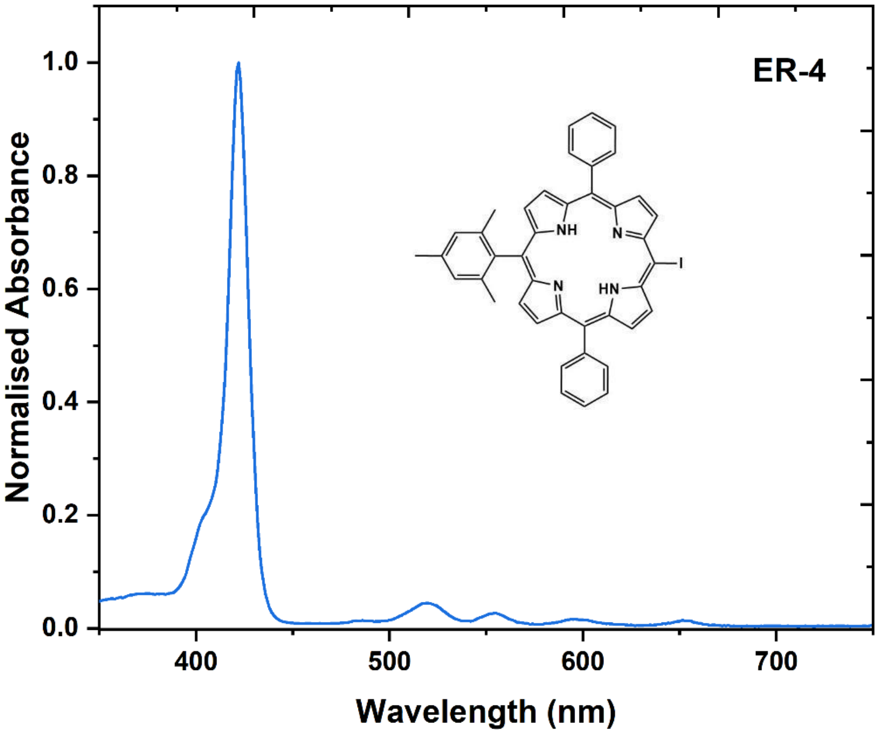

Figure 51. UV-Vis spectrum of porphyrin **ER-4** in chloroform.

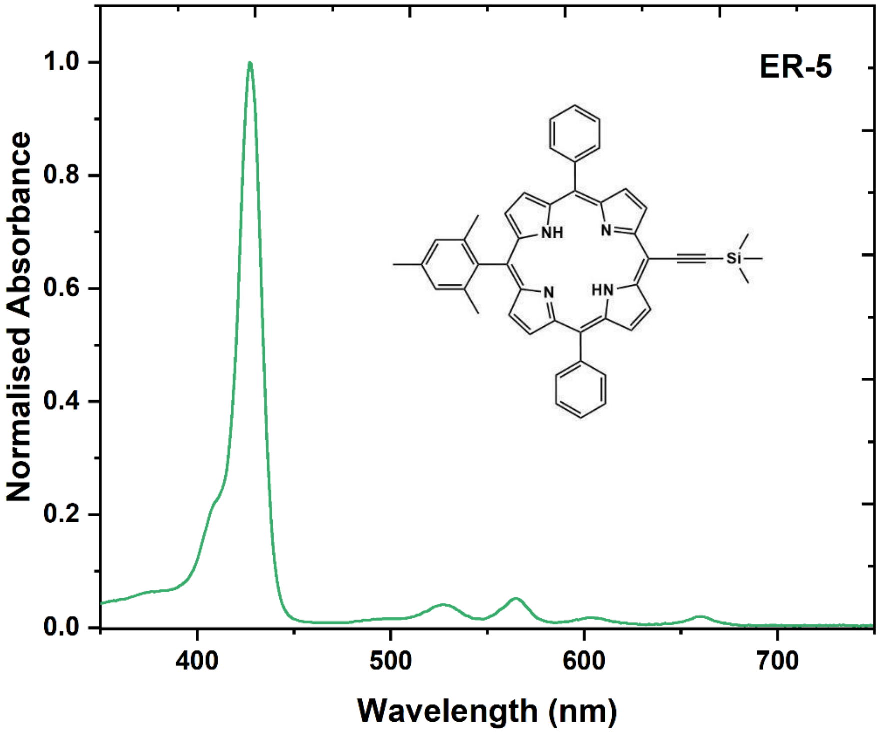

Figure 52. UV-Vis spectrum of porphyrin **ER-5** in chloroform.

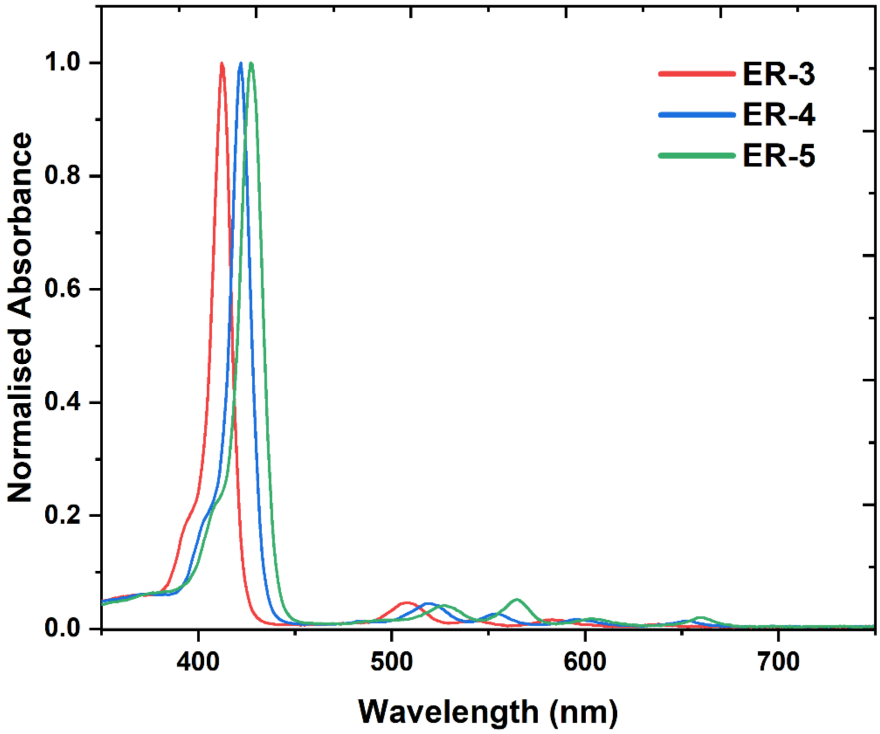

Figure 53. Combined and normalised UV-Vis spectra of porphyrins **ER-3**, **ER-4**, and **ER-5** in chloroform.

The three spectra are all characteristic of free-base porphyrin. There is strong absorption around 400 nm (Soret band) and four less intense bands between 500 and 700 nm (Q bands). The UV-Vis absorption characteristics ($\lambda_{max}$ and $\lambda_{Q\text{-band}}$) of each porphyrin derivative are listed in Table 4, below.

Table 4. UV-Vis absorption characteristics of porphyrins **ER-3**, **ER-4**, and **ER-5** all in chloroform.

| **Compound** | **$\lambda_{max}$ (nm)** | **$\lambda_{Q\text{-band}}$ (nm)** | **$\lambda_{Q\text{-band}}$ (nm)** | **$\lambda_{Q\text{-band}}$ (nm)** | **$\lambda_{Q\text{-band}}$ (nm)** |
|---|---|---|---|---|---|
| **ER-3** | 412 | 507 | 542 | 583 | 636 |
| **ER-4** | 422 | 519 | 554 | 596 | 652 |
| **ER-5** | 427 | 527 | 564 | 604 | 660 |

The red-shift observed of all absorption bands of the halogenated porphyrin **ER-4**, and acetylenic porphyrin **ER-5**, with respect to **ER-3**, is due to the reorganisation of the charges at the macrocycle level.[143, 144] The bathochromic effect can also be attributed to the mesomeric donor effect of the iodine in **ER-4**, or by extension of the conjugation in the case of **ER-5**.

Due to the increase in π-electrons of **ER-5**, and the possible reduction in aggregation and/or π-π stacking of the porphyrins in solutions of **ER-5** *vs*. **ER-4** and **ER-3** (due to **ER-5** being bulkier than its counterparts) there is an increase in the intensity of light absorbed and thus, we observe a hyperchromic shift in the spectrum of **ER-5**. Addition of more π-electrons may go on to further increase the hyperchromic shift, and this may have additional effects on the 2PA properties of the porphyrins.

### *3.5.4 Z-scan*

Herein we provide details of the 2PA properties of porphyrins **ER-3**, **ER-4**, and **ER-5**, characterised using the Z-scan technique. The Z-scan measurements were performed over a wide range of wavelengths (800 – 1360 nm), achieved by employing an Astrella Ti:Sapphire amplifier (output wavelength 800 nm) pumping a TOPAS Prime optical parametric amplifier equipped with a NirUVis frequency mixer, which delivered wavelength tunable pulses with a duration of about 50 fs and the repetition rate of 1 kHz. The output beam was selected with a polarization separator and attenuated using neutral density filters. Chloroform solutions of **ER-3**, **ER-4**, and **ER-5** were placed in stoppered 1 mm glass cuvettes. The concentration of each sample was 1% w/w. During a Z-scan measurement the sample moves along the axis of the incident beam, in the z-direction. Prior to and past the focal point, the so-called open- and closed-aperture signals are recorded. The open-aperture signal corresponds to the overall transmittance of the sample, and the closed-aperture signal corresponds to the transmittance of the central part of the beam as selected by an aperture in the far field. These signals, as well as the signal corresponding to the incident beam, were viewed on an oscilloscope, digitised, and transferred to a computer via a National Instruments BNC-2110 Terminal Block and National Instruments PCI-6143 Multifunction I/O Device. The obtained results for the three porphyrins were calibrated by using Z-scan measurements performed on a fused silica plate. The non-linear refractive index of the fused silica plate was assumed from literature data, and subsequently compared with measurements of an identical glass cuvette filled only with the solvent (chloroform). The obtained data were analysed using a custom fitting program that utilises equations derived by Sheik-Bahae, *et al.*[152]

Changes to the substituent in the "free" meso-position lead to changes in the electron delocalisability, and charge transfer of each porphyrin, due to the nature of and differences between each substituent -H, -I, and -≡-$SiMe_3$. In the case of porphyrin **ER-4** bearing a halogen (I), the intersystem crossing (ISC) may be enhanced via the heavy atom effect, and leads to the red-shift observed in the UV-Vis spectra.

The 2PA cross-sections ($\sigma_2$) of porphyrins **ER-3**, **ER-4**, and **ER-5** have been measured and compared by using the femtosecond open-aperture Z-scan technique. The 2PA has been measured at excitation wavelengths corresponding to double the wavelength region of the one-photon absorption (1PA) bands (those measured by UV-Vis absorption). The measured wavelengths are between 800 and 1360 nm. The computed $\sigma_2$ values are presented in Figure 54 overlaying their respective 1PA spectrum, below.

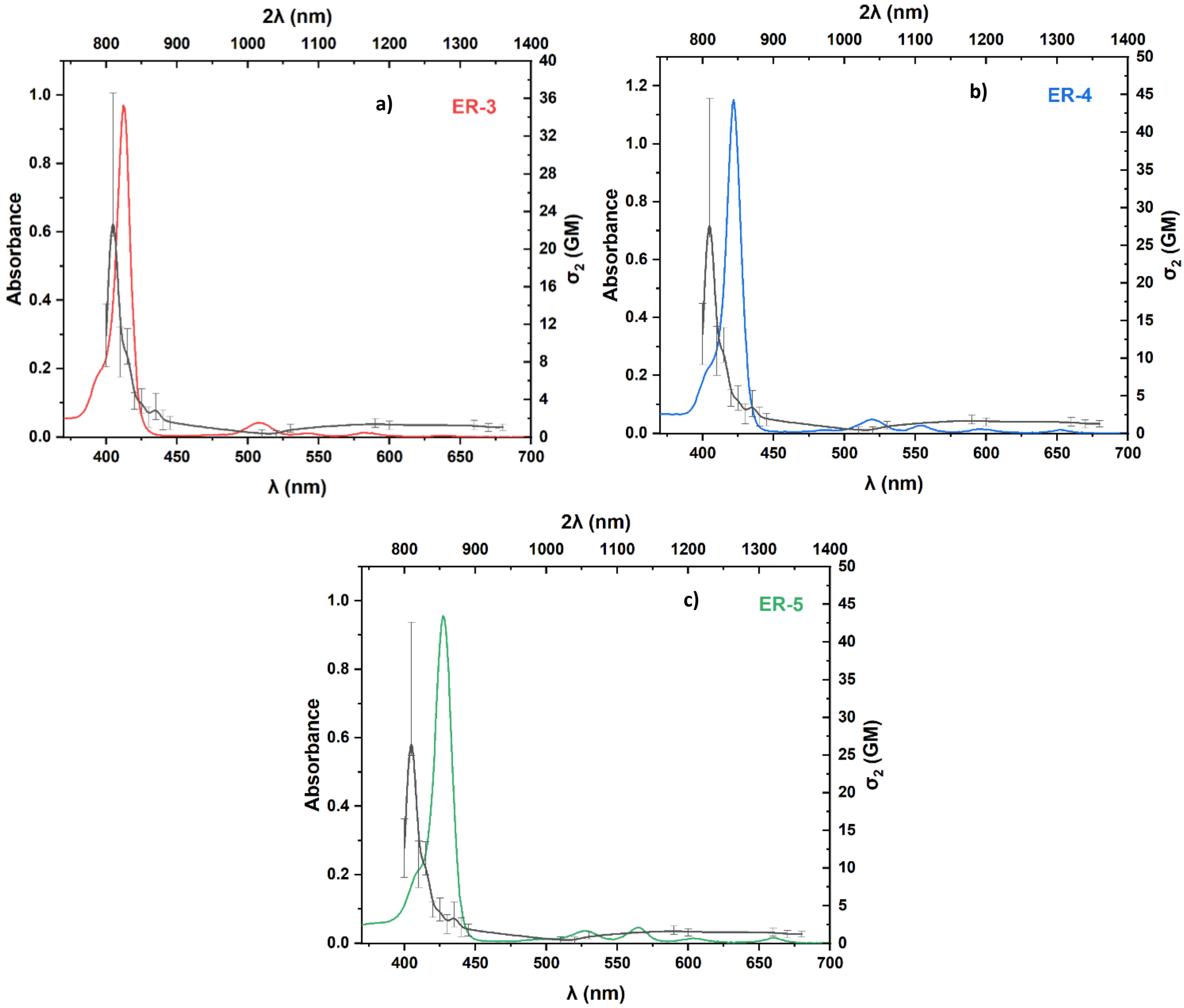

Figure 54. Overlay of 1PA (solid colour lines) and 2PA (solid black lines) spectra for **ER-3** (a, red), **ER-4** (b, blue), and **ER-5** (c, green) in chloroform. $\sigma_2$ are derived from the Z-scan measurements and plotted against twice the wavelength (2λ) of the 1PA spectra.

This presentation of spectra (2PA overlaying the 1PA spectra) relies on the assumption that the same excitable states can be reached by both 1PA and 2PA, which is a common occurrence for non-centrosymmetric molecules.[40] The calculated $\sigma_2$ values of all measured wavelengths, for each porphyrin, are listed in Table 5, below.

Table 5. The calculated 2PA cross-section values ($\sigma_2$) of porphyrins **ER-3**, **ER-4**, and **ER-5** performed in $CHCl_3$.

| | **ER-3** | | **ER-4** | | **ER-5** | |
|---|---|---|---|---|---|---|
| **Wavelength (nm)** | **$\sigma_2$ (GM)** | **Error** | **$\sigma_2$ (GM)** | **Error** | **$\sigma_2$ (GM)** | **Error** |
| 800 | 10.8351 | ± 3.3509 | 13.1859 | ± 4.078 | 12.6284 | ± 3.9055 |
| **810** | **28.9813** | ± 7.5878 | **35.2691** | ± 9.2341 | **33.7779** | ± 8.8436 |
| 820 | 9.019 | ± 2.655 | 10.9758 | ± 3.2311 | 10.5117 | ± 3.0945 |
| 830 | 9.6587 | ± 1.8962 | 11.7543 | ± 2.3076 | 11.2573 | ± 2.2101 |
| 840 | 3.8675 | ± 0.88909 | 4.7066 | ± 1.082 | 4.5076 | ± 1.0362 |
| 850 | 3.8716 | ± 1.3037 | 4.7117 | ± 1.5866 | 4.5124 | ± 1.5195 |
| 860 | 2.1746 | ± 1.0946 | 2.6464 | ± 1.332 | 2.5345 | ± 1.2757 |
| 870 | 3.2699 | ± 1.3998 | 3.9794 | ± 1.7035 | 3.8111 | ± 1.6315 |
| 880 | 1.8431 | ± 1.0629 | 2.243 | ± 1.2936 | 2.1482 | ± 1.2389 |
| 890 | 1.5183 | ± 0.67517 | 1.8478 | ± 0.82165 | 1.7696 | ± 0.78691 |
| 1000 | --- | --- | --- | --- | --- | --- |
| 1020 | 0.3304 | ± 0.42662 | 0.40208 | ± 0.51918 | 0.38508 | ± 0.49723 |
| 1040 | 0.35619 | ± 0.35973 | 0.43347 | ± 0.43778 | 0.41514 | ± 0.41927 |
| 1060 | 0.92512 | ± 0.41278 | 1.1258 | ± 0.50234 | 1.0782 | ± 0.4811 |
| 1080 | --- | --- | --- | --- | --- | --- |
| 1100 | --- | --- | --- | --- | --- | --- |
| 1120 | --- | --- | --- | --- | --- | --- |
| 1140 | --- | --- | --- | --- | --- | --- |
| 1160 | --- | --- | --- | --- | --- | --- |
| 1180 | 1.5091 | ± 0.4812 | 1.8366 | ± 0.58561 | 1.7589 | ± 0.56085 |
| 1200 | 1.2646 | ± 0.4275 | 1.539 | ± 0.52025 | 1.4739 | ± 0.49825 |
| 1220 | --- | --- | --- | --- | --- | --- |
| 1240 | --- | --- | --- | --- | --- | --- |
| 1260 | --- | --- | --- | --- | --- | --- |
| 1280 | --- | --- | --- | --- | --- | --- |
| 1300 | --- | --- | --- | --- | --- | --- |
| 1320 | 1.2983 | ± 0.48413 | 1.58 | ± 0.58917 | 1.5132 | ± 0.56426 |
| 1340 | 1.0384 | ± 0.43306 | 1.2637 | ± 0.52702 | 1.2102 | ± 0.50474 |
| 1360 | 1.0668 | ± 0.34552 | 1.2983 | ± 0.42048 | 1.2434 | ± 0.40271 |

It is evident that porphyrin **ER-3**, with the *meso*-H substituent, displays smaller $\sigma_2$ and thus, weaker non-linear absorption compared to **ER-4** and **ER-5**. This is indicated at the maximum $\sigma_2$ value (@ 810 nm) of each porphyrin being 28.98 ± 7.59 GM, 32.27 ± 9.23 GM, and 33.78 ± 8.84 GM for **ER-3**, **ER-4**, and **ER-5**, respectively. The larger cross-sections of **ER-4** and **ER-5** are due to the heavy atom effect and increased conjugation of the macrocycles, respectively. The calculated data shows that each of the three compounds display a relatively weak 2PA maximum around 1360 nm.

Further photophysical studies of each compound would be helpful in proving the extent of the heavy atom effect and extended π-conjugation mechanisms. Such studies may shed more light on these effects that are of great interest for novel materials related to PDT/PACT applications, 2PA imaging, and more.

## 3.6 EXPERIMENTAL - SYNTHESIS

Note: where it is stated that anhydrous solvent is used, the "wet" solvent was passed through a column of alumina immediately prior to use to remove excess water (unless stated otherwise).[189, 190]

### *3.6.1* ***ER-1*** *(mesityl-dipyrromethane)*

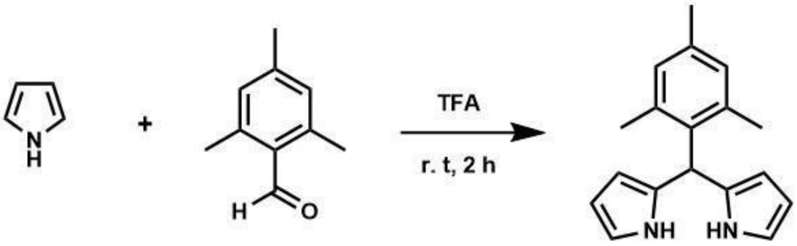

40 equiv of pyrrole (40 mL; 577 mmol) and 1 equiv of mesitaldehyde (2 mL; 13.6 mmol) are stirred under Ar at room temperature for 15 min then 0.2 equiv of TFA (210 µL; 2.7 mmol) are added to the mixture. The reaction continues for 2 hours until the majority of the mesitaldehyde has reacted. The reaction is stopped by adding 100 mL of dichloromethane (DCM) and 20 mL of 0.1 M aqueous NaOH. The organic phase is washed with $H_2O$ (3 x 150 mL), dried over $MgSO_4$ and then evaporated. The crude is purified on a silica gel column (eluent: Hexane / DCM: 2/1) and after recrystallization from cyclohexane, **ER-1** is obtained in the form of a white powder (yield = 25.8%).

TLC: $R_f$ = 0.6 (Hexane/DCM: 2/1)

$^1$H-NMR: *CDCl₃* (500 MHz) – 7.93 (2H, $H_{NH}$, s), 6.87 (2H, $H_{mesityl}$, s), 6.66 (2H, $H_{pyrrole}$, m), 6.18 (2H, $H_{pyrrole}$, q (*J* = 2.8 Hz)), 6.01 (2H, $H_{pyrrole}$, m), 5.93 (1H, $H_{meso}$, s), 2.28 (3H, $H_{methyl}$, s), 2.07 (6H, $H_{methyl}$, s)

### *3.6.2* ***ER-2*** *(di(1H-pyrrol-2-yl)methane)*

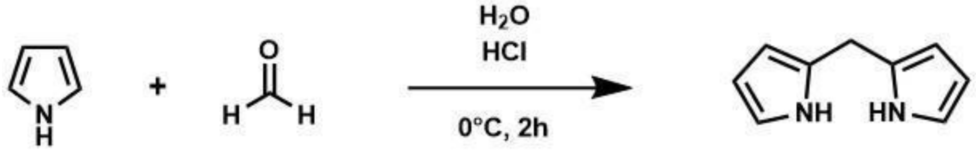

Pyrrole (17 mL, 245 mmol, 1.5 equiv) was dissolved in water (60 mL) and the solution was degassed with nitrogen for 30 min and then cooled down to 0 °C. Formaldehyde (4.5 mL, 37% in water, 163 mmol, 1 equiv) and HCl (0.2 mL, 35%, 2 mmol, 0.03 equiv) were added dropwise over a period of 15 min and the reaction was stirred for a further 2 h at 0 °C. The reaction solution was extracted three times with DCM (3 x 50 mL) and the combined organic layers were concentrated under reduced pressure. The crude product was purified by column chromatography (eluent = Hexane/DCM: 2/1) to yield di(1H-pyrrol-2-yl)methane **ER-2** as a white solid (yield = 22.3%). **ER-2** was stored in the freezer since it is prone to slight decomposition at room temperature.

TLC: $R_f$ = 0.25 (Hexane/DCM: 1/1)

$^1$H-NMR: *CDCl₃* (600 MHz) – 7.84 (2H, $H_{NH}$, s), 6.66 (2H, $H_{pyrrole}$, m), 6.15 (2H, $H_{pyrrole}$, q (*J* = 2.9 Hz), 6.04 (2H, $H_{pyrrole}$, m), 3.98 (2H, $H_{meso}$, s)

### *3.6.3 **ER-3** (10-mesityl-5,15-diphenylporphyrin)*

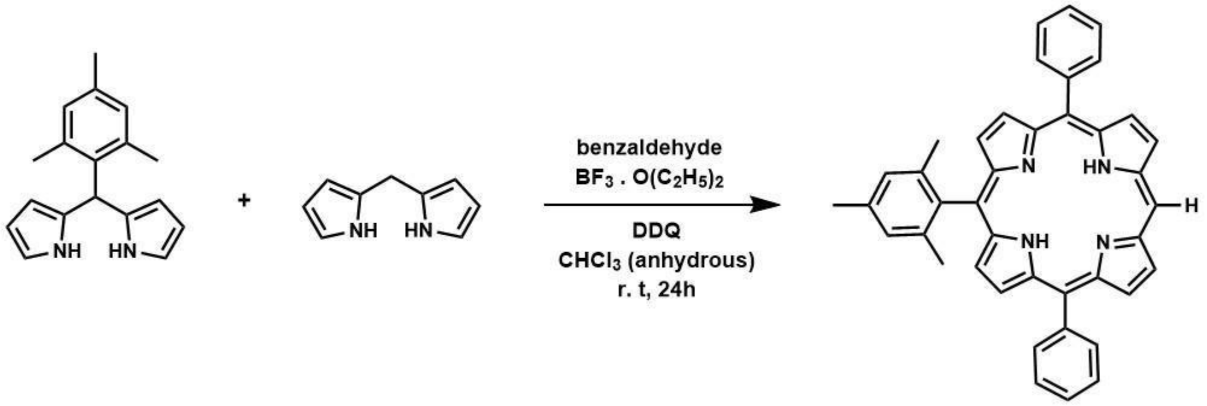

300.4 mg of **ER-1** (1.13 mmol, 1 equiv), 165.8 mg of **ER-2** (1 equiv, 1.13 mmol) and 0.34 mL of benzaldehyde (3.35 mmol, 2 equiv) are added to a round bottom flask. Then, 150 mL of anhydrous chloroform is added to the flask followed by 18 µL of boron trifluoride diethyl etherate (0.146 mmol, 0.13 equiv). The mixture is left to stir for 24 h, under argon. After 24 h, 779 mg of DDQ (3.43 mmol, 3.3 equiv) is added to the reaction flask and left to stir for 15 minutes. TEA (3 mL) is added to quench the reaction, and the mixture then poured onto a silica gel column (eluent = DCM) to remove the tar from the mixture. The resulting porphyrin mixture is separated via flash column chromatography (eluent gradient starting with Hexane/DCM: 10/1 to 10/1.1). **ER-3** is obtained as a purple solid (yield = 16.2%).

TLC: $R_f$ = 0.64 (Hexane/DCM: 1/1)

$^1$H-NMR: *CDCl₃* (500 MHz) – 10.21 (1H, $H_{meso}$, s), 9.34 (2H, $H_{\beta pyrrolic}$, d (*J* = 4.6 Hz)), 9.01 (2H, $H_{\beta pyrrolic}$, d (*J* = 6.5, 4.6 Hz)), 8.85 (2H, $H_{\beta pyrrolic}$, d (*J* = 4.8 Hz)), 8.73 (2H, $H_{\beta pyrrolic}$, d (*J* = 4.8 Hz)), 8.24 (4H, $H_{2,6\ phenyl,}$ m), 7.79 (6H, $H_{3,4,5\ phenyl,}$ m), 7.28 (2H, $H_{mesityl}$, s), 2.63 (3H, $H_{methyl}$, s), 1.82 (6H, $H_{methyl}$, s), -2.89 (2H, $H_{NH}$, s)

### *3.6.3.1 **ER-3b** (5, 10, 15-trimesityporphyrin)*

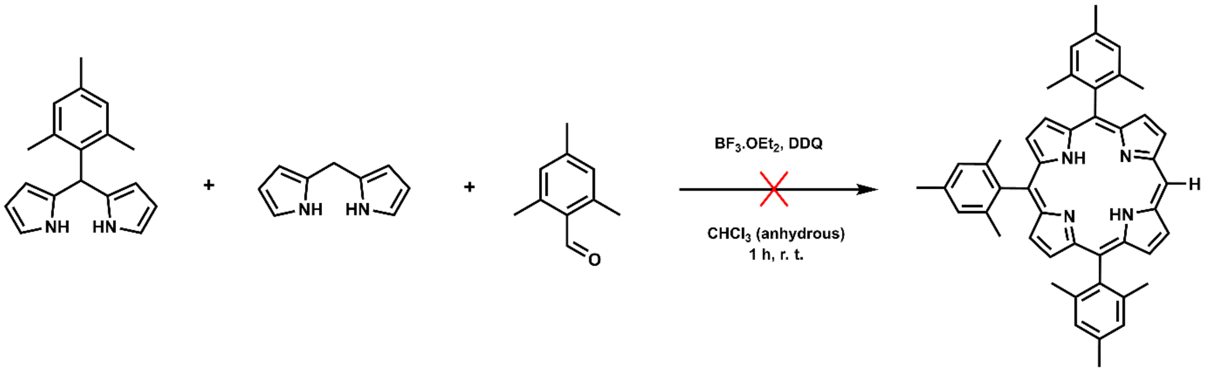

300 mg of **ER-1** (1.135 mmol, 1 equiv), 165.9 mg of **ER-2** (1.135 mmol, 1 equiv) and 0.34 mL of mesitaldehyde (2.27 mmol, 2 equiv) are dissolved in 150 mL of anhydrous $CHCl_3$. The reaction medium is stirred at room temperature for 10 minutes and then 84.04 µL of trifluoroborane diethyl etherate (0.681 mmol, 0.6 equiv) are added to the mixture dropwise. After 1 h of stirring, 772.94 mg of DDQ (3.405 mmol, 3 equiv) are added and the reaction continues for an additional 1 h. The reaction is stopped by evaporation of the solvent. The crude is pre-purified (eluent: $CH_2Cl_2$) in order to remove the tar. **ER-3** is obtained after purification by silica-gel column chromatography (eluent $CH_2Cl_2$ / Petroleum ether: 3/7) in the form of a purple solid. It was found that even after purification there still remained unreacted mesitaldehyde that could not be separated from the porphyrin product. Upon repetition, reaction run time was extended to 24 hours (before addition of DDQ). $^1$H-NMR analysis displayed unreacted aldehyde still remained in the resulting crude mixture, separation proved difficult with porphyrin yields too low for the next steps of the synthesis. Reaction for **ER-3** (section 3.6.3) was solely used from this point onwards.

### 3.6.4 ***ER-4*** *(5-iodo-15-mesityl-10,20-diphenylporphyrin)*

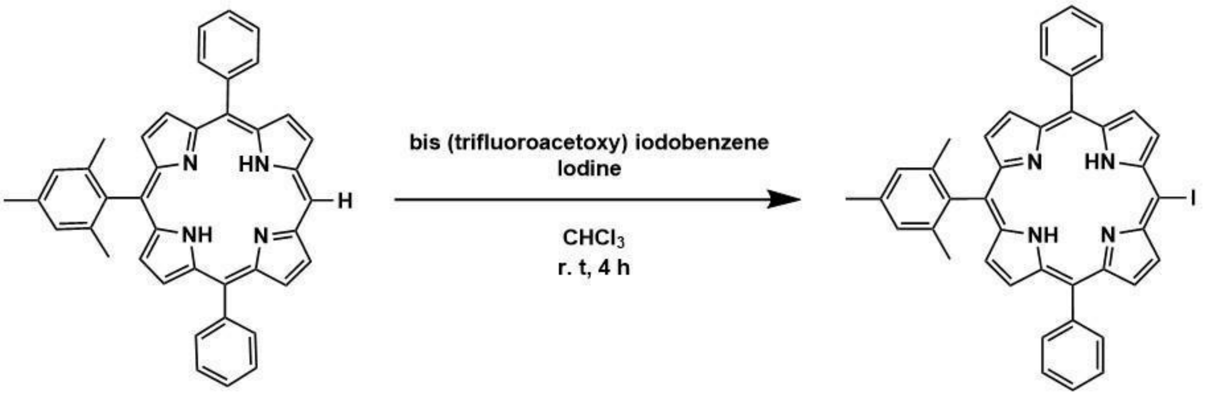

1 equiv of 10,15,20-trimesitylporphyrin (**ER-3**) (69.2 mg; 0.119 mmol), 0.75 equiv of bis (trifluoroacetoxy) iodobenzene (39.8 mg; 0.0925 mmol) and 0.6 equiv of iodine (19.4 mg; 0.0764 mmol) are dissolved in 8 mL of $CHCl_3$. After stirring for 4 h at room temperature, the reaction medium is diluted by adding DCM (70 mL). The organic phase is neutralised with saturated sodium thiosulfate ($Na_2S_2O_3$) solution (2 x 70 mL), washed with $H_2O$ (2 x 100mL), dried over $MgSO_4$ and then evaporated. The product obtained is purified on a silica gel column (eluent = Pet. ether/DCM gradient starting from 9/1 to 7/3) to obtain **ER-4** in the form of a purple solid (yield = 55.6%).

TLC: $R_f$ = 0.5 (Pet. ether/DCM: 2/1)

$^1$H-NMR: *$CD_2Cl_2$* (500 MHz) – 9.69 (2H, $H_{\beta pyrrolic}$, d (*J* = 4.8 Hz)), 8.87 (2H, $H_{\beta pyrrolic}$, d (*J* = 4.0 Hz)), 8.76 (2H, $H_{\beta pyrrolic}$, d (*J* = 4.6 Hz)), 8.65 (2H, $H_{\beta pyrrolic}$, d (*J* = 4.6 Hz)), 8.2 (4H, $H_{2,6\ phenyl}$, m), 7.79 (6H, $H_{3,4,5\ phenyl}$, m), 7.28 (2H, $H_{mesityl}$, s), 2.60 (3H, $H_{methyl}$, s), 1.82 (6H, $H_{methyl}$, s), -2.68 (2H, $H_{NH}$, s)

### *3.6.5* ***ER-5*** *(5-mesityl-10,20-diphenyl-15-((trimethylsilyl)ethynyl)porphyrin)*

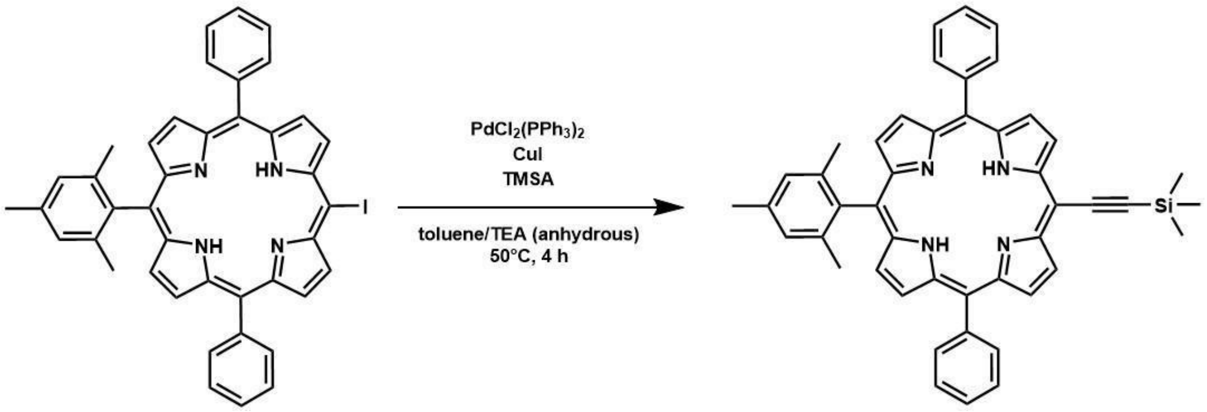

**ER-4** (1 eq, 30 mg, 0.0425 mmol), $PdCl_2(PPh_3)_2$ (0.2 eq, 10.9 mg, 0.0155 mmol), CuI (0.1 eq, 1.7 mg, 0.00893 mmol) and TMSA (5 equiv, 54 µL, 0.390 mmol) were combined in a Schlenk flask. Dry toluene and dry TEA (3.3 mL, 3/0.3) were added and the solution was freeze-pump-thaw degassed (x6). Then, the mixture was stirred for 4 h at 50 °C. After evaporation of the solvent, the crude product was dissolved in DCM (25 mL), washed twice with $H_2O$ (2 x 50mL) and dried over $MgSO_4$. The residue was purified by silica gel column chromatography (hexane/DCM: gradient ranging from 1/0.1 to 1/0.5). **ER-5** was obtained as a dark purple solid (yield = 23.3%).

TLC: $R_f$ = 0.48 (Hexane/DCM: 2/1)

$^1$H-NMR: *$CD_2Cl_2$* (500 MHz) – 9.67 (2H, $H_{\beta pyrrolic}$ d (*J* = 4.8 Hz)), 8.90 (2H, $H_{\beta pyrrolic}$ d (*J* = 4.6 Hz)), 8.75 (2H, $H_{\beta pyrrolic}$ d (*J* = 4.8 Hz)), 8.63 (2H, $H_{\beta pyrrolic}$ d (*J* = 4.8 Hz)), 8.22 (4H, $H_{2,6\ phenyl,}$ m), 7.79 (6H, $H_{3,4,5\ phenyl,}$ m), 7.29 (2H, $H_{mesityl}$, s), 2.61 (3H, $H_{methyl}$, s), 1.82 (6H, $H_{methyl}$, s), 0.62 (9H, $H_{SiCH3,}$ s), -2.40 (2H, $H_{NH}$, s)

### *3.6.6 **ER-6** (2-(4-bromophenyl)-5-chloropyrimidine)*

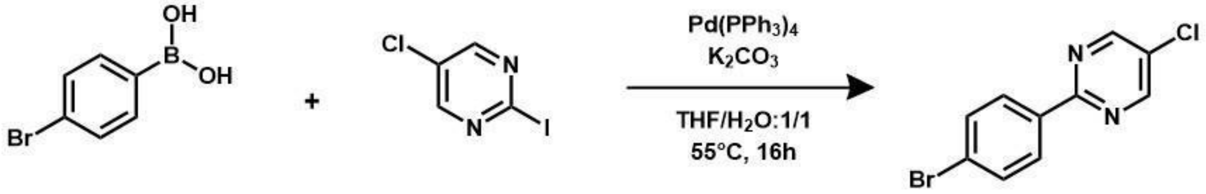

To a Schlenk flask with condenser and stirrer bar, 4-bromophenylboronic acid (421.8 mg, 1 equiv, 2.1 mmol), 5-chloro-2-iodopyrimidine (502.6 mg, 1 equiv, 2.09 mmol), Pd $(PPh_3)_4$ (71.7 mg, 0.03 equiv, 0.062 mmol) $K_2CO_3$ (862.3 mg, 3 equiv, 6.24 mmol), and 30 mL degassed 1:1 THF/$H_2O$ were added. The mixture was heated to 55 ° C with stirring for 20 h, the THF is then removed under reduced pressure, and the aqueous layer extracted with DCM (4 x 30 mL). The combined organic layers were dried with $MgSO_4$, concentrated, and the residue purified by column chromatography on silica (eluent = Hexane/DCM gradient from 1/0.2 to 1/0.3) to give **ER-6** as a white solid (yield = 27.7%).

TLC: $R_f$ = 0.45 (Hexane/DCM: 2/1)

$^1$H-NMR: *CDCl$_3$* (500 MHz) – 8.73 (2H, $H_{2,6}$, s), 8.29 (2H, $H_{8,12}$, d (*J* = 4.6 Hz)), 7.62 (2H, $H_{9,11}$, d (*J* = 4.8 Hz))

### *3.6.7* ***ER-6-I*** *(2-(4-bromophenyl)-5-iodopyrimidine)*

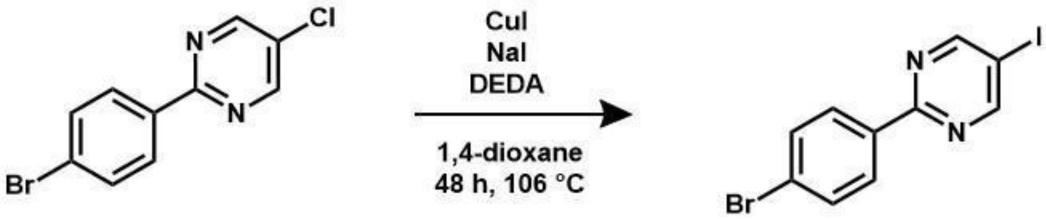

30 mg of **ER-6** (0.11 mmol, 1 equiv), 114.27 mg of CuI (0.6 mmol, 6 equiv), 89.93 mg of NaI (0.6 mmol, 6 equiv), 84.30 µL of N, N-diethylethylenediamine (DEDA) (0.6 mmol, 6 equiv), and anhydrous 1, 4-dioxane (15 mL) were added to a small, dry flask with a stirrer bar. The reaction mixture was heated to reflux (106 °C) and left to stir for 48 h, under nitrogen, until all of the starting material is completely converted. Afterwards, the reaction was quenched with saturated $NH_4Cl$ solution (30 mL), extracted with DCM (3 x 25 mL), and dried over anhydrous $Na_2SO_4$. The solvent is then removed under reduced pressure to afford compound **ER-6-I** (yield = 80%).

TLC: $R_f$ = 0.44 (Hexane/DCM: 2/1)

$^1$H-NMR: *CDCl₃* (500 MHz)– 8.73 (2H, $H_{2,6}$, s), 8.13 (2H, $H_{8,12}$, d (*J* = 4.8 Hz)), 7.84 (2H, $H_{9,11}$, d (*J* = 4.8 Hz))

### *3.6.8 **ER-7** (5-((2-(4-bromophenyl)pyrimidin-5-yl)ethynyl)-15-mesityl-10,20-diphenylporphyrin)*

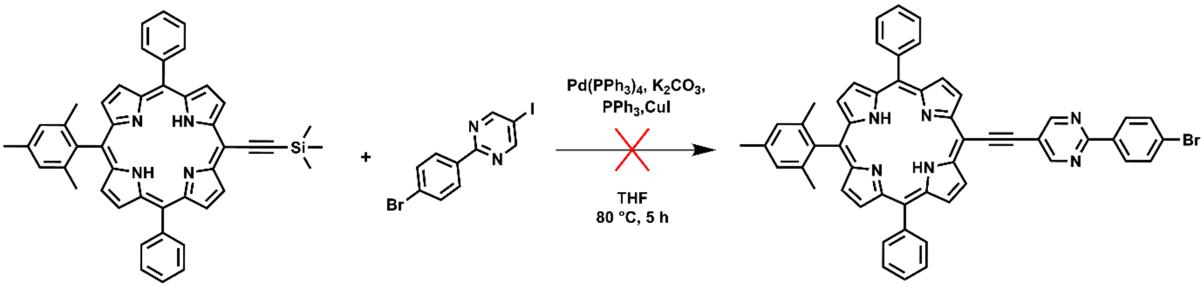

A mixture of **ER-6-I** (15.99 mg, 1 equiv, 0.0443 mmol), **ER-5** (30 mg, 1 equiv, 0.0443 mmol), $K_2CO_3$ (12.24 mg, 2 equiv, 0.0886 mmol), $Pd(PPh_3)_4$ (1.54 mg, 0.03 equiv, 0.00133 mmol), $PPh_3$ (0.35 mg, 0.03 equiv, 0.00133 mmol), and CuI (0.3 mg, 0.03 equiv, 0.00133 mmol) in 5 mL of THF was stirred at 80 °C. After stirring for 5 h, to the mixture was added 10 mL aqueous 2 M HCl, and extracted with 3 x 15 mL ethyl acetate. The organic phase was sequentially washed with 10 mL of brine, 10 mL of aqueous sat. $NaHCO_3$, an additional 10 mL of brine, and dried with $MgSO_4$. After removal of the solvent under reduced pressure, the $^1$H-NMR and MS were analysed and it was confirmed that the product **ER-7** was not formed. Alterations were made to the catalytic equivalences (increased 3-fold to 0.09 equiv for $Pd(PPh_3)_4$, $PPh_3$, and CuI) and the reaction repeated without success. The procedure requires further alterations.

# Chapter IV:

## Two-photon absorption properties of expanded macrocycles: naphthiporphyrins

# INTRODUCTION

Another method for the enhancement of porphyrin properties is via expansion of the macrocycle core. There are various studies on this topic, with few pertaining to the enhancement of 2PA properties. Carbaporphyrinoids expand upon the porphyrin core and are such characterised by their presence of carbon atom(s) within the macrocycle's coordination cavity.[191] This expanded macrocycle leads to porphyrin analogues with unusual coordination environments, composed of nitrogen donors and carbon atoms, these analogues remain capable of metal or metalloid binding.[192]

Carbaporphyrinoids[193] can be composed of embedding polycyclic aromatic hydrocarbon (PAH) subunits, to replace a pyrrole unit, such as benzene,[91] azulene,[194] cycloheptatriene,[195] and naphthalene,[92] to name a few. Aceneporphyrinoids or naphthiporphyrins, those containing the naphthalene subunit, have been found to be of particular interest due to the naphthalene motif playing a crucial role in determining the overall properties of the expanded macrocycle.[196-198] The nature of the PAH moiety present determines the extent of which the electronic properties of the macrocycle are altered, and whether this also partakes in the π-delocalisation of the molecule. Aceneporphyrinoids have received much attention in recent years for several reasons, including their atypical π-conjugation,[199, 200] their varying aromaticity from anti-aromatic and non-aromatic,[201, 202] as well as their ability to form stable organometallic complexes with metals with uncommon oxidation states.[203-205] Upon incorporation of a PAH, the cavity size of the macrocycle may exceed 16 atoms, which is typical for a regular sized porphyrin/porphyrinoid.[96, 206] These resulting macrocycles are considered expanded carbaporphyrinoids.

The type of PAH embedded porphyrinoid that we explore here are naphthiporphyrins. To date, a series of constitutional isomers of naphthiporphyrin have been synthesised. These include 1,3-,[92, 207] 1,4-,[92, 208] 1,5-,[209] and 1,7-naphthiporphyrinoids.[197] These macrocycle possess a precisely designed cavity within which there is contribution of porphyrin-like donor atoms, these compounds are becoming more and more attractive for their use within organometallic and organoelement chemistry.[192, 210] Naphthiporphyrins also possess atypical conformational flexibility.[211-213]

The molecular properties of these expanded macrocycles can by further modified via the inclusion of heteroatoms,[97, 214, 215] such as oxygen, sulfur, selenium, or tellurium, within the cavity of the macrocycle. Inclusion of heteroatoms has a significant effect on the electronic properties of the molecules. This in turn has an effect on the spectral, structural, and coordination properties of the molecule.[196, 198, 216]

The study here is based on a new constitutional isomer of naphthiporphyrin that was designed and synthesised in a previous study, 28-hetero-2,7-naphthiporphyrin, by Szyszko, *et al*.[217] The compounds displayed formation of organophosphorus(V) complexes, proving the compounds ability to act as a macrocyclic ligand.

It is well-studied that two-photon absorption (2PA) properties are highly affected by the electronic and structural properties of a molecule, such as the length of its π-conjugation,[218-223] as well as its aromaticity and planarity.[93, 224-228] As previously mentioned, the photophysical properties of heteroporphyrins, namely carbaporphyrinoids, have not been studied in-depth even with their potential application within photodynamic therapy (PDT),[229] and sensor development,[230] and uses as catalysts,[231] and anion-binding agents.[232]

Herein, we measure the 2PA properties of three 28-hetero-2,7-naphthiporphyrins (Figure 55) where heterocycle D differs with the presence of sulfur (**1-S**), selenium (**1-Se**), and tellurium (**1-Te**) within the cavity of the macrocycle.[233]

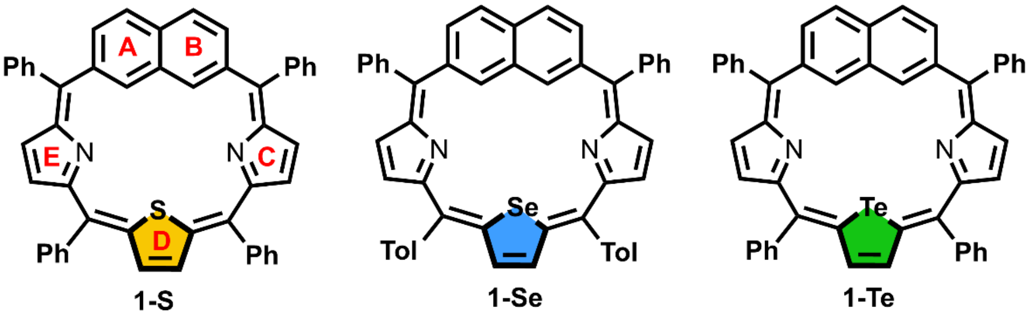

Figure 55. Structures of naphthiporphyrins **1-S**, **1-Se**, and **1-Te**.

The compounds are characterised using the Z-scan technique where very few carbaporphyrinoids have been measured regarding their non-linear optical properties.[234] Previous works that discuss the 2PA properties of uncommon porphyrinoids cover expanded porphyrins such as cyclo[n]pyrrole, amethyrin, and rubyrin,[93] *N*-confused hexaphyrins,[94] and biradicaloid *meso*-substituted [26]hexaphyrin (Figure 56).[95]

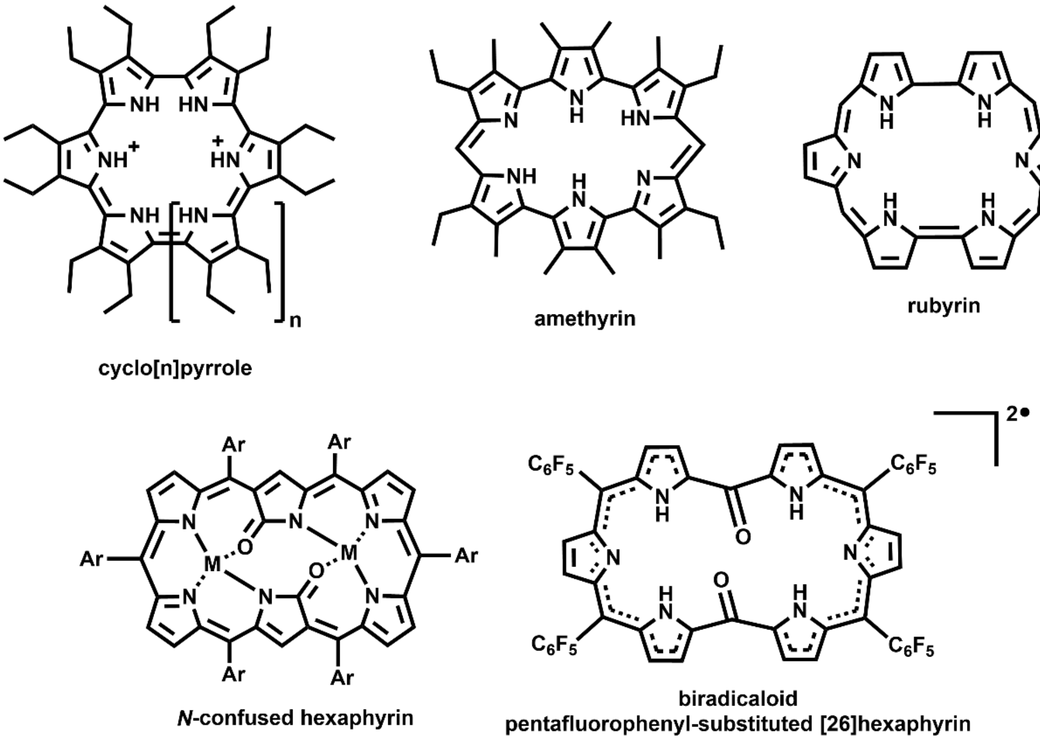

Figure 56. Structures of uncommon porphyrinoids and expanded porphyrins including cyclo[n]pyrrole, amethyrin, rubyrin, *N*-confused hexaphyrin, and biradicaloid *meso*-tetrakis(pentafluorophenyl)-substituted [26]hexaphyrin.

## 4.1 LINEAR OPTICAL PROPERTIES

Naphthiporphyrins **1-S**, **1-Se**, and **1-Te** were measured in HPLC grade dichloromethane (DCM) to make certain that no chemical changes of the molecules occurred throughout the experiments. Due to the amount of compound available to us, we were able to make two samples of **1-Se**. The samples only differed in concentration, **1-Se_0.5**, a 0.5% w/w solution, and **1-Se_1**, a 1% w/w solution. All four solutions were dark green in appearance. The UV-Vis spectra displayed an intense Soret-like band in the 347 – 358 nm wavelength range (Figure 57). All spectra also display a second, relatively intense, band in the 443 – 452 nm wavelength range.

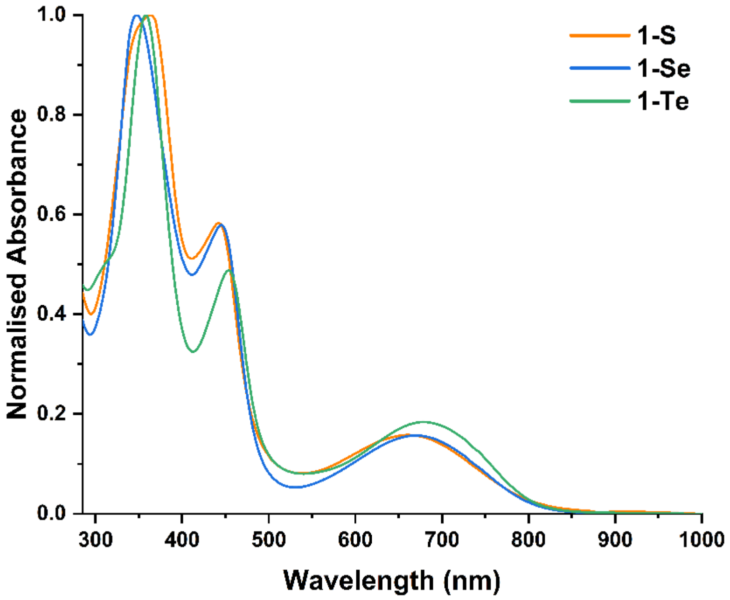

Figure 57. UV-Vis absorption spectra of porphyrinoids **1-S** (1% w/w), **1-Se** (1% w/w), and **1-Te** (1% w/w) (all were measured in DCM). Sample **1-Se_0.5** (0.5% w/w) displayed the same wavelength values as **1-Se_1**, so it has been omitted for clarity.

There is a broad absorption band present in all spectra over the 500 – 850 nm wavelength range, with maxima in this range at 661 nm for **1-S**, 670 nm for **1-Se** (the same for 0.5 and 1%), and 679 nm for **1-Te**. The bands and spectral patterns displayed here are characteristic of non-aromatic carbaporphyrinoids.[225] As the heterocycle ring D is changed from thiophene to selenophene to tellurophene, the absorption bands display a small bathochromic shift. The observed red-shift is also a commonly occurring effect and has been well-studied for heteroporphyrins[235] and heterocarbaporphyrinoids.[209, 217]. This effect is likely due to the electron delocalisation of the group 16 elements (chalcogens), as well as the increasing metallic nature as you move down the chalcogen group.[236] Another factor that may also have some effect on the photophysical properties is the difference in sizes of the heteroatoms (S, Se, and Te).[237] The larger Te affects the conformation of the macrocycle to a larger degree compared to S. Other changes in aromaticity and π-electron delocalisation may also have an effect on the photophysical properties.

## 4.2 NON-LINEAR OPTICAL PROPERTIES

Due to the differences of the heteroatoms present in heterocycle ring D, tellurium is the heaviest of the three and is less electronegative than selenium which in turn is less electronegative than sulfur, these lead to changes in the electron delocalisability and charge transfer of the naphthiporphyrins.[238] The presence of heavy atoms in the macrocycle not only red-shifts the bands in the 1PA spectra, it is also known to enhance the intersystem crossing (ISC) of a molecule, this phenomenon has been readily studied.[239-241] As 2PA is a third-order non-linear optical process, and it is known to be influenced by the charge transfer efficiency of a molecule,[242, 243] which is related to its electron-donor properties, it was decided to compare the 2PA cross-section ($\sigma_2$) values of **1-S**, **1-Se**, and **1-Te** via the Z-scan open-aperture technique.[53, 152, 244]

The maximum $\sigma_2$ values for these compounds were determined by measuring the 2PA at excitation wavelengths that correspond to twice the wavelength (2λ) region of the 1PA bands. This ensures that the 1PA contribution to the open aperture signal can be managed and minimised. This led to the measured wavelengths of 850 – 1600 nm for **1-S**, **1-Se_1**, and **1-Te_1** and 800 – 1600 nm for **1-Se_0.5**. The $\sigma_2$ values for the naphthiporphyrins were calculated and presented in Figure 58, plotted alongside the 1PA spectra at 2λ.

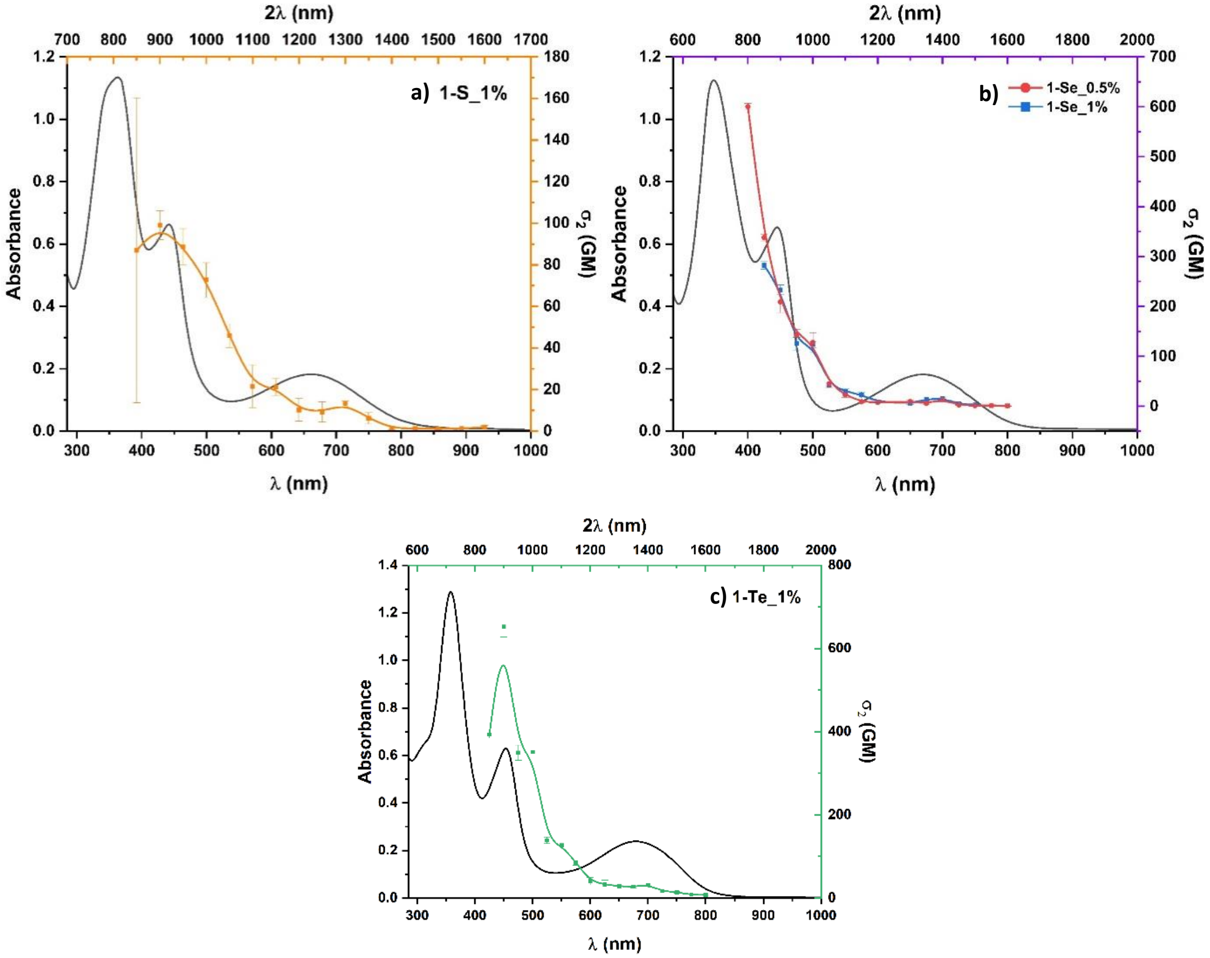

Figure 58. Overlay of the one-photon (solid black lines) and two-photon (solid colour lines) absorption spectra for a) **1-S** b) **1-Se_0.5** (red) and **1-Se_1** (blue) and c) **1-Te**. All measured in DCM. The 2PA cross-section values are derived from the Z-scan open-aperture measurements. The 1PA measurements are plotted against twice the wavelength (2λ).

The data in Figure 58 is presented such that the same excited states are reachable by both the 1PA and 2PA processes, this is common occurrence for non-centrosymmetric molecules.[245] However, it should be noted, that the relative strengths of the various 2PA absorption bands do not have to follow those of the 1PA spectra.

Two examples of the Z-scan open-aperture curves are displayed below (Figure 59) for 900 nm and 1400 nm of each molecule. It is apparent that **1-Te** displays the strongest non-linear absorption, followed by **1-Se**, with **1-S** displaying the weakest non-linear absorption. The non-linear absorption is almost undetectable at 1400 nm. The two differing concentrations of molecule **1-Se** (0.5% and 1%)

displays non-linear absorption that approximately scales with concentration, as shown in Table 6, the calculated values are in agreement.

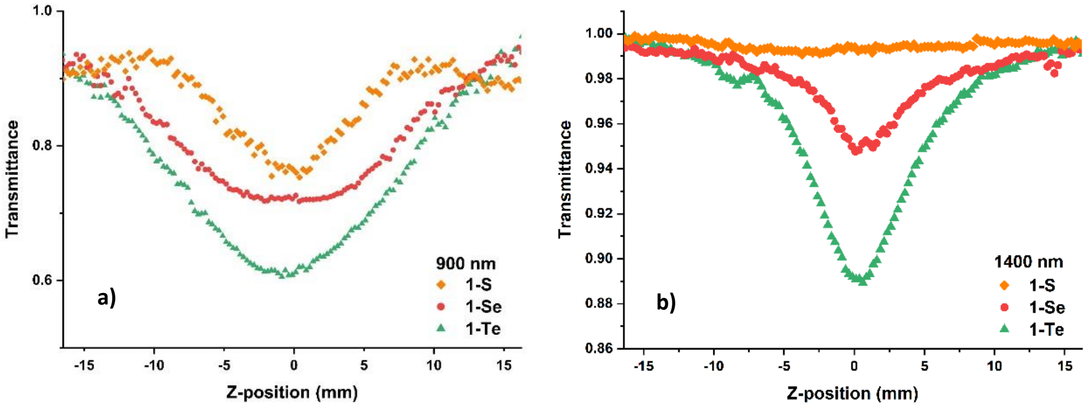

Figure 59. Z-scan open-aperture curves of **1-S**, **1-Se_0.5**, and **1-Te** at a) 900 nm and b) 1400 nm.

Table 6. Calculated two-photon absorption values of all investigated compounds, in DCM. *MW* represents molecular weight.

| **Compound** | **$\lambda_{2PA}$ (nm)** | **$\sigma_2$ (GM)** | **$\sigma_2/MW$ (GM $g^{-1}$)** |
|---|---|---|---|
| **1-S** | 900 | 99 ± 6.8 | 0.143 |
| | 1400 | 1.4 ± 0.8 | 0.002 |
| **1-Se_0.5** | 900 | 209 ± 22 | 0.272 |
| | 1400 | 13.2 ± 3 | 0.017 |
| **1-Se_1** | 900 | 233 ± 10 | 0.303 |
| | 1400 | 15.7 ± 1.5 | 0.020 |
| **1-Te** | 900 | 652 ± 25 | 0.826 |
| | 1400 | 31.5 ± 3 | 0.040 |

The calculated data demonstrates that all compounds show a comparatively weak 2PA maximum around 1400 nm, with the $\sigma_2$ value of **1-Te** being double that of **1-Se**, and **1-Se** being around 10 times higher than **1-S**. It is expected that maxima may appear at shorter wavelengths (between 700 and 900 nm), but this cannot be precisely due to the overlap of these wavelength ranges with the tail-end absorption of the 1PA spectra. The band observed at 900 nm (most prominent in **1-Te_1** 2PA spectrum) can be brought about by the existence of a knee-like feature in most two-photon spectra.[246] It is worth mentioning that the increase of $\sigma_2$, for **1-Se** at 800 nm, to 600 GM is likely to arise from the presence of excited state absorption. As mentioned, the tail-end absorption from the 1PA contribution is probably still too high at 800 nm, this can lead to an increase in the calculated $\sigma_2$ values most probably due to excited state absorption or absorption saturation. The $\sigma_2$ values may be higher at shorter wavelengths than those calculated here, but it is hard to obtain evidence of this due to the 1PA influence.

The calculated $\sigma_2$ values presented here further support the heavy atom effect, as changing from sulfur to selenium, and finally to the heavier tellurium, produces larger $\sigma_2$. Heavier atoms tend to possess increased electron density at their centre,[247-250] which is attributed to decreased electronegativity and increased electron donation as we move down the chalcogen group. These factors may lead to more efficient charge transfer, thus leading to the increased calculated $\sigma_2$ values. Further photophysical studies would allow confirmation of this mechanism. Such studies may also lead to better understanding of the role that electron donation and the heavy atom effect play. These factors also promote ISC due to large atomic number atoms able to induce strong spin-orbit coupling.[240, 251, 252] The heavy atom effect has been shown to effect photophysical properties,[253-256] as implied here with the increasing $\sigma_2$ values as we move to the heavier heavy atoms. All these effects are of significant interest for 2PA applications, such as PDT,[257-259] 2PA imaging,[260, 261] optical limiting,[262-264] optical data storage,[42, 265] microfabrication,[44, 45] amongst others.

The main interest in these experiments is the non-linear absorption properties that were derived from the Z-scan open-aperture measurements, but the closed-aperture measurements, in principle, also allow for the determination of both non-linear absorptive and refractive properties. These properties are commonly presented as the real (Re (γ)) and imaginary (Im (γ)) parts of the cubic hyperpolarisability (γ) of the compounds being studied.[266-268]

The spectra of the complex hyperpolarisability, γ (-ω; ω, -ω, ω) that were determined from the Z-scan closed-aperture measurements are shown in Figure 60. All three naphthiporphyrins have absolute values of Re (γ) and Im (γ) on the order of $10^{-33}$ esu. The imaginary part relates to the 2PA cross-section and it follows that of the spectral pattern of $\sigma_2$. The real part is negative for the majority of the investigated spectral region, this is typical for compounds that exhibit strong two-photon absorption. Experimentally, due to the high concentrations of the solutions, the solute contribution to the total refractive non-linearity of the solution is comparably high, this leads to sufficiently low errors in the calculations of Re (γ). As the heterocyclic ring changes from thiophene to selenophene to tellurophene there is an increase in γ.

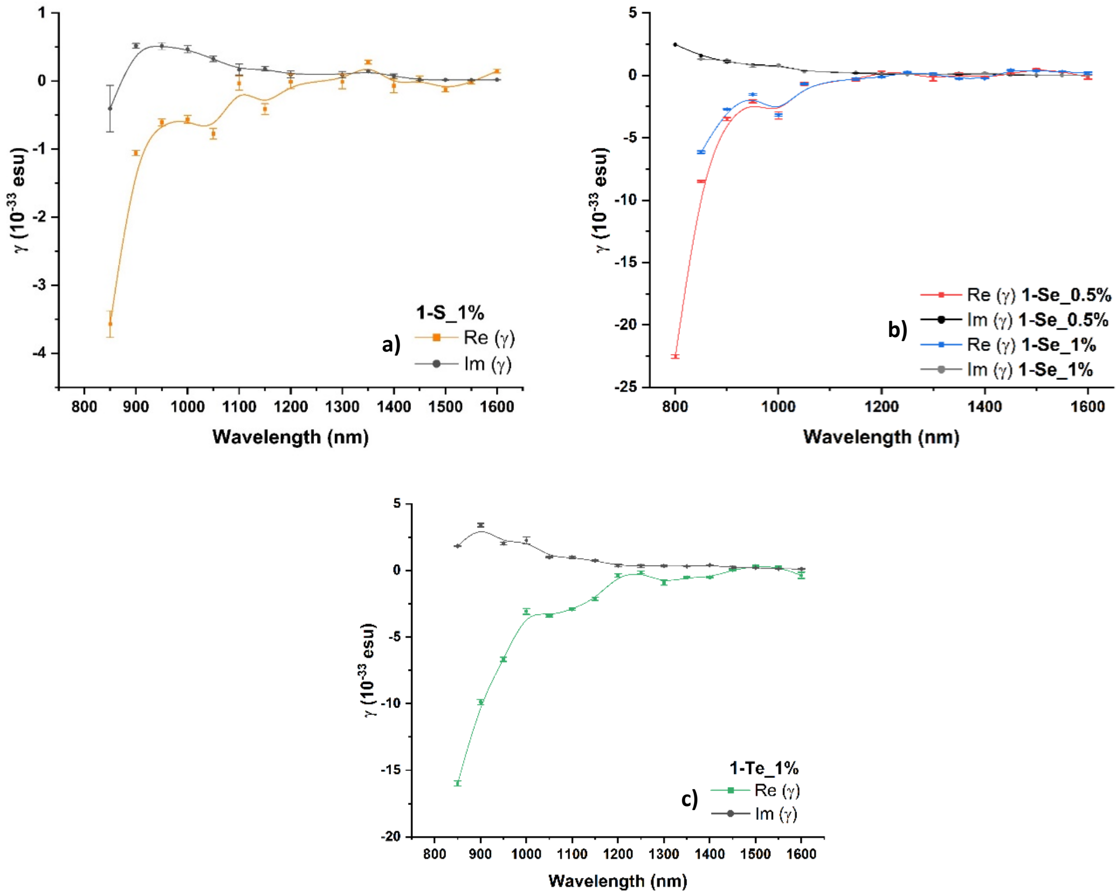

Figure 60. Spectra displaying the calculated real (Re) and imaginary (Im) parts of the hyperpolarisability, γ, derived from the Z-scan measurements for a) **1-S**, b) **1-Se_0.5** and **1-Se_1**, and c) **1-Te**.

It has been previously suggested that the decrease in the transition energy between the ground and the excited state is due to the heavier heteroatom, this transition energy is that involved in the transition that contributes to γ.[269, 270] This change in transition energy may also be a reason for the observed increase in $\sigma_2$ as we move from S to Se to Te. Particularly for **1-Te**, the calculated $\sigma_2$ values show a considerable enhancement compared to traditional macrocycles. The clear advantage of these naphthiporphyrins is their ability to absorb at longer wavelengths (> 1400 nm) compared to porphyrins that are used in the treatment of head and neck cancers, Foscan® = 652 nm and *meso*-tetra-4-hydroxyphenylporphyrin = 648 nm.[271] The potential use of naphthiporphyrins in similar applications is clear, further experiments will determine their compatibility, but we have provided another example demonstrating successful enhancement of 2PA properties.

## 4.3 CONCLUSION & OUTLOOK

The results from this investigation of one- and two-photon absorption properties of naphthiporphyrins **1-S**, **1-Se**, and **1-Te** show an improvement upon well-known photosensitizers that are currently used for PDT, as one example. The measured 2PA cross-sections may look to be moderate in comparison to much larger photosensitizers that have been measured in this context, but the moderate values were determined here at much longer wavelengths, 1400 nm, than has been previously recorded for such molecules. The 2PA values measured at 900 nm for **1-S** and **1-Te** are of a higher order of magnitude than well-known photosensitizers used for PDT, Foscan® has a reported $\sigma_2$ of 28 ± 8 GM (DMSO, $\lambda = 775$ nm).[65] These initial measurements demonstrate the promise of these compounds for their potential application in PDT, and other two-photon applications. Further investigations should be done to establish if these modifications to the macrocycle core can be utilised to create more expanded porphyrin-like molecules with further enhanced 2PA properties.

# Conclusion

## CONCLUSION AND PERSPECTIVES

During this work, in the first chapter, we have successfully demonstrated that porphyrins encapsulated in acetylated lignin nanoparticles are capable of emitting in the NIR range upon two-photon excitation. The porphyrin-loaded lignin nanoparticle hybrid dispersions were measured using two-photon excited fluorescence and two-photon fluorescence microscopy.

In the second chapter, we have successfully shown the modifications of existing photosensitizer Foscan® have enhanced two-photon absorption properties, particularly demonstrated by the calculated two-photon absorption cross-section values being 2.6-fold increased upon that of Foscan®.

In the next part of our work, we carried out the synthesis of a π-conjugated extended porphyrin to develop its two-photon absorption properties for their prospective use within photodynamic therapy. A porphyrin-type, tetrapyrrolic macrocycle, was aimed to be coupled with a para-substituted pyrimidine heterocycle. For this coupling step we utilised the Sonogashira reaction, though we were unsuccessful here, and future optimisation of this step will be required. However, the uncoupled porphyrin structures were measured and characterised for their two-photon absorption properties via Z-scan measurements, with the synthesised compounds also being characterised by a mixture of standard structural analysis methods, including $^1$H-NMR, UV-Visible absorption, and mass spectrometry. The measured two-photon absorption cross-section values for the three uncoupled porphyrins demonstrated that as the conjugation increased so thus did the cross-section value. The additional heavy-atom effect also induced an enhancement effect. Coupling of these porphyrins with the pyrimidine heterocycle should provide further information on the conjugation effect and whether it will lead to greater enhancement of their non-linear optical properties, with biological (*in vitro*) tests being required to determine their applicability in aqueous environments.

The final part of this work demonstrated the two-photon absorption at extended wavelength values of up to 1600 nm. The one- and two-photon absorption properties of three naphthiporphyrins were measured using UV-Visible absorption and the Z-scan technique, respectively. The moderate two-photon absorption cross-section values recorded at 1400 nm is the longest wavelength that these types of compounds have been measured at before. These compounds show great potential for their use within two-photon and photodynamic therapy applications. Further investigations would be able to determine the usefulness of these compounds and their modifications in the design and creation of more expanded macrocycles with enhanced two-photon absorbing capabilities.

# REFERENCES

1. J. Feyh, *Journal of Photochemistry and Photobiology B: Biology*, 1996, **36**, 175-177.
2. S. M. Gondivkar, A. R. Gadbail, M. G. Choudhary, P. R. Vedpathak and M. S. Likhitkar, *Journal of investigative and clinical dentistry*, 2018, **9**, e12270.
3. A. Allegra, G. Pioggia, A. Tonacci, C. Musolino and S. Gangemi, *Antioxidants*, 2020, **9**, 448.
4. Á. Juarranz, Y. Gilaberte and S. González, *Journal*, 2020, **12**, 3341.
5. I. Wada, S. Shiose, K. Ishikawa, K. Kano, S. Notomi, K. Mori, M. Akiyama, S. Nakao and K.-H. Sonoda, *Graefe's Archive for Clinical and Experimental Ophthalmology*, 2022, 1-8.
6. A. Armbrecht, P. Aspinall and B. Dhillon, *British Journal of Ophthalmology*, 2004, **88**, 1270-1273.
7. J. Gray and G. Fullarton, *Photodiagnosis and Photodynamic Therapy*, 2007, **4**, 151-159.
8. K. Moghissi, K. Dixon, M. Stringer and J. Thorpe, *Photodiagnosis and photodynamic therapy*, 2009, **6**, 159-166.
9. J. Xiao, L. Cheng, T. Fang, Y. Zhang, J. Zhou, R. Cheng, W. Tang, X. Zhong, Y. Lu and L. Deng, *Small*, 2019, **15**, 1904979.
10. D. Andreadis, A.-M. Pavlou, E. Sotiriou, F. Vrani, D. Ioannides and A. Kolokotronis, *Translational Research in Oral Oncology*, 2016, **1**, 2057178X16669161.
11. R. Saini, N. V. Lee, K. Y. Liu and C. F. Poh, *Cancers*, 2016, **8**, 83.
12. H. Liu, L. Daly, G. Rudd, A. P. Khan, S. Mallidi, Y. Liu, F. Cuckov, T. Hasan and J. P. Celli, *Lasers in surgery and medicine*, 2019, **51**, 345-351.
13. S. Khan, M. B. Hussain, A. P. Khan, H. Liu, S. Siddiqui, S. Mallidi, P. L. Alacron, L. Daly, G. Rudd and F. Cuckov, *Journal of biomedical optics*, 2020, **25**, 063813.
14. J. Usuda, H. Kato, T. Okunaka, K. Furukawa, H. Tsutsui, K. Yamada, Y. Suga, H. Honda, Y. Nagatsuka and T. Ohira, *Journal of thoracic oncology*, 2006, **1**, 489-493.
15. R. Allison, K. Moghissi, G. Downie and K. Dixon, *Photodiagnosis and photodynamic therapy*, 2011, **8**, 231-239.
16. K. Wang, B. Yu and J. L. Pathak, *Journal of Cancer*, 2021, **12**, 1154.
17. M. Kim, H. Y. Jung and H. J. Park, *International journal of molecular sciences*, 2015, **16**, 23259-23278.
18. C. Theresia, J. Zheng and X.-Y. Chen, *Photodiagnosis and Photodynamic Therapy*, 2017, **20**, 189-192.
19. M. Wainwright, *The Journal of antimicrobial chemotherapy*, 1998, **42**, 13-28.

20. Y. Ilizirov, A. Formanovsky, I. Mikhura, Y. Paitan, F. Nakonechny and M. Nisnevitch, *Molecules*, 2018, **23**, 3152.
21. S. Banerjee, D. Ghosh, K. Vishakha, S. Das, S. Mondal and A. Ganguli, *Photodiagnosis and Photodynamic Therapy*, 2020, **32**, 102002.
22. N. Higuchi, J.-i. Hayashi, M. Fujita, Y. Iwamura, Y. Sasaki, R. Goto, T. Ohno, E. Nishida, G. Yamamoto and T. Kikuchi, *International Journal of Molecular Sciences*, 2021, **22**, 8384.
23. M. Wainwright, *Chemical Society Reviews*, 2002, **31**, 128-136.
24. L. Sobotta, P. Skupin-Mrugalska, J. Mielcarek, T. Goslinski and J. Balzarini, *Mini reviews in medicinal chemistry*, 2015, **15**, 503-521.
25. L. Marciel, L. Teles, B. Moreira, M. Pacheco, L. M. Lourenço, M. G. Neves, J. P. Tome, M. A. Faustino and A. Almeida, *Future Medicinal Chemistry*, 2017, **9**, 365-379.
26. G. M. F. Calixto, J. Bernegossi, L. M. De Freitas, C. R. Fontana and M. Chorilli, *Molecules*, 2016, **21**, 342.
27. L.-O. Klotz, K.-D. Kröncke and H. Sies, *Photochemical & photobiological sciences*, 2003, **2**, 88-94.
28. J. Mosinger, O. Jirsák, P. Kubát, K. Lang and B. Mosinger, *Journal of materials chemistry*, 2007, **17**, 164-166.
29. C. Flors and S. Nonell, *Accounts of chemical research*, 2006, **39**, 293-300.
30. A. Späth, C. Leibl, F. Cieplik, K. Lehner, J. Regensburger, K.-A. Hiller, W. Bäumler, G. Schmalz and T. Maisch, *Journal of medicinal chemistry*, 2014, **57**, 5157-5168.
31. F. Wilkinson, W. P. Helman and A. B. Ross, *Journal of Physical and Chemical Reference Data*, 1995, **24**, 663-677.
32. P. R. Ogilby, *Chemical Society Reviews*, 2010, **39**, 3181-3209.
33. R. R. Allison and K. Moghissi, *Clinical endoscopy*, 2013, **46**, 24.
34. B. P. Joshi and T. D. Wang, *Cancers (Basel)*, 2010, **2**, 1251-1287.
35. I. Yoon, J. Z. Li and Y. K. Shim, *Clinical endoscopy*, 2013, **46**, 7.
36. A. M. Smith, M. C. Mancini and S. Nie, *Nature nanotechnology*, 2009, **4**, 710-711.
37. H. Kobayashi, M. Ogawa, R. Alford, P. L. Choyke and Y. Urano, *Chemical reviews*, 2010, **110**, 2620-2640.
38. M. Rumi and J. W. Perry, *Advances in Optics and Photonics*, 2010, **2**, 451-518.
39. E. Robbins, S. Leroy-Lhez, N. Villandier, M. Samoć and K. Matczyszyn, *Molecules*, 2021, **26**, 6323.
40. M. Pawlicki, H. A. Collins, R. G. Denning and H. L. Anderson, *Angewandte Chemie International Edition*, 2009, **48**, 3244-3266.

41. W. Kaiser and C. Garrett, *Physical review letters*, 1961, **7**, 229.
42. B. H. Cumpston, S. P. Ananthavel, S. Barlow, D. L. Dyer, J. E. Ehrlich, L. L. Erskine, A. A. Heikal, S. M. Kuebler, I.-Y. S. Lee and D. McCord-Maughon, *Nature*, 1999, **398**, 51-54.
43. Q. Zhang, S. Yue, H. Sun, X. Wang, X. Hao and S. An, *Journal of Materials Chemistry C*, 2017, **5**, 3838-3847.
44. F. Niesler and M. Hermatschweiler, *Optik & Photonik*, 2016, **11**, 54-57.
45. E. Scarpa, E. D. Lemma, R. Fiammengo, M. P. Cipolla, F. Pisanello, F. Rizzi and M. De Vittorio, *Sensors and Actuators B: Chemical*, 2019, **279**, 418-426.
46. J. Lee, Y. Arita, S. Toyoshima, K. Miyamoto, P. Panagiotopoulos, E. M. Wright, K. Dholakia and T. Omatsu, *ACS Photonics*, 2018, **5**, 4156-4163.
47. X. Xu, J. B. Madrigal, A. Broussier, G. E. Lio, F. Geoffray, A. Issa, S. Jradi, R. Bachelot, C. Couteau and S. Blaize, 2020.
48. B. Gu, W. Wu, G. Xu, G. Feng, F. Yin, P. H. J. Chong, J. Qu, K. T. Yong and B. Liu, *Advanced Materials*, 2017, **29**, 1701076.
49. L. K. McKenzie, H. E. Bryant and J. A. Weinstein, *Coordination Chemistry Reviews*, 2019, **379**, 2-29.
50. W. Fan, P. Huang and X. Chen, *Chemical Society Reviews*, 2016, **45**, 6488-6519.
51. J. V. Garcia, F. Zhang and P. C. Ford, *Philosophical Transactions of the Royal Society A: Mathematical, Physical and Engineering Sciences*, 2013, **371**, 20120129.
52. V. Gupta, *Molecular and laser spectroscopy: advances and applications*, Elsevier, 2017.
53. L. M. Mazur, T. Roland, S. Leroy-Lhez, V. Sol, M. Samoc, I. D. Samuel and K. Matczyszyn, *The Journal of Physical Chemistry B*, 2019, **123**, 4271-4277.
54. J. Schmitt, V. Heitz, A. Sour, F. Bolze, H. Ftouni, J. F. Nicoud, L. Flamigni and B. Ventura, *Angewandte Chemie*, 2015, **127**, 171-175.
55. J. Schmitt, V. Heitz, S. Jenni, A. Sour, F. Bolze and B. Ventura, *Supramolecular Chemistry*, 2017, **29**, 769-775.
56. M. Zhu, J. Zhang, Y. Zhou, P. Xing, L. Gong, C. Su, D. Qi, H. Du, Y. Bian and J. Jiang, *Inorganic Chemistry*, 2018, **57**, 11537-11542.
57. T. L. Poulos, *Chemical reviews*, 2014, **114**, 3919-3962.
58. C. Rovira, *Journal of Physics: Condensed Matter*, 2003, **15**, S1809.
59. S. R. De Annunzio, N. C. S. Costa, R. D. Mezzina, M. A. Graminha and C. R. Fontana, *International Journal of Molecular Sciences*, 2019, **20**, 3861.
60. K. Chen, 2010.

61. G. Lozovaya, Z. Masinovsky and A. Sivash, *Origins of life and evolution of the biosphere*, 1990, **20**, 321-330.
62. I. B. Tan, G. Dolivet, P. Ceruse, V. V. Poorten, G. Roest and W. Rauschning, *Head & neck*, 2010, **32**, 1597-1604.
63. M. Dilkes and U. Bapat, *Otolaryngology-Head and Neck Surgery*, 2004, **131**, P74-P75.
64. R. R. Allison, G. H. Downie, R. Cuenca, X.-H. Hu, C. J. Childs and C. H. Sibata, *Photodiagnosis and photodynamic therapy*, 2004, **1**, 27-42.
65. B. Hamed, T. von Haimberger, V. Kozich, A. Wiehe and K. Heyne, *Journal of Photochemistry and Photobiology A: Chemistry*, 2014, **295**, 53-56.
66. C.-K. Wang, P. Macak, Y. Luo and H. Ågren, *The Journal of chemical physics*, 2001, **114**, 9813-9820.
67. L. Xu, J. Zhang, L. Yin, X. Long, W. Zhang and Q. Zhang, *Journal of Materials Chemistry C*, 2020, **8**, 6342-6349.
68. W. Sharmoukh, A. Attanzio, E. Busatto, T. Etienne, S. Carli, A. Monari, X. Assfeld, M. Beley, S. Caramori and P. C. Gros, *RSC Advances*, 2015, **5**, 4041-4050.
69. O. Sengul, E. B. Boydas, M. Pastore, W. Sharmouk, P. C. Gros, S. Catak and A. Monari, *Theoretical Chemistry Accounts*, 2017, **136**, 1-9.
70. H. Wang, B. Fang, L. Kong, X. Li, Z. Feng, Y. Wu, K. Uvdal and Z. Hu, *Spectrochimica Acta Part A: Molecular and Biomolecular Spectroscopy*, 2018, **198**, 304-308.
71. Y. Zheng, S. Sun, L. Xu, S. Ni, W. Liu, B. Huang, Q. Huang, Q. Zhang, F. Lu and M.-D. Li, *Dyes and Pigments*, 2019, **165**, 301-307.
72. L. Dykman and N. Khlebtsov, *Acta Naturae (англоязычная версия)*, 2011, **3**, 34-55.
73. D. A. Giljohann, D. S. Seferos, W. L. Daniel, M. D. Massich, P. C. Patel and C. A. Mirkin, *Spherical Nucleic Acids*, 2020, 55-90.
74. G.-D. Zhang, A. Harada, N. Nishiyama, D.-L. Jiang, H. Koyama, T. Aida and K. Kataoka, *Journal of controlled release*, 2003, **93**, 141-150.
75. D.-Q. Wu, Z.-Y. Li, C. Li, J.-J. Fan, B. Lu, C. Chang, S.-X. Cheng, X.-Z. Zhang and R.-X. Zhuo, *Pharmaceutical research*, 2010, **27**, 187-199.
76. K. Sugisaki, T. Usui, N. Nishiyama, W.-D. Jang, Y. Yanagi, S. Yamagami, S. Amano and K. Kataoka, *Investigative ophthalmology & visual science*, 2008, **49**, 894-899.
77. G. Marchand, G. Fabre, N. Maldonado-Carmona, N. Villandier and S. Leroy-Lhez, *Nanoscale Advances*, 2020, **2**, 5648-5658.
78. N. Maldonado-Carmona, T.-S. Ouk, N. Villandier, C. A. Calliste, M. J. Calvete, M. M. Pereira and S. Leroy-Lhez, *Antibiotics*, 2021, **10**, 513.

79. E. Feese, H. Sadeghifar, H. S. Gracz, D. S. Argyropoulos and R. A. Ghiladi, *Biomacromolecules*, 2011, **12**, 3528-3539.

80. M. Krouit, R. Granet, P. Branland, B. Verneuil and P. Krausz, *Bioorganic & Medicinal Chemistry Letters*, 2006, **16**, 1651-1655.

81. S. Li, X.-F. Jiang and Q.-H. Xu, *Science China Chemistry*, 2018, **61**, 88-96.

82. S. S. Lucky, K. C. Soo and Y. Zhang, *Chemical reviews*, 2015, **115**, 1990-2042.

83. X. Shen, L. Li, H. Wu, S. Q. Yao and Q.-H. Xu, *Nanoscale*, 2011, **3**, 5140-5146.

84. E. Dahlstedt, H. A. Collins, M. Balaz, M. K. Kuimova, M. Khurana, B. C. Wilson, D. Phillips and H. L. Anderson, *Organic & biomolecular chemistry*, 2009, **7**, 897-904.

85. J. T. Dy, K. Ogawa, A. Satake, A. Ishizumi and Y. Kobuke, *Chemistry–A European Journal*, 2007, **13**, 3491-3500.

86. H. Huang, B. Yu, P. Zhang, J. Huang, Y. Chen, G. Gasser, L. Ji and H. Chao, *Angewandte Chemie International Edition*, 2015, **54**, 14049-14052.

87. L. K. McKenzie, I. V. Sazanovich, E. Baggaley, M. Bonneau, V. Guerchais, J. G. Williams, J. A. Weinstein and H. E. Bryant, *Chemistry–A European Journal*, 2017, **23**, 234-238.

88. O. Mongin, V. Hugues, M. Blanchard-Desce, A. Merhi, S. Drouet, D. Yao and C. Paul-Roth, *Chemical Physics Letters*, 2015, **625**, 151-156.

89. M. A. Oar, J. M. Serin, W. R. Dichtel, J. M. Fréchet, T. Y. Ohulchanskyy and P. N. Prasad, *Chemistry of Materials*, 2005, **17**, 2267-2275.

90. T. Chatterjee, V. S. Shetti, R. Sharma and M. Ravikanth, *Chemical Reviews*, 2017, **117**, 3254-3328.

91. T. D. Lash, *Organic & Biomolecular Chemistry*, 2015, **13**, 7846-7878.

92. T. D. Lash, A. M. Young, J. M. Rasmussen and G. M. Ferrence, *J. Org. Chem.*, 2011, **76**, 5636-5651.

93. Z. S. Yoon, J. H. Kwon, M.-C. Yoon, M. K. Koh, S. B. Noh, J. L. Sessler, J. T. Lee, D. Seidel, A. Aguilar and S. Shimizu, *J. Am. Chem. Soc.*, 2006, **128**, 14128-14134.

94. J. H. Kwon, T. K. Ahn, M.-C. Yoon, D. Y. Kim, M. K. Koh, D. Kim, H. Furuta, M. Suzuki and A. Osuka, *The Journal of Physical Chemistry B*, 2006, **110**, 11683-11690.

95. T. Koide, K. Furukawa, H. Shinokubo, J.-Y. Shin, K. S. Kim, D. Kim and A. Osuka, *Journal of the American Chemical Society*, 2010, **132**, 7246-7247.

96. J. L. Sessler and D. Seidel, *Angewandte Chemie International Edition*, 2003, **42**, 5134-5175.

97. T. D. Lash, *European Journal of Organic Chemistry*, 2007, **2007**, 5461-5481.

98. B. Gu, W. Wu, G. Xu, G. Feng, F. Yin, P. H. J. Chong, J. Qu, K. T. Yong and B. Liu, *Adv Mater*, 2017, **29**.

99. X. Shen, S. Li, L. Li, S. Q. Yao and Q. H. Xu, *Chemistry*, 2015, **21**, 2214-2221.

100. S. Li, X. Shen, L. Li, P. Yuan, Z. Guan, S. Q. Yao and Q. H. Xu, *Langmuir*, 2014, **30**, 7623-7627.

101. W. Tang, H. Xu, E. J. Park, M. A. Philbert and R. Kopelman, *Biochem Biophys Res Commun*, 2008, **369**, 579-583.

102. P. Du, X. Huang and J. S. Yu, *Chemical Engineering Journal*, 2018, **337**, 91-100.

103. J. Pennakalathil, E. Jahja, E. S. Özdemir, O. z. Konu and D. n. s. Tuncel, *Biomacromolecules*, 2014, **15**, 3366-3374.

104. G. Tian, W. Ren, L. Yan, S. Jian, Z. Gu, L. Zhou, S. Jin, W. Yin, S. Li and Y. Zhao, *Small*, 2013, **9**, 1929-1938.

105. Q. Tang, Y. Qian, D. Yang, X. Qiu, Y. Qin and M. Zhou, *Polymers*, 2020, **12**, 2471.

106. P. Duarah, D. Haldar and M. K. Purkait, *International Journal of Biological Macromolecules*, 2020, **163**, 1828-1843.

107. P. Figueiredo, K. Lintinen, A. Kiriazis, V. Hynninen, Z. Liu, T. Bauleth-Ramos, A. Rahikkala, A. Correia, T. Kohout and B. Sarmento, *Biomaterials*, 2017, **121**, 97-108.

108. L. Dai, Y. Li, F. Kong, K. Liu, C. Si and Y. Ni, *ACS Sustainable Chemistry & Engineering*, 2019, **7**, 13497-13504.

109. V. K. Thakur, M. K. Thakur, P. Raghavan and M. R. Kessler, *ACS Sustain. Chem. Eng.*, 2014, **2**, 1072-1092.

110. R. Rinaldi, R. Jastrzebski, M. T. Clough, J. Ralph, M. Kennema, P. C. Bruijnincx and B. M. Weckhuysen, *Angew. Chem. Int. Ed.*, 2016, **55**, 8164-8215.

111. V. Ugartondo, M. Mitjans and M. P. Vinardell, *Bioresour. Technol.*, 2008, **99**, 6683-6687.

112. A. Barapatre, A. S. Meena, S. Mekala, A. Das and H. Jha, *Int. J. Biol. Macromol.*, 2016, **86**, 443-453.

113. O. Gordobil, R. Herrera, M. Yahyaoui, S. İlk, M. Kaya and J. Labidi, *RSC Adv.*, 2018, **8**, 24525-24533.

114. G. J. Gil-Chávez, S. S. P. Padhi, C. V. Pereira, J. N. Guerreiro, A. A. Matias and I. Smirnova, *Int. J. Biol. Macromol.*, 2019, **136**, 697-703.

115. M. H. Sipponen, H. Lange, C. Crestini, A. Henn and M. Österberg, *ChemSusChem*, 2019, **12**, 2039.

116. S. Iravani and R. S. Varma, *Green Chem.*, 2020, **22**, 612-636.

117. P. Figueiredo, K. Lintinen, J. T. Hirvonen, M. A. Kostiainen and H. A. Santos, *Prog. Mater Sci.*, 2018, **93**, 233-269.

118. G. Marchand, C. A. Calliste, R. M. Williams, C. McLure, S. Leroy-Lhez and N. Villandier, *ChemistrySelect*, 2018, **3**, 5512-5516.

119. M. Zhou, D. Wang, D. Yang, X. Qiu and Y. Li, *Ind Crops Prod.*, 2019, **137**, 453-459.

120. N. Maldonado-Carmona, T.-S. Ouk, M. J. Calvete, M. M. Pereira, N. Villandier and S. Leroy-Lhez, *Photochem. Photobiol. Sci.*, 2020, **19**, 445-461.

121. N. Maldonado-Carmona, G. Marchand, N. Villandier, T.-S. Ouk, M. M. Pereira, M. J. Calvete, C. A. Calliste, A. Żak, M. Piksa and K. J. Pawlik, *Front. Microbiol.*, 2020, **11**.

122. L. M. Jose, S. Kuriakose and T. Mathew, *Photodiagnosis and Photodynamic Therapy*, 2021, **36**, 102479.

123. F. Bolze, S. Jenni, A. Sour and V. Heitz, *Chem. Commun.*, 2017, **53**, 12857-12877.

124. W. Zhuang, L. Yang, B. Ma, Q. Kong, G. Li, Y. Wang and B. Z. Tang, *ACS applied materials & interfaces*, 2019, **11**, 20715-20724.

125. I. Yoon, J. Z. Li and Y. K. Shim, *Clin Endosc*, 2013, **46**, 7-23.

126. E. Hemmer, A. Benayas, F. Légaré and F. Vetrone, *Nanoscale Horizons*, 2016, **1**, 168-184.

127. D. C. Sordillo, L. A. Sordillo, P. P. Sordillo, L. Shi and R. R. Alfano, *J. Biomed. Opt.*, 2017, **22**, 045002.

128. Y. Shen, A. J. Shuhendler, D. Ye, J.-J. Xu and H.-Y. Chen, *Chem. Soc. Rev.*, 2016, **45**, 6725-6741.

129. Y. Zhou, X. Liang and Z. Dai, *Nanoscale*, 2016, **8**, 12394-12405.

130. Z.-A. Chen, Y. Kuthati, R. K. Kankala, Y.-C. Chang, C.-L. Liu, C.-F. Weng, C.-Y. Mou and C.-H. Lee, *Science and technology of advanced materials*, 2015.

131. A. Vargas, B. Pegaz, E. Debefve, Y. Konan-Kouakou, N. Lange, J.-P. Ballini, H. van den Bergh, R. Gurny and F. Delie, *Int. J. Pharm.*, 2004, **286**, 131-145.

132. C. Xu and W. W. Webb, *JOSA B*, 1996, **13**, 481-491.

133. J. Mertz, C. Xu and W. Webb, *Opt. Lett.*, 1995, **20**, 2532-2534.

134. M. Drobizhev, S. Tillo, N. Makarov, T. Hughes and A. Rebane, *J. Phys. Chem. B.*, 2009, **113**, 855-859.

135. N. S. Makarov, M. Drobizhev and A. Rebane, *Optics express*, 2008, **16**, 4029-4047.

136. G. Binnig, *Ultramicroscopy*, 1992, **42**, 7-15.

137. F. J. Giessibl, *Rev. Mod. Phys.*, 2003, **75**, 949.

138. P. T. So, C. Y. Dong, B. R. Masters and K. M. Berland, *Annu. Rev. Biomed. Eng.*, 2000, **2**, 399-429.

139. M. Oheim, D. J. Michael, M. Geisbauer, D. Madsen and R. H. Chow, *Adv. Drug Del. Rev.*, 2006, **58**, 788-808.

140. Z. Zhang, X. Zhang, Z. Xin, M. Deng, Y. Wen and Y. Song, *Adv. Mater.*, 2013, **25**, 6714-6718.

141. M. E. Johnson, A. R. M. Bustos and M. R. Winchester, *Anal. Bioanal. Chem.*, 2016, **408**, 7629-7640.

142. J. D. Robertson, L. Rizzello, M. Avila-Olias, J. Gaitzsch, C. Contini, M. S. Magoń, S. A. Renshaw and G. Battaglia, *Sci. Rep.*, 2016, **6**, 1-9.

143. R. Teixeira, V. V. Serra, D. Botequim, P. M. Paulo, S. M. Andrade and S. Costa, *Molecules*, 2021, **26**, 4264.

144. Y. Terazono, G. Kodis, M. Chachisvilis, B. R. Cherry, M. Fournier, A. Moore, T. A. Moore and D. Gust, *J. Am. Chem. Soc.*, 2015, **137**, 245-258.

145. M. Taniguchi, J. S. Lindsey, D. F. Bocian and D. Holten, *Journal of Photochemistry and Photobiology C: Photochemistry Reviews*, 2021, 100401.

146. Z. Ma, C. Liu, N. Niu, Z. Chen, S. Li, S. Liu and J. Li, *ACS Sustain. Chem. Eng.*, 2018, **6**, 3169-3175.

147. W. Chen, C.-A. Cheng, E. D. Cosco, S. Ramakrishnan, J. G. Lingg, O. T. Bruns, J. I. Zink and E. M. Sletten, *J. Am. Chem. Soc.*, 2019, **141**, 12475-12480.

148. I. Gosens, J. A. Post, L. J. de la Fonteyne, E. H. Jansen, J. W. Geus, F. R. Cassee and W. H. de Jong, *Part. Fibre Toxicol.*, 2010, **7**, 1-11.

149. M. A. Ashraf, W. Peng, Y. Zare and K. Y. Rhee, *Nanoscale research letters*, 2018, **13**, 1-7.

150. I. S. Mfouo-Tynga, L. D. Dias, N. M. Inada and C. Kurachi, *Photodiagnosis and Photodynamic Therapy*, 2021, **34**, 102091.

151. J. Wang, M. Sheik-Bahae, A. A. Said, D. J. Hagan and E. W. Van Stryland, *J Opt. Soc Am B.*, 1994, **11**.

152. M. Sheik-Bahae, A. A. Said, T.-H. Wei, Y.-Y. Wu, D. J. Hagan, M. Soileau and E. W. Van Stryland, San Diego, CA, 1989.

153. Z. Sun, L. P. Zhang, F. Wu and Y. Zhao, *Advanced Functional Materials*, 2017, **27**, 1704079.

154. N. Sheng, D. Liu, J. Wu, B. Gu, Z. Wang and Y. Cui, *Dyes and Pigments*, 2015, **119**, 116-121.

155. Ò. Rubio-Pons, Y. Luo and H. Ågren, *The Journal of chemical physics*, 2006, **124**, 094310.

156. M. O. Senge and J. C. Brandt, *Photochemistry and photobiology*, 2011, **87**, 1240-1296.

157. R. Baskaran, J. Lee and S.-G. Yang, *Biomaterials research*, 2018, **22**, 1-8.

158. R. Bonnett, B. D. Djelal and A. Nguyen, *Journal of Porphyrins and Phthalocyanines*, 2001, **5**, 652-661.

159. R. Bonnett, R. D. White, U.-J. Winfield and M. C. Berenbaum, *Biochemical Journal*, 1989, **261**, 277.

160. P. Gierlich, S. Mucha, E. Robbins, L. Gomes-Da-Silva, K. Matczyszyn and M. Senge, *ChemPhotoChem*, 2021.

161. B. Khurana, P. Gierlich, A. Meindl, L. C. Gomes-da-Silva and M. O. Senge, *Photochemical & Photobiological Sciences*, 2019, **18**, 2613-2656.

162. I. Maliszewska, E. Wanarska, A. C. Thompson, I. D. Samuel and K. Matczyszyn, *Molecules*, 2021, **26**, 623.

163. I. Maliszewska, B. Lisiak, K. Popko and K. Matczyszyn, *Photochemistry and Photobiology*, 2017, **93**, 1081-1090.

164. N. S. Makarov, J. Campo, J. M. Hales and J. W. Perry, *Optical materials express*, 2011, **1**, 551-563.

165. R. Medishetty, J. K. Zaręba, D. Mayer, M. Samoć and R. A. Fischer, *Chemical Society Reviews*, 2017, **46**, 4976-5004.

166. M. Samoc, K. Matczyszyn, M. Nyk, J. Olesiak-Banska, D. Wawrzynczyk, P. Hanczyc, J. Szeremeta, M. Wielgus, M. Gordel, L. Mazur, R. Kolkowski, B. Straszak, M. Cifuentes and M. Humphrey, *Nonlinear absorption and nonlinear refraction: maximizing the merit factors*, SPIE, 2012.

167. R. L. Roberts, T. Schwich, T. C. Corkery, M. P. Cifuentes, K. A. Green, J. D. Farmer, P. J. Low, T. B. Marder, M. Samoc and M. G. Humphrey, *Advanced Materials*, 2009, **21**, 2318-2322.

168. X. Long, J. Wu, S. Yang, Z. Deng, Y. Zheng, W. Zhang, X.-F. Jiang, F. Lu and L. Xu, *Journal of Materials Chemistry C*, 2021, **9**, 11679-11689.

169. L. Luo, Q. Zhang, Y. Luo, Z. He, X. Tian and G. Battaglia, *Journal of controlled release*, 2019, **298**, 99-109.

170. S. G. Mucha, L. Firlej, J.-L. Bantignies, A. Żak, M. Samoć and K. Matczyszyn, *RSC advances*, 2020, **10**, 38437-38445.

171. S. Sumalekshmy, M. M. Henary, N. Siegel, P. V. Lawson, Y. Wu, K. Schmidt, J.-L. Brédas, J. W. Perry and C. J. Fahrni, *Journal of the American Chemical Society*, 2007, **129**, 11888-11889.

172. M. Atif, P. Dyer, T. A. Paget, H. Snelling and M. Stringer, *Photodiagnosis and photodynamic therapy*, 2007, **4**, 106-111.

173. D. Wawrzyńczyk, *Journal of Materials Chemistry C*, 2017, **5**, 1724-1729.

174. S. H. Yau, N. Abeyasinghe, M. Orr, L. Upton, O. Varnavski, J. H. Werner, H.-C. Yeh, J. Sharma, A. P. Shreve and J. S. Martinez, *Nanoscale*, 2012, **4**, 4247-4254.

175. J. Arnbjerg, M. Johnsen, P. K. Frederiksen, S. E. Braslavsky and P. R. Ogilby, *J Phys Chem A*, 2006, **110**, 7375-7385.

176. L. K. McKenzie, H. E. Bryant and J. A. Weinstein, *Coord. Chem. Rev.*, 2019, **379**, 2-29.

177. R. Zhang, Y. Duan and B. Liu, *Nanoscale*, 2019, **11**, 19241-19250.

178. C.-H. Lee and J. S. Lindsey, *Tetrahedron*, 1994, **50**, 11427-11440.

179. A. Jiblaoui, Limoges, 2013.

180. J. Jökel, F. Schwer, M. von Delius and U.-P. Apfel, *Chemical Communications*, 2020, **56**, 14179-14182.

181. B. J. Littler, Y. Ciringh and J. S. Lindsey, *J. Org. Chem.*, 1999, **64**, 2864-2872.

182. J. S. Lindsey, *Accounts of chemical research*, 2010, **43**, 300-311.

183. Q. M. Wang and D. W. Bruce, *Synlett*, 1995, **1995**, 1267-1268.

184. A. Jiblaoui, C. Baudequin, V. Chaleix, G. Ducourthial, F. Louradour, Y. Ramondenc, V. Sol and S. Leroy-Lhez, *Tetrahedron*, 2013, **69**, 5098-5103.

185. R. W. Boyle, C. K. Johnson and D. Dolphin, *Journal of the Chemical Society, Chemical Communications*, 1995, 527-528.

186. D. A. Shultz, K. P. Gwaltney and H. Lee, *The Journal of Organic Chemistry*, 1998, **63**, 769-774.

187. T. Dohi, M. Ito, N. Yamaoka, K. Morimoto, H. Fujioka and Y. Kita, *Tetrahedron*, 2009, **65**, 10797-10815.

188. Z. M. Hudson, Z. Wang, M. G. Helander, Z. H. Lu and S. Wang, *Advanced Materials*, 2012, **24**, 2922-2928.

189. D. B. G. Williams and M. Lawton, *The Journal of organic chemistry*, 2010, **75**, 8351-8354.

190. D. R. Burfield, K.-H. Lee and R. H. Smithers, *The Journal of Organic Chemistry*, 1977, **42**, 3060-3065.

191. T. D. Lash, *Chemical reviews*, 2017, **117**, 2313-2446.

192. B. Szyszko and L. Latos-Grażyński, *Chem. Soc. Rev.*, 2015, **44**, 3588-3616.

193. B. Szyszko and L. Latos-Grażyński, *Angew. Chem. Int. Ed.*, 2020, **59**, 16874-16901.

194. T. D. Lash and S. T. Chaney, *Angewandte Chemie International Edition in English*, 1997, **36**, 839-840.

195. K. M. Bergman, G. M. Ferrence and T. D. Lash, *The Journal of Organic Chemistry*, 2004, **69**, 7888-7897.

196. K. Laxman, A. Kumar and M. Ravikanth, *Asian J. Org. Chem.*, 2020, **9**, 162-180.

197. J.-H. Hong, A. S. Aslam, M. Ishida, S. Mori, H. Furuta and D.-G. Cho, *J. Am. Chem. Soc.*, 2016, **138**, 4992-4995.

198. A. Sinha and M. Ravikanth, *J. Org. Chem.*, 2021, **86**, 6100-6110.

199. B. Szyszko, L. Latos-Grażyński and L. Szterenberg, *Chem. Commun.*, 2012, **48**, 5004-5006.

200. B. Szyszko, P. Rymut, M. Matviyishyn, A. Białońska and L. Latos-Grażyński, *Angew. Chem. Int. Ed.*, 2020, **59**, 20137-20146.

201. M.-C. Yoon, S. Cho, M. Suzuki, A. Osuka and D. Kim, *J. Am. Chem. Soc.*, 2009, **131**, 7360-7367.

202. T. Tanaka and A. Osuka, *Chemical reviews*, 2017, **117**, 2584-2640.

203. B. Szyszko, A. Białońska, L. Szterenberg and L. Latos-Grażyński, *Angew. Chem.*, 2015, **127**, 5014-5018.

204. T. D. Lash, D. A. Colby and L. F. Szczepura, *Inorganic chemistry*, 2004, **43**, 5258-5267.

205. K. Kupietz, M. J. Białek, K. Hassa, A. Białońska and L. Latos-Grażyński, *Inorganic chemistry*, 2019, **58**, 12446-12456.

206. M. Bröring, H. J. Dietrich, J. Dörr, G. Hohlneicher, J. Lex, N. Jux, C. Pütz, M. Roeb, H. Schmickler and E. Vogel, *Angew. Chem. Int. Ed.*, 2000, **39**, 1105-1108.

207. T. D. Lash, S. T. Chaney and D. T. Richter, *J. Org. Chem.*, 1998, **63**, 9076-9088.

208. B. Szyszko and L. Latos-Grażyński, *Organometallics.*, 2011, **30**, 4354-4363.

209. B. Szyszko, E. Pacholska-Dudziak and L. Latos-Grażyński, *J. Org. Chem.*, 2013, **78**, 5090-5095.

210. T. D. Lash, *Chemistry–An Asian Journal*, 2014, **9**, 682-705.

211. R. Misra and T. K. Chandrashekar, *Acc. Chem. Res.*, 2008, **41**, 265-279.

212. N. Shivran, S. C. Gadekar and V. G. Anand, *Chemistry–An Asian Journal*, 2017, **12**, 6-20.

213. T. Koide, K. Youfu, S. Saito and A. Osuka, *Chem. Commun.*, 2009, 6047-6049.

214. B. Szyszko, M. Małecki, A. Berlicka, M. J. Białek, A. Białońska, K. Kupietz, E. Pacholska-Dudziak and L. Latos-Grażyński, *Chem. Eur. J.*, 2016, **22**, 7602-7608.

215. S. Pushpan, M. Kumar and T. Chandrashekar, *Journal of the Chemical Society, Perkin Transactions 2*, 1999, 961-968.

216. R. L. Hill, M. Gouterman and A. Ulman, *Inorganic Chemistry*, 1982, **21**, 1450-1455.

217. B. Szyszko, M. Matviyishyn, S. Hirka, E. Pacholska-Dudziak, A. Białońska and L. Latos-Grażyński, *Org. Lett.*, 2019, **21**, 7009-7014.

218. K. Kurotobi, K. S. Kim, S. B. Noh, D. Kim and A. Osuka, *Angew. Chem. Int. Ed.*, 2006, **45**, 3944-3947.

219. Y. Inokuma, N. Ono, H. Uno, D. Y. Kim, S. B. Noh, D. Kim and A. Osuka, *Chem. Commun.*, 2005, 3782-3784.

220. Y. Nakamura, S. Y. Jang, T. Tanaka, N. Aratani, J. M. Lim, K. S. Kim, D. Kim and A. Osuka, *Chem. Eur. J.*, 2008, **14**, 8279-8289.

221. T. K. Ahn, K. S. Kim, D. Y. Kim, S. B. Noh, N. Aratani, C. Ikeda, A. Osuka and D. Kim, *J. Am. Chem. Soc.*, 2006, **128**, 1700-1704.

222. H. Rath, J. Sankar, V. PrabhuRaja, T. K. Chandrashekar, A. Nag and D. Goswami, *J. Am. Chem. Soc.*, 2005, **127**, 11608-11609.

223. R. Misra, R. Kumar, T. K. Chandrashekar, A. Nag and D. Goswami, *Org. Lett.*, 2006, **8**, 629-631.

224. I. Hisaki, S. Hiroto, K. S. Kim, S. B. Noh, D. Kim, H. Shinokubo and A. Osuka, *Angew. Chem.*, 2007, **119**, 5217-5220.

225. J.-Y. Shin, K. S. Kim, M.-C. Yoon, J. M. Lim, Z. S. Yoon, A. Osuka and D. Kim, *Chem. Soc. Rev.*, 2010, **39**, 2751-2767.

226. S. Gokulnath and T. K. Chandrashekar, *Journal of Chemical Sciences*, 2008, **120**, 137-142.

227. T. K. Ahn, J. H. Kwon, D. Y. Kim, D. W. Cho, D. H. Jeong, S. K. Kim, M. Suzuki, S. Shimizu, A. Osuka and D. Kim, *J. Am. Chem. Soc.*, 2005, **127**, 12856-12861.

228. J.-Y. Shin, J. M. Lim, Z. S. Yoon, K. S. Kim, M.-C. Yoon, S. Hiroto, H. Shinokubo, S. Shimizu, A. Osuka and D. Kim, *J. Phys. Chem. B.*, 2009, **113**, 5794-5802.

229. B. Habermeyer and R. Guilard, *Photochem. Photobiol. Sci.*, 2018, **17**, 1675-1690.

230. R. Paolesse, S. Nardis, D. Monti, M. Stefanelli and C. Di Natale, *Chemical reviews*, 2017, **117**, 2517-2583.

231. N. Mihara, Y. Yamada, H. Takaya, Y. Kitagawa, K. Igawa, K. Tomooka, H. Fujii and K. Tanaka, *Chem. Eur. J.*, 2019, **25**, 3369-3375.

232. A. Srinivasan, M. R. Kumar, R. Pandian, S. Mahajan, K. S. Pushpan, B. Sridevi, S. J. Narayanan and T. Chandrashekar, *J. Porphyrins Phthalocyanines*, 1998, **2**, 305-314.

233. E. Robbins, R. Deska, K. Ślusarek, M. Dudek, M. Samoć, L. Latos-Grażyński, B. Szyszko and K. Matczyszyn, *RSC advances*, 2022, **12**, 19554-19560.

234. X.-J. Liu, J.-K. Feng, A.-M. Ren and X. Zhou, *Chem. Phys. Lett.*, 2003, **373**, 197-206.

235. L. Latos-Grażyński, E. Pacholska, P. J. Chmielewski, M. M. Olmstead and A. L. Balch, *Inorganic Chemistry*, 1996, **35**, 566-573.

236. K. T. Mahmudov, M. N. Kopylovich, M. F. C. G. da Silva and A. J. Pombeiro, *Dalton Trans.*, 2017, **46**, 10121-10138.

237. A. Kumar, K. Laxman and M. Ravikanth, *Org. Lett.*, 2019, **21**, 8726-8730.

238. S. Wang, J. Shang, C. Yan, W. Wang, C. Yuan, H.-L. Zhang and X. Shao, *Org. Chem. Front*, 2019, **6**, 263-272.

239. J. Pirillo, B. C. De Simone and N. Russo, *Theor. Chem. Acc.*, 2016, **135**, 1-5.

240. J. C. Koziar and D. O. Cowan, *Acc. Chem. Res.*, 1978, **11**, 334-341.

241. K. M. Farrell, M. M. Brister, M. Pittelkow, T. I. Sølling and C. E. Crespo-Hernández, *J. Am. Chem. Soc.*, 2018, **140**, 11214-11218.

242. B. Küçüköz, G. Sevinç, E. Yildiz, A. Karatay, F. Zhong, H. Yılmaz, Y. Tutel, M. Hayvalı, J. Zhao and H. Yaglioglu, *Phys. Chem. Chem. Phys.*, 2016, **18**, 13546-13553.

243. S. Tekin, B. Küçüköz, H. Yılmaz, G. Sevinç, M. Hayvalı, H. G. Yaglioglu and A. Elmali, *J. Photochem. Photobiol. A.*, 2013, **256**, 23-28.

244. E. W. Van Stryland and M. Sheik-Bahae, in *Characterization Techniques and Tabulations for Organic Nonlinear Materials*, Marcel Dekker, Inc, 1st edn., 1998, pp. 671-708.

245. M. Pawlicki, H. A. Collins, R. G. Denning and H. L. Anderson, *Angew Chem Int Ed Engl*, 2009, **48**, 3244-3266.

246. S. J. Zelewski, K. C. Nawrot, A. Zak, M. Gladysiewicz, M. Nyk and R. Kudrawiec, *J. Phys. Chem. Lett.*, 2019, **10**, 3459-3464.

247. F. A. Devillanova and W.-W. Du Mont, *Handbook of chalcogen chemistry: new perspectives in sulfur, selenium and tellurium*, Royal Society of Chemistry, 2013.

248. W. Levason, S. D. Orchard and G. Reid, *Organometallics.*, 1999, **18**, 1275-1280.

249. A. J. Barton, W. Levason and G. Reid, *J. Organomet. Chem.*, 1999, **579**, 235-242.

250. A. J. Genge, S. Orchard and S. A. Pope, *J. Chem. Soc., Dalton Trans.*, 1999, DOI: 10.1039/A902820J, 2343-2352.

251. J. Zhao, W. Wu, J. Sun and S. Guo, *Chem. Soc. Rev.*, 2013, **42**, 5323-5351.

252. A. Rodriguez-Serrano, V. Rai-Constapel, M. C. Daza, M. Doerr and C. M. Marian, *Phys. Chem. Chem. Phys.*, 2015, **17**, 11350-11358.

253. A. Karatay, M. C. Miser, X. Cui, B. Küçüköz, H. Yılmaz, G. Sevinç, E. Akhüseyin, X. Wu, M. Hayvali and H. G. Yaglioglu, *Dyes Pigm.*, 2015, **122**, 286-294.

254. B. Sauerwein and G. B. Schuster, *The Journal of Physical Chemistry*, 1991, **95**, 1903-1906.

255. D. G. Hilmey, M. Abe, M. I. Nelen, C. E. Stilts, G. A. Baker, S. N. Baker, F. V. Bright, S. R. Davies, S. O. Gollnick and A. R. Oseroff, *J. Med. Chem.*, 2002, **45**, 449-461.

256. C.-L. Sun, Q. Liao, T. Li, J. Li, J.-Q. Jiang, Z.-Z. Xu, X.-D. Wang, R. Shen, D.-C. Bai and Q. Wang, *Chem. Sci.*, 2015, **6**, 761-769.

257. J. Bhawalkar, N. Kumar, C.-F. Zhao and P. Prasad, *J Laser Med Sci.*, 1997, **15**, 201-204.

258. S. Kim, T. Y. Ohulchanskyy, H. E. Pudavar, R. K. Pandey and P. N. Prasad, *J. Am. Chem. Soc.*, 2007, **129**, 2669-2675.

259. Q. Zheng, A. Bonoiu, T. Y. Ohulchanskyy, G. S. He and P. N. Prasad, *Mol. Pharm.*, 2008, **5**, 389-398.

260. Z. F. Chang, L. M. Jing, B. Chen, M. Zhang, X. Cai, J. J. Liu, Y. C. Ye, X. Lou, Z. Zhao, B. Liu, J. L. Wang and B. Z. Tang, *Chem. Sci.*, 2016, **7**, 4527-4536.

261. Q. Zhang, X. Tian, H. Zhou, J. Wu and Y. Tian, *Materials.*, 2017, **10**.

262. J.-C. Liu, X.-Z. Li and Y. Zhang, Beijing, China, 2016.

263. M. G. Silly, L. Porrès, O. Mongin, P.-A. Chollet and M. Blanchard-Desce, *Chem. Phys. Lett.*, 2003, **379**, 74-80.

264. Q. Zheng, S. K. Gupta, G. S. He, L. S. Tan and P. N. Prasad, *Adv. Funct. Mater.*, 2008, **18**, 2770-2779.
265. Q. Zhang, S. Yue, H. Sun, X. Wang, X. Hao and S. An, *J. Mater. Chem. C.*, 2017, **5**, 3838-3847.
266. Z. Pokladek, N. Ripoche, M. Betou, Y. Trolez, O. Mongin, J. Olesiak-Banska, K. Matczyszyn, M. Samoc, M. G. Humphrey and M. Blanchard-Desce, *Chem. Eur. J.*, 2016, **22**, 10155-10167.
267. K. Matczyszyn, J. Olesiak-Banska, K. Nakatani, P. Yu, N. A. Murugan, R. Zalesny, A. Roztoczynska, J. Bednarska, W. Bartkowiak and J. Kongsted, *J. Phys. Chem. B.*, 2015, **119**, 1515-1522.
268. L. Chen, R. Hu, J. Xu, S. Wang, X. Li, S. Li and G. Yang, *Spectrochim. Acta A Mol. Biomol. Spectrosc.*, 2013, **105**, 577-581.
269. K. Kamada, T. Sugino, M. Ueda, K. Tawa, Y. Shimizu and K. Ohta, *Chem. Phys. Lett.*, 1999, **302**, 615-620.
270. K. Kamada, M. Ueda, T. Sakaguchi, K. Ohta and T. Fukumi, *JOSA B*, 1998, **15**, 838-845.
271. L. Ma, J. Moan and K. Berg, *Int. J. Cancer*, 1994, **57**, 883-888.

# PUBLICATIONS

1. **Emma L. Robbins**, Radosław A. Deska, Katarzyna Ślusarek, Marta M. Dudek, Marek Samoć, Lechosław Latos-Grażyński, Bartosz Szyszko, Katarzyna Matczyszyn: **Two-photon absorption of 28-hetero-2,7-naphthiporphyrins: expanded carbaporphyrinoid macrocycles**

RSC Advances. 2022, vol. 12, nr 30, 19554-19560.

DOI: 10.1039/D2RA03167A

2. **Emma L. Robbins**, S. G. Mucha, Dominika Benkowska-Biernacka, Krzysztof Nadolski, Nidia Maldonado-Carmona, Nicolas Villandier, Stéphanie Leroy-Lhez, Katarzyna Matczyszyn: **Porphyrin-loaded acetylated lignin nanoparticles as a remarkable biomarker emitting in the first optical window**

Journal of Porphyrins and Phthalocyanines. 2022, 1-8.

DOI: 10.1142/S1088424622500377

3. Piotr Gierlich, S. G. Mucha, **Emma L. Robbins**, Lígia C. Gomes-da-Silva, Katarzyna Matczyszyn, Mathias O. Senge: **One-photon and two-photon photophysical properties of tetrafunctionalized Temoporfin (*m*-THPC) derivatives as potential agents for two-photon induced photodynamic therapy**

ChemPhotoChem. 2021, 7, 1-12.

DOI: 10.1002/cptc.202100249

4. **Emma L. Robbins**, Stéphanie Leroy-Lhez, Nicolas Villandier, Marek Samoć, Katarzyna Matczyszyn: **Prospects for more efficient multi-photon absorption photosensitizers exhibiting both reactive oxygen species generation and luminescence**

Molecules. 2021, vol.26, nr 20, art. 6323, 1-39.

**Special Issue:** Photodynamic Therapy in Cancer Treatment 2021.

DOI: 10.3390/molecules26206323